A THREE-PLATE KINEMATIC MODEL FOR LAU BASIN OPENING

A THESIS SUBMITTED TO THE GRADUATE DIVISION OF THE UNIVERSITY OF HAWAI'I IN PARTIAL FULFILLMENT OF THE REQUIREMENTS FOR THE DEGREE OF

MASTER OF SCIENCE

IN

GEOLOGY AND GEOPHYSICS

AUGUST 2000

By
Kirsten E. Zellmer

Thesis Committee:

Brian Taylor, Chairperson
Steven J. Martel
Fernando Martinez

We certify that we have read this thesis and that, in our opinion, it is satisfactory in scope and quality as a thesis for the degree of Master of Science in Geology and Geophysics.

THESIS COMMITTEE

_____

Chairperson

_____

_____

ACKNOWLEDGMENTS

I would like to especially thank Brian Taylor for always taking the time to discuss the scientific implications of my research with me. The countless conversations we had, particularly during the period in which the three-plate statistical pole code was being developed, most certainly shaped the ultimate direction of this project. I would also like to thank my entire committee for discussing with me many of the other research focuses possible for the Lau Basin. Also, I extend many thanks to all of my housemates and friends here at UH for keeping me positive during the development of this project and the completion of this work.

ABSTRACT

Recognizing the Niuafo'ou Microplate (N) between the Australian (A) and Tongan (T) Plates north of 19 20'S, we solve the kinematics of Lau Basin opening consistent with marine and geodetic data. We present a new three-plate model derived from statistically best-fitting a set of data that includes (1) Bruhnes spreading rates, (2) azimuths of spreading axes and Peggy Ridge (PR) transform fault, (3) focal mechanisms, and (4) geodetically determined A-T velocities. First, we independently determine the three Euler poles using data from the following plate boundaries: A-T = East Lau Spreading Center (ELSC); A-N = Central Lau Spreading Center (CLSC) and PR; N-T = Fonualei Rift and Spreading Center (FRSC). Second, we search their associated 95% confidence ellipses to determine a set of compatible poles that meet three-plate circuit criteria. This three-plate model resolves the former apparent conflict between magnetic anomaly spreading rates and geodetic rates (Taylor et al., EPSL 1996).

TABLE OF CONTENTS

LIST OF TABLES

LIST OF FIGURES

CHAPTER 1. INTRODUCTION

1.1 Geology of the Lau Backarc Basin

The Lau Basin is one of the best-studied backarc basins of the western Pacific (Fig. 1.1). Classically, a backarc basin is defined to be a region of newly accreted seafloor that is positioned between an inactive remnant arc and an active volcanic arc (Weissel, 1981). The Lau Basin is situated above the westward-dipping lithospheric slab that is subducting at the Tonga Trench. It is bounded by the inactive Lau Ridge in the west and the active Tofua volcanic arc in the east (Fig. 1.2).

The Lau Basin contains several prominent tectonically active structures (Fig. 1.2). Peggy Ridge (PR) is an active right-lateral transform fault (Weissel, 1977). Its northwest terminus is located at the Fatuna Spreading Center (FSC) (Pelletier et al., unpubl.). To the southeast the PR links to the Central Lau Spreading Center (CLSC) via a complex series of left-stepping, *en échelon* spreading segments that comprise the Lau Extensional Transform Zone (LETZ) (Taylor et al., 1994, 1996). The CLSC is currently propagating to the south, and its southern tip overlaps the northern segments of the East Lau Spreading Center (ELSC) (Parson et al., 1990). The ELSC likewise consists of left-stepping segments, the southernmost being known as the Valu Fa (VF) ridge (Morton and Sleep, 1985). The area immediately south of the ELSC is a region of active rifting. In the northern region of Lau Basin, two spreading centers have been identified: the Northwest Lau Spreading Center (NWLSC) (Tiffin, 1993) and the Fonualei Rift and Spreading Center (FRSC). The NWLSC strikes nearly orthogonal to the PR and consists of right-stepping segments, some of which have not been well mapped. The FRSC comprises

Fig. 1.1. Bathymetry of the western Pacific (Smith and Sandwell, 1997). White box indicates the location of the Lau Basin and Fig. 1.2. Depth scale is in km.

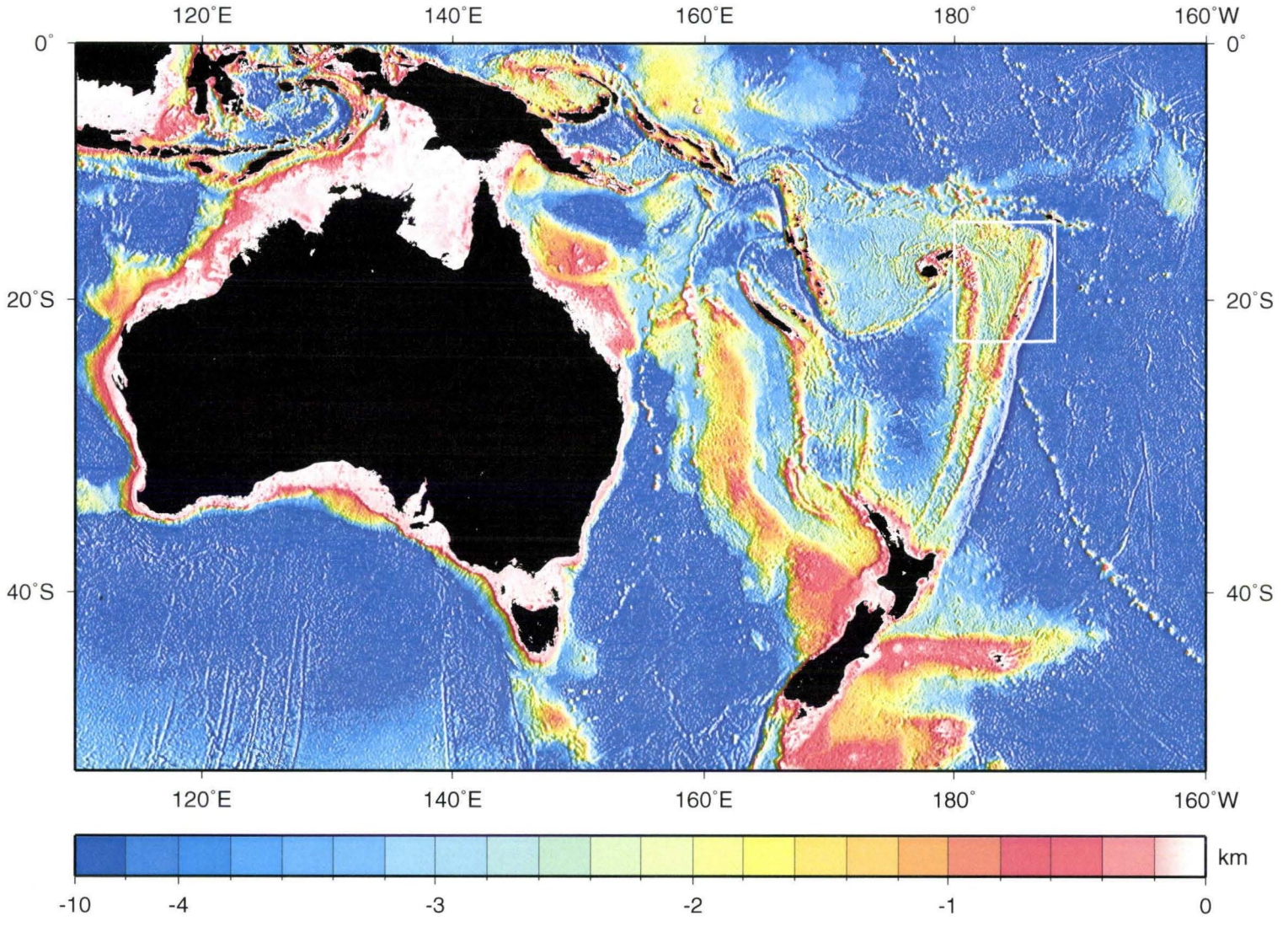
120°E
140°E
160°E
180°
160°W
0°
20°S
40°S
km
-10
-4
-3
-2
-1
0

Fig. 1.2. Lau Basin bathymetric map showing the location of currently recognized plate boundaries (black lines). Thick lines indicate plate boundaries that are accommodating active spreading; thin lines indicate transform faults. Depth scale is in km. Plate boundaries are labeled as follows: CLSC=Central Lau Spreading Center; ELSC=East Lau Spreading Center; FRSC=Fonualei Rift and Spreading Center; FSC=Fatuna Spreading Center; LETZ=Lau Extensional Transform Zone; PR=Peggy Ridge; MTJ=Mangatolu Triple Junction; NWLSC=Northwest Lau Spreading Center.

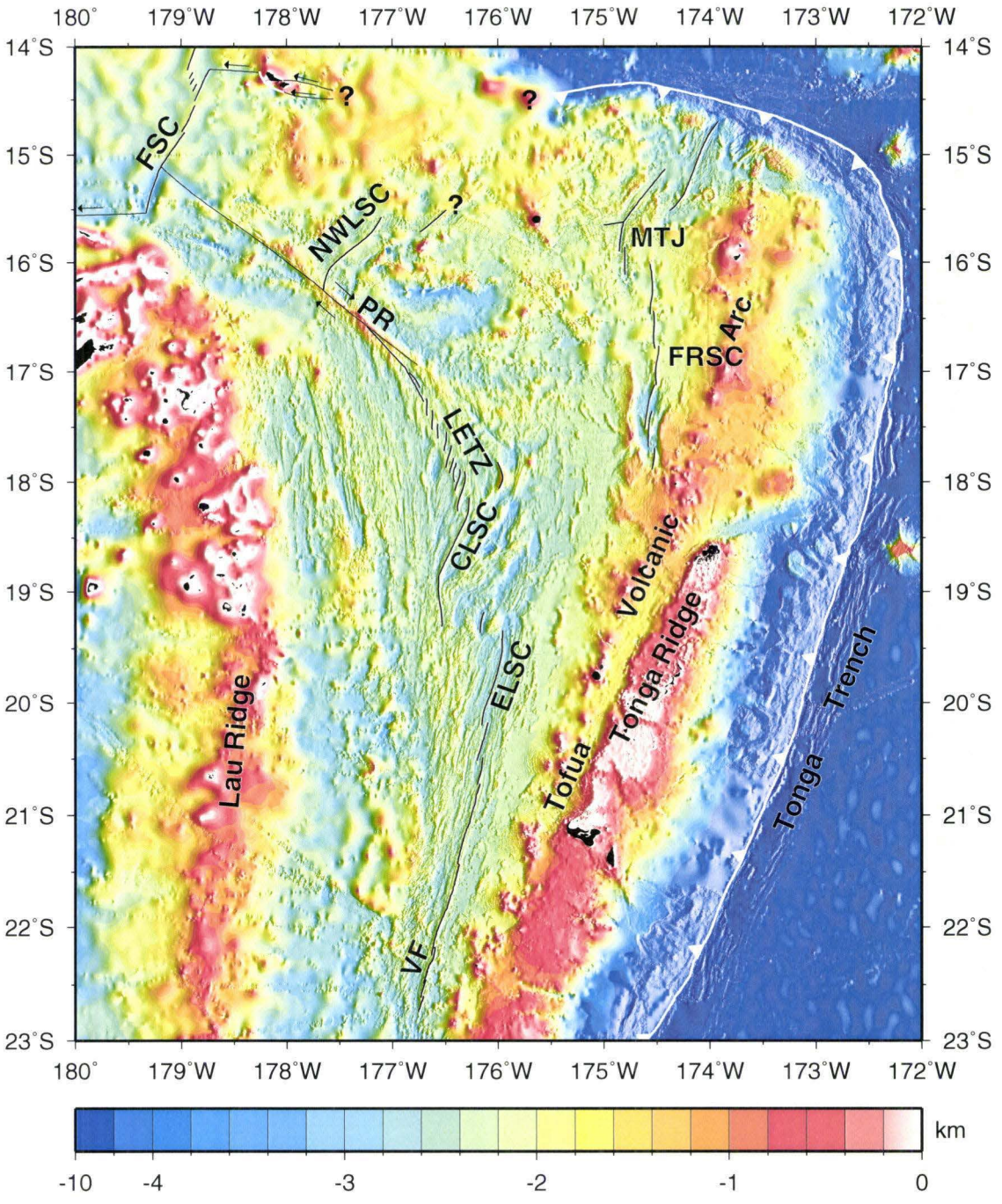
180°
179°W
178°W
177°W
176°W
175°W
174°W
173°W
172°W
14°S
15°S
16°S
17°S
18°S
19°S
20°S
21°S
22°S
23°S
FSC
NWLSC
PR
LETZ
CLSC
ELSC
VF
MTJ
FRSC
Arc
Volcanic
Tonga Ridge
Tofua
Tonga Trench
Lau Ridge
?
km
-10
-4
-3
-2
-1
0

the spreading centers extending south of the Mangatolu Triple Junction (MTJ, also known as the Kings Triple Junction) (Hawkins and Helu, 1986).

1.2 Background

Karig (1970) recognized that the Lau Basin was in an extensional regime despite its seemingly paradoxical location near a convergent margin. Lawver et al. (1976) attempted to differentiate between "types" of backarc basins: (1) those that originated as "normal" oceanic crust (Fig. 1.3 (a)) and (2) those that originated and evolved by entirely different tectonic extensional processes that were inherently linked to their position above a subducting lithospheric slab (Fig. 1.3 (b)). Lawver et al. cited the Lau Basin as one of the latter type, and in doing so started a debate about Lau Basin extension that lasted twenty years. They proposed that the Lau Basin could be extending via processes analogous to spreading ocean ridges, but had difficulty in identifying magnetic lineations in part due to lack of dense data coverage at the time. They suggested that the magnetic anomalies they could identify (south of 19° S) were created at either a series of short *en échelon* ridges or by intrusion of dikes at ridge crests. They thought that this type of extension would force the basin to evolve in such a way that it would be "difficult to distinguish between rigid plate tectonics and numerous random spreading centers." Weissel (1977), on the other hand, proposed that a rigid multiple plate system was possible given the non-orthogonal configuration of the northwest trending PR and the north-south oriented spreading segments south of the transform (Fig. 1.4). Although Weissel was more confident in identifying these magnetic lineations, he agreed that the anomalies probably formed along short ridge segments. Therefore, his view was that a tectonic

Fig. 1.3. Diagrams reproduced from Lawver and Hawkins (1978) that serve to illustrate the debate surrounding the nature of the extension in the Lau Basin. (a) Backarc basin extension occurring via "normal" organized seafloor spreading processes similar to that on the mid-ocean ridge system. (b) Backarc basin extension occurring via a disorganized extensional process that results in a series of short, disconnected ridges and numerous seamounts distributed throughout the basin.

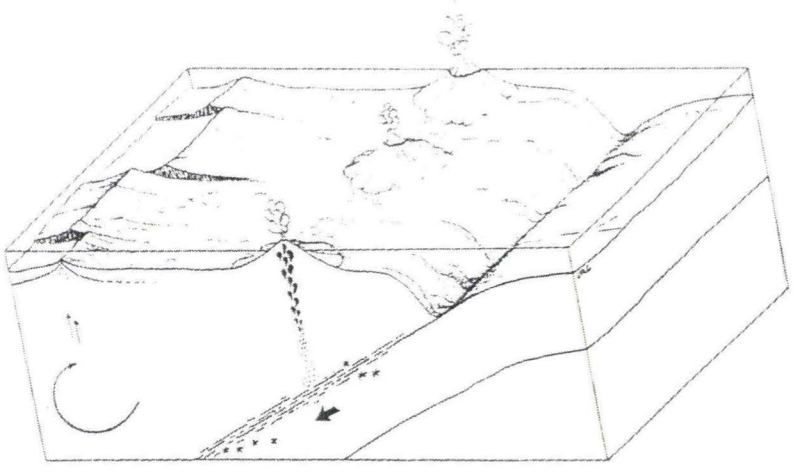

(a)

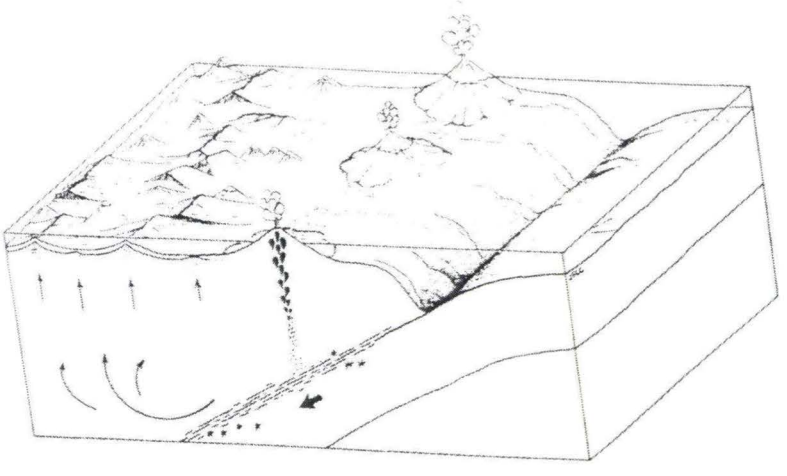

(b)

Fig. 1.4. Tectonic interpretation of a multiple plate system for the Lau Basin (reproduced from Weissel, 1977). Heavy lines denote active plate boundaries. Given the non-orthogonal configuration of PR (for the location of PR, refer to Fig. 1.2) and the north-south trending magnetic lineations (thin lines), Weissel (1977) proposed a set of hypothetical plate boundaries (broken heavy dashed lines) in the region north of 18°S. Magnetic anomalies are labeled as follows: J=Jaramillo; 2=Olduvai; 2'=Gauss.


179°
15°
173°
15°
2000
2'
2
J
V
21°
179°
21°
173°

plate system was possible, but that the evolution of the basin proceeded via a complex set of interactions between small plates.

Lawver and Hawkins (1978) supported the concept of "diffuse" spreading across the basin as opposed to "normal" seafloor spreading for Lau Basin evolution. They interpreted the complex pattern of magnetic anomalies to be due in part to the "abundant short ridges" and "point-source magma leaks" (seamounts) in the area. Weissel (1981) countered with a paper that examined magnetic lineations in several backarc basins in the western Pacific, and emphasized the existence of identifiable short north-south lineations as evidence for crustal accretion in distinct narrow zones while holding to the theory that the basin evolved by the growth of more than two plates. At the time, Taylor and Karner (1983) subsequently questioned possible correlations between "global" versus "local" driving forces for the formation of backarc basins. They suggested that spreading in the Lau Basin requires more than just a passive response to the global plate kinematics. Hamburger and Isacks (1988), however, continued to support the idea of "diffuse deformation" in back-arc basins by interpreting shallow seismicity and active zones of volcanism to be related to sets of pull-apart basins rather than to any single defined zone of activity (Fig. 1.5). Thus, by the late 1980s, support for the concept of "diffuse" tectonics in the Lau Basin remained strong.

Numerous Lau Basin marine geophysical surveys occurred throughout the 1980s and 1990s, including an Ocean Drilling Program (ODP) cruise in 1992. Parson and Hawkins (1994) recompiled both the bathymetric and the magnetic data. The recompiled magnetic anomaly map from this study is reproduced in Fig. 1.6 (a). Parson and Hawkins stated that "no continuous

Fig. 1.5. Hamburger and Isacks (1988) model of deformation interpreted from Lau Basin seismic slip vectors. This model supported the concept that disorganized, distributed diffuse deformation was occurring throughout the entire backarc basin.

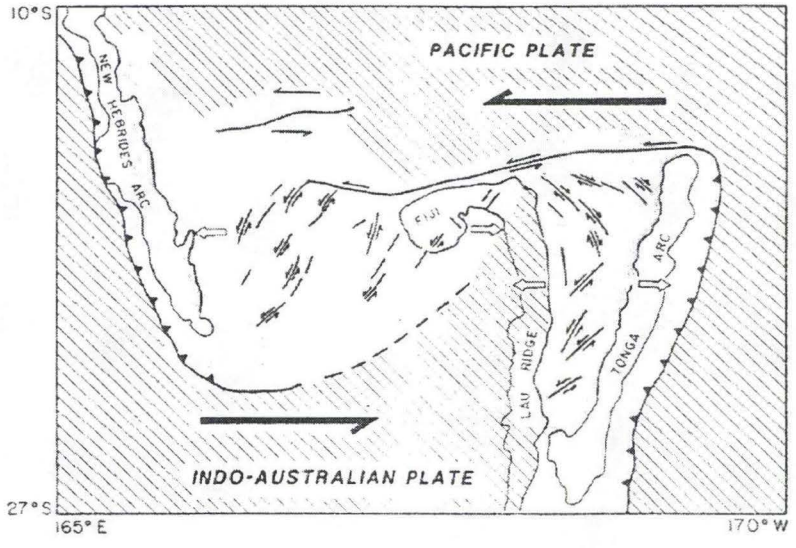
10°S
27°S
165° E
170° W
PACIFIC PLATE
INDO-AUSTRALIAN PLATE
NEW HEBRIDES ARC
FIJI
LAU RIDGE
TONGA
ARC

Fig. 1.6. (a) Contoured residual magnetic anomaly map reproduced from Parson and Hawkins (1994). Positively magnetized anomalies are plotted in white. (b) Interpretation of magnetic anomalies plotted in (a) from Parson and Hawkins (1994). Parson and Hawkins (1994) note that the anomalies shown in (a) were weak (less than 200 nT) making true magnetic boundaries difficult to identify. Magnetic anomalies are labeled as follows: 1=Brunhes; J=Jaramillo; 2=Olduvai; 2R=Matuyama; 2A=Gauss.

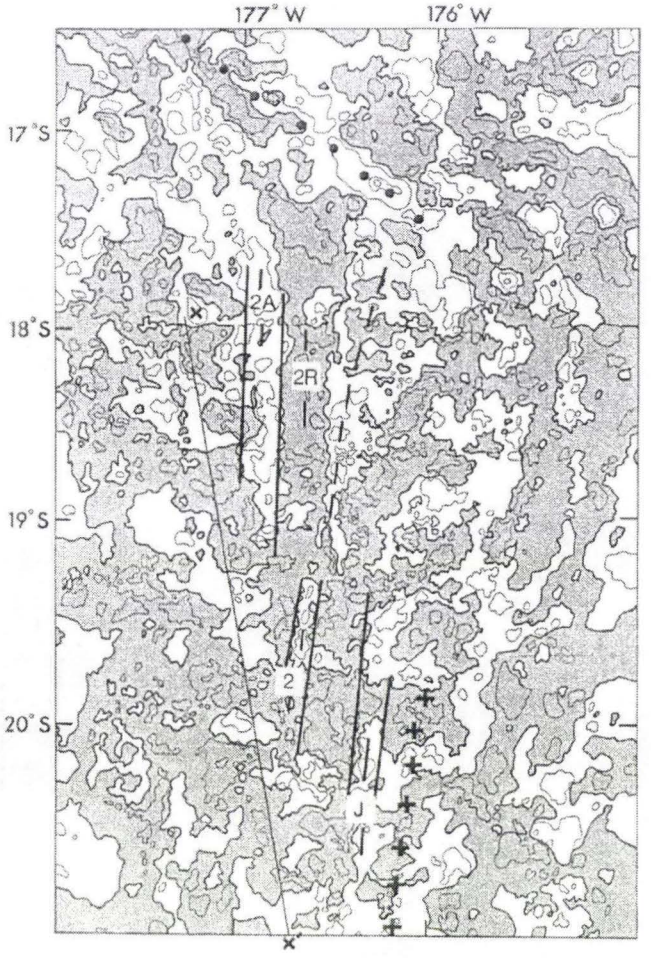
177° W
176° W
17°S
18°S
19°S
20°S
2A
2R
2
J

(a)

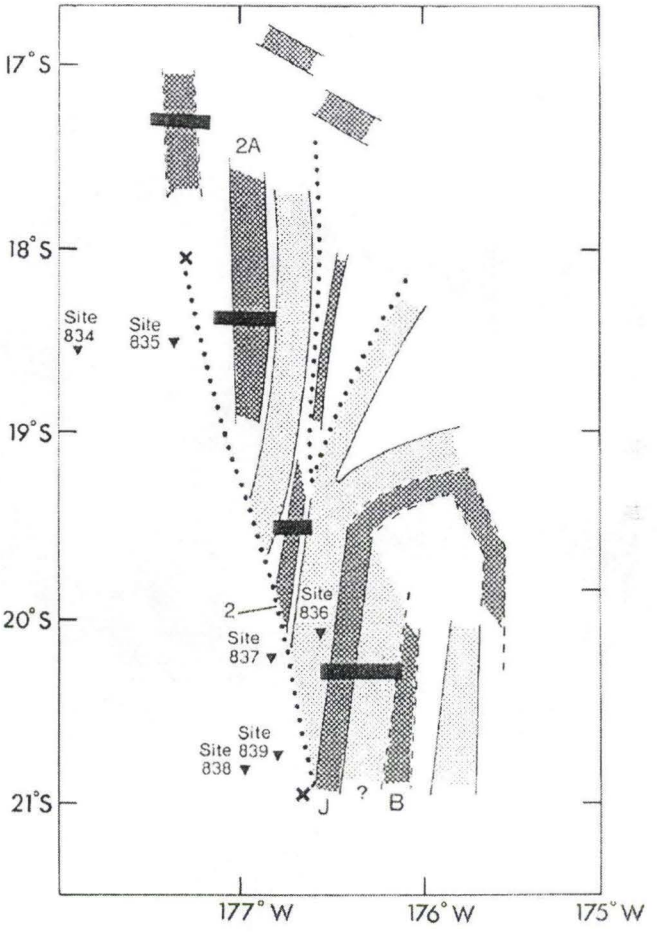
17°S
18°S
19°S
20°S
21°S
2A
Site 834
Site 835
2
Site 836
Site 837
Site 838
Site 839
J
?
B
177° W
176° W
175° W

(b)

magnetic lineations could be unequivocally mapped, and only weak (< 200 nT) anomalies appear as discrete, isolated areas", thus supporting the idea that backarc basin opening was somehow fundamentally different from "normal" seafloor spreading. Despite this problem with the data, they interpreted the magnetic anomaly pattern (Fig. 1.6 (b)) and use crustal age data from the 1992 ODP survey to propose a two-stage ridge propagation model for Lau Basin opening in which arc rifting is replaced by sea-floor spreading (Fig. 1.7).

Taylor et al., (1996) resolved the issues surrounding the problems associated with interpreting "weak" magnetic anomalies by performing a magnetization inversion of the magnetic anomaly and bathymetric data for the basin, and in doing so made magnetic lineations much easier to identify. Fig. 1.8 (a) shows our current version of the Lau Basin magnetic anomalies. It displays weak, isolated anomalies like those identified by Parson and Hawkins (1994). A magnetization inversion corrects for known skewness in the magnetic field and variations in the magnetic source layer (in this study set to be 1 km below seafloor). Our current results of the inversion are shown in Fig. 1.8 (b). Further details regarding the magnetic anomaly compilation and the magnetization inversion are discussed in Chapter 2. The magnetization inversion not only greatly improves the interpretability of the magnetic lineations (Fig. 1.9), but strongly indicates that seafloor spreading in the Lau Basin is indeed similar to "normal" crustal accretion occurring on mid-ocean ridges.

Fig. 1.7. The two-stage propagation model of Parson and Hawkins (1994) in which crust generated by arc rifting (+ pattern) is replaced by crust generated by seafloor spreading at the ELSC and CLSC (stippled pattern). The origin of the crustal domain north of PR (x pattern) remains mostly unknown, and at the time of this paper, the LETZ, FSC, and FRSC had not been mapped.

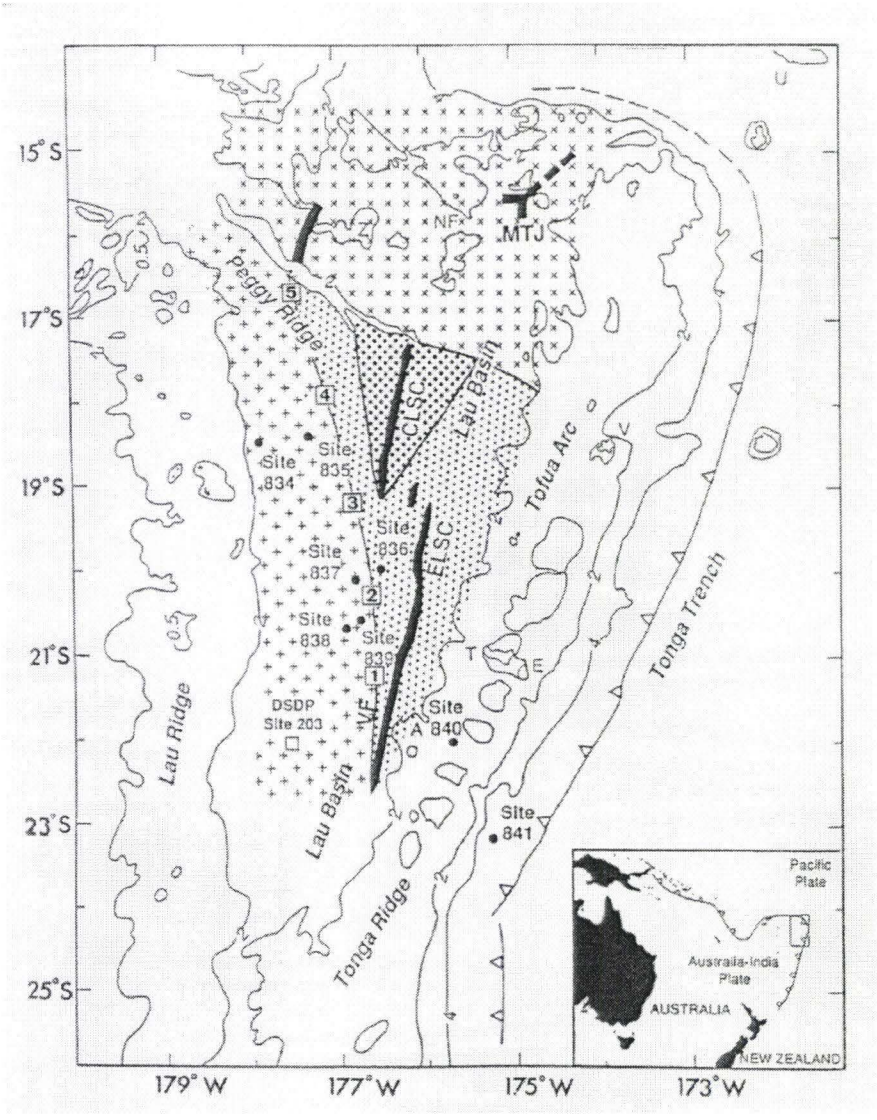
15°S
17°S
19°S
21°S
23°S
25°S
179° W
177° W
175° W
173° W
NF
MTJ
Peggy Ridge
CLSC
ELSC
Lau Basin
Tofua Arc
Tonga Trench
Lau Ridge
Tonga Ridge
VF
Site 834
Site 835
Site 836
Site 837
Site 838
Site 839
Site A 840
Site 841
DSDP Site 203
T
E
1
2
3
4
5
Pacific Plate
Australia-India Plate
AUSTRALIA
NEW ZEALAND

Fig. 1.8. (a) Results of our current magnetic anomaly compilation. Positive magnetic anomalies are plotted in red; negative magnetic anomalies are plotted in blue. Anomalies are additionally highlighted ("sunlit" from the east) to emphasize their location. (b) Magnetization map assuming a 1 km thick source layer beneath the bathymetry. Positively magnetized crust is plotted in red; negatively magnetized crust is plotted in blue. The magnetization map is additionally highlighted with crustal fabric ("sunlit" from the east). The magnetization inversion process greatly improves the recognition of the magnetic lineations.

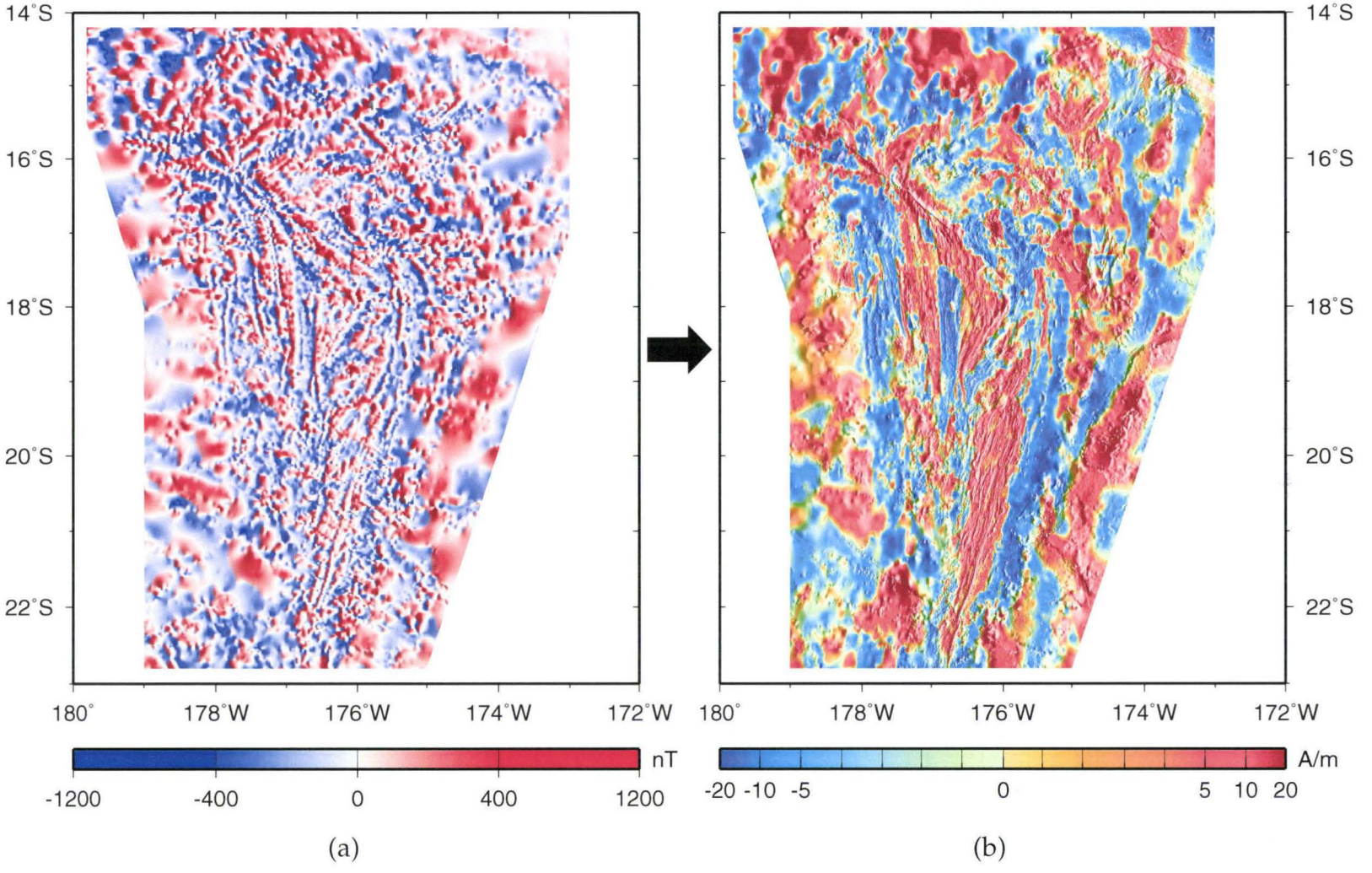
14°S
16°S
18°S
20°S
22°S
180°
178°W
176°W
174°W
172°W
nT
-1200
-400
0
400
1200
(a)
14°S
16°S
18°S
20°S
22°S
180°
178°W
176°W
174°W
172°W
A/m
-20 -10 -5
0
5 10 20
(b)

Fig. 1.9. Interpretation of Lau Basin crustal magnetization distribution. Positively magnetized crust is plotted in red; negatively magnetized crust is plotted in blue. The map is additionally highlighted with crustal fabric ("sunlit" from the east). The results of a similar inversion published in Taylor et al., (1996) proved that seafloor spreading in the Lau Basin is similar to crustal accretion at the mid-ocean ridges. Refer also to Fig. 1.2 for a list of plate boundary names. Magnetic anomalies are labeled as follows: 1=Brunhes; J=Jaramillo; 2=Olduvai; 2A=Gauss.

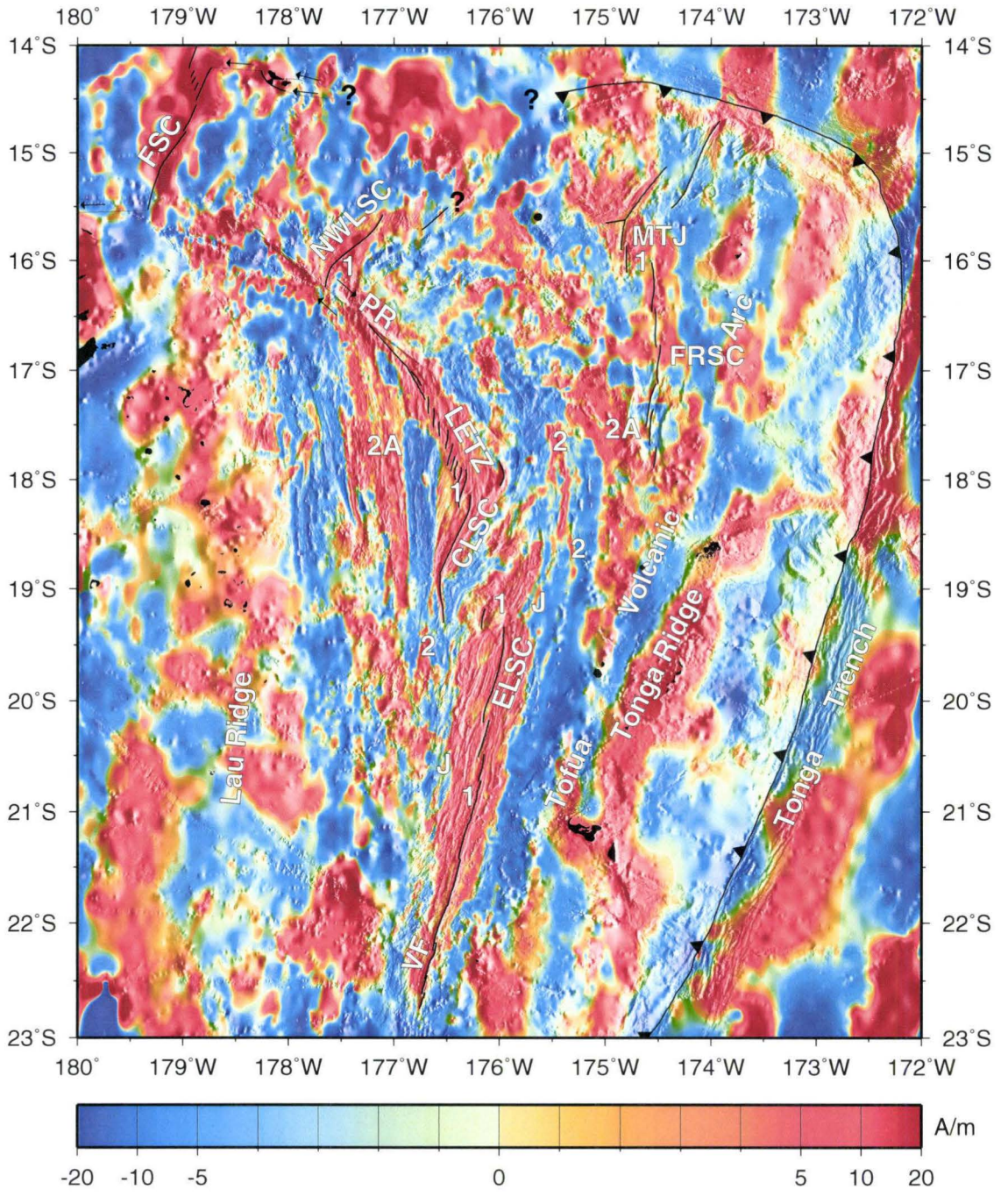
180°
179°W
178°W
177°W
176°W
175°W
174°W
173°W
172°W
14°S
15°S
16°S
17°S
18°S
19°S
20°S
21°S
22°S
23°S
FSC
NWLSC
PR
MTJ
FRSC
Arc
2A
ELSC
CLSC
Volcanic
Tonga Ridge
Trench
Tonga
Tofua
Lau Ridge
VF
A/m
-20
-10
-5
0
5
10
20

1.3 Tectonic History

Once the first magnetization inversion was completed in 1996 and anomalies were confidently identified, a detailed description of the tectonic history south of PR was established by Taylor et al. (1996). They summarized the tectonic evolution of the Lau basin south of PR as follows: (1) At 6 Ma, stretching between the Lau and Tonga Ridges commences, (2) At 4 Ma, the ELSC initiates near the present day location of PR and propagates south, generating north-south seafloor fabric in the process, (3) At 2 Ma, the ELSC boundary rapidly rotated 15° clockwise and broke into left-stepping segments and the CLSC and LETZ initiated. Around this same time, right-lateral active slip began on PR. (4) Between 2 Ma and the present, the ELSC and the CLSC have continued to propagate southward.

1.4 Main Issues

By 1996, the tectonic evolution of the CLSC and the ELSC south of PR was well established under the context of seafloor spreading. However, little was known about the tectonics of the region north of 18°S, and the kinematics of a plate system in the Lau Basin had not been rigorously addressed.

An additional issue with Lau Basin kinematics was also pointed out by Taylor et al. (1996). The Brunhes Chron spreading rates (ranging from ~65 mm/yr in the southern part of the ELSC to ~90 mm/yr near the northern portion of the CLSC) were less that 75% of the opening rates measured geodetically and reported in Bevis (1995). Fig. 1.10 illustrates this discrepancy as it existed in 1996. Taylor et al. (1996) tentatively suggested that spreading rates on the ELSC and the CLSC had rapidly increased in the recent past.

Fig. 1.10. Illustration of the discrepancy between the spreading rates determined from the Brunhes/Matuyama magnetization boundary of Taylor et al. (1996) and the geodetic plate velocities reported in Bevis et al. (1995). Gray areas are regions of positively magnetized crust. According to Taylor et al. (1996), spreading rates range from 65 mm/yr at ~21° S on the ELSC to 90 mm/yr at ~18° S on the CLSC. Respective geodetic relative plate motion vectors (ranging from 91 mm/yr to 130 mm/yr at similar azimuths and latitudes) are much faster than spreading rates predicted by the marine magnetic data.

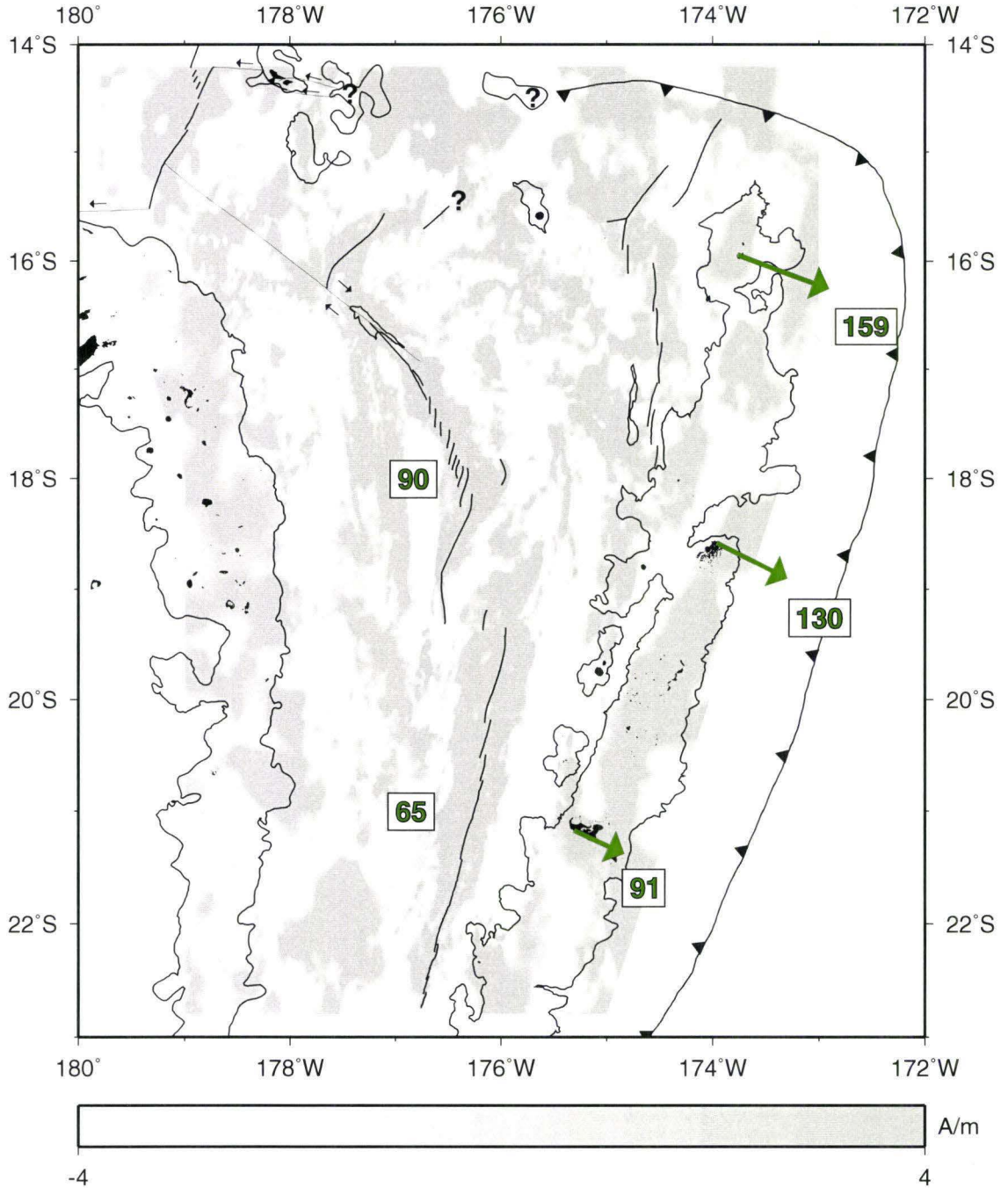
180°
178°W
176°W
174°W
172°W
14°S
16°S
18°S
20°S
22°S
159
90
130
65
91
A/m
-4
4

Revisions to the geodetic data were reported in Bevis (1997) (refer also to chapter 3). The spreading rates determined from the marine magnetic data coincided more closely with the new geodetic plate motion vectors, however, it was unclear whether it was possible to establish kinematics for the Lau Basin consistent with both data sets.

1.5 New Data

Two geophysical cruises have greatly contributed to furthering our knowledge of Lau Basin morphology and structure. In 1995, a detailed survey of the ELSC was conducted (*R/V Hakurei Maru* #2, Cruise HM9507). In 1996, a survey of the southern PR, CLSC, LETZ and a swath to the north was completed (R/V *Moana Wave*, Cruise MW9603). The FRSC was discovered and mapped during the MW9603 cruise, which served to spark ideas about a three-plate system that could account for motion across this boundary. Both magnetic and very high resolution bathymetric data were collected for these two regions, which ultimately served to greatly improve the quality of the Lau Basin magnetization map. Details regarding all the geophysical data compilation methods are included in Chapter 2.

1.6 Questions to be Addressed

In light of the main issues that remained outstanding in 1996 and the new data collected and processed since 1995, the prime question to be addressed here is: Can a multiple plate kinematic model be defined that (1) explains a majority of the tectonic features throughout the basin, (2) is consistent with both spreading rates determined from the marine magnetic data and the revised geodetic velocities, and (3) satisfies rigid plate criteria?

1.7 Proposed Model

In this thesis, the recent tectonics (0.78 Ma - present) of a three-plate system for Lau Basin opening are investigated. In addition to the recompiled bathymetric and magnetic data, a recent compilation of Lau Basin acoustic imagery (Fig. 1.11) greatly aided in the reassessment of all of the identifiable plate boundaries throughout the region, as does Lau Basin seismicity (Fig. 1.12). In the region between the NWLSC/PR/LETZ/CLSC and the MTJ/FRSC lies an aseismic area that is roughly bounded in the north by a tectonically active left-lateral shear zone that is ~100 km wide. To the south of this aseismic region, a few earthquakes are recorded and located, but no distinct narrow plate boundary can be mapped between the CLSC and the FRSC. Despite the ambiguity of the southern boundary of the aseismic region, it is possible to derive a kinematic model that can describe the motion of three plate-like regions within the Lau Basin. We refer to this aseismic region between the NWLSC/PR/LETZ/CLSC and the MTJ/FRSC as the Niuafo'ou (N) microplate (Fig. 1.13) after a small island in the area. We propose that motion between the Australian (A) plate and the Tongan (T) plate is partitioned along the boundaries of the intervening Niuafo'ou microplate.

The tectonics of the following proposed plate boundaries are analyzed: (A-T) ELSC, (A-N) PR, LETZ, CLSC, and (N-T) FRSC. This thesis presents the kinematics of a three-plate system that accounts for geophysical features observed at these boundaries and is consistent with geodetic measurements of relative plate motion. Additionally, the kinematic results of this three-plate model in turn allow for an assessment of the nature of the ambiguous southern boundary of the Niuafo'ou microplate.

Fig. 1.11. Map of Lau Basin acoustic reflectivity. The reflectivity scale (Ref) has been normalized between 0 (white, low reflectivity) and 1 (black, high reflectivity). Active spreading centers tend to be highly reflective. (Refer also to Fig. 1.2 for a list of plate boundary names). No narrow plate boundary connecting the CLSC to the FRSC can be identified in the acoustic reflectivity map.

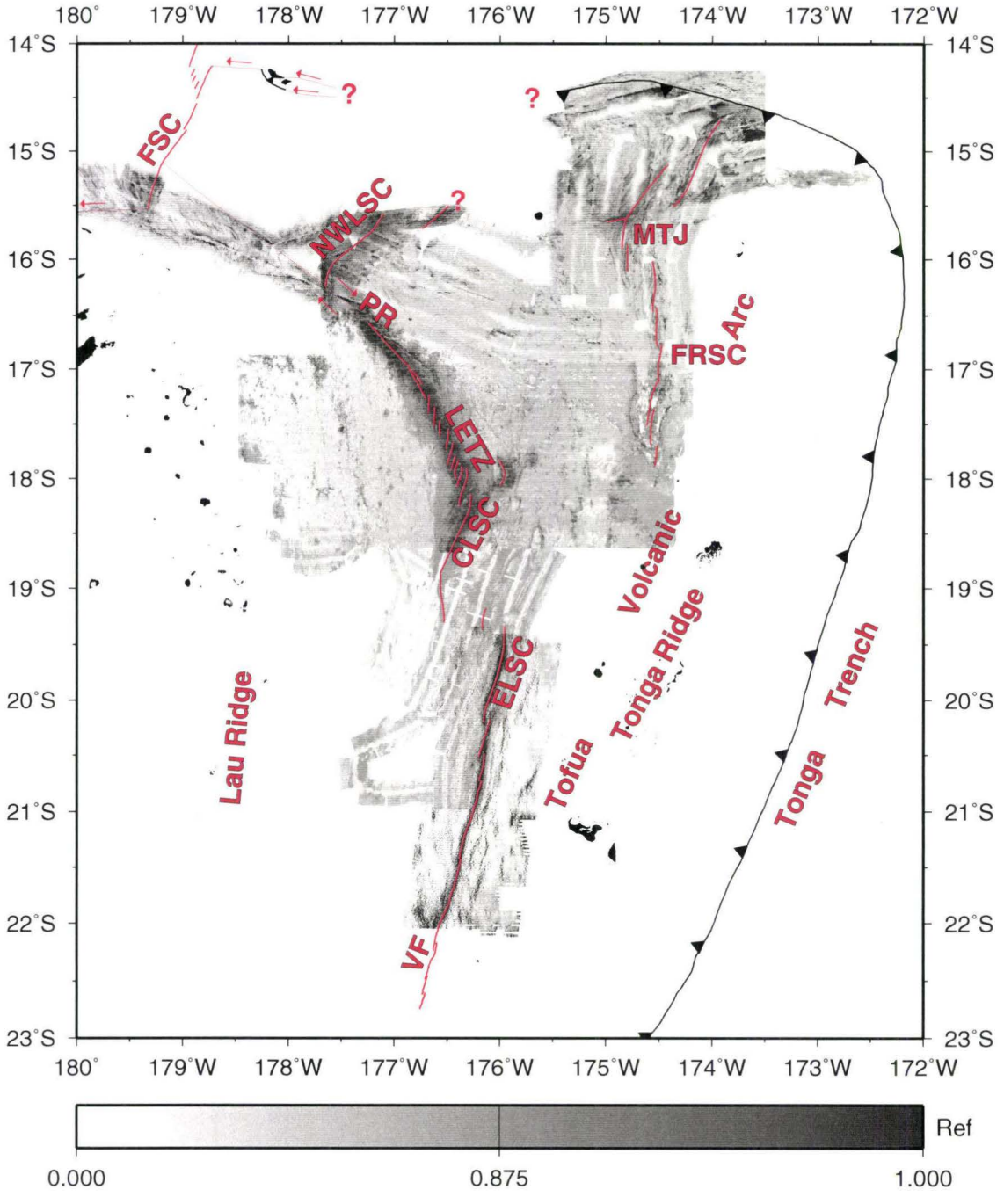
180°
179°W
178°W
177°W
176°W
175°W
174°W
173°W
172°W
14°S
15°S
16°S
17°S
18°S
19°S
20°S
21°S
22°S
23°S
FSC
NWLSC
PR
LETZ
CLSC
ELSC
VF
MTJ
FRSC Arc
Volcanic
Tonga Ridge
Tonga Trench
Lau Ridge
Tofua
?
Ref
0.000
0.875
1.000

Fig. 1.12. Lau Basin seismicity. Three data sets are plotted: (1) CMT focal mechanisms ( ); (2) ISC shallow earthquakes (+); (3) OBS surveyed microquakes (Eguchi et al., 1987.) (·). The band of seismicity trending NE of the CLSC is interpreted to be associated with the southern boundary of the Niuafo'ou Microplate. (Refer also to Fig. 1.2 for a list of plate boundary names).

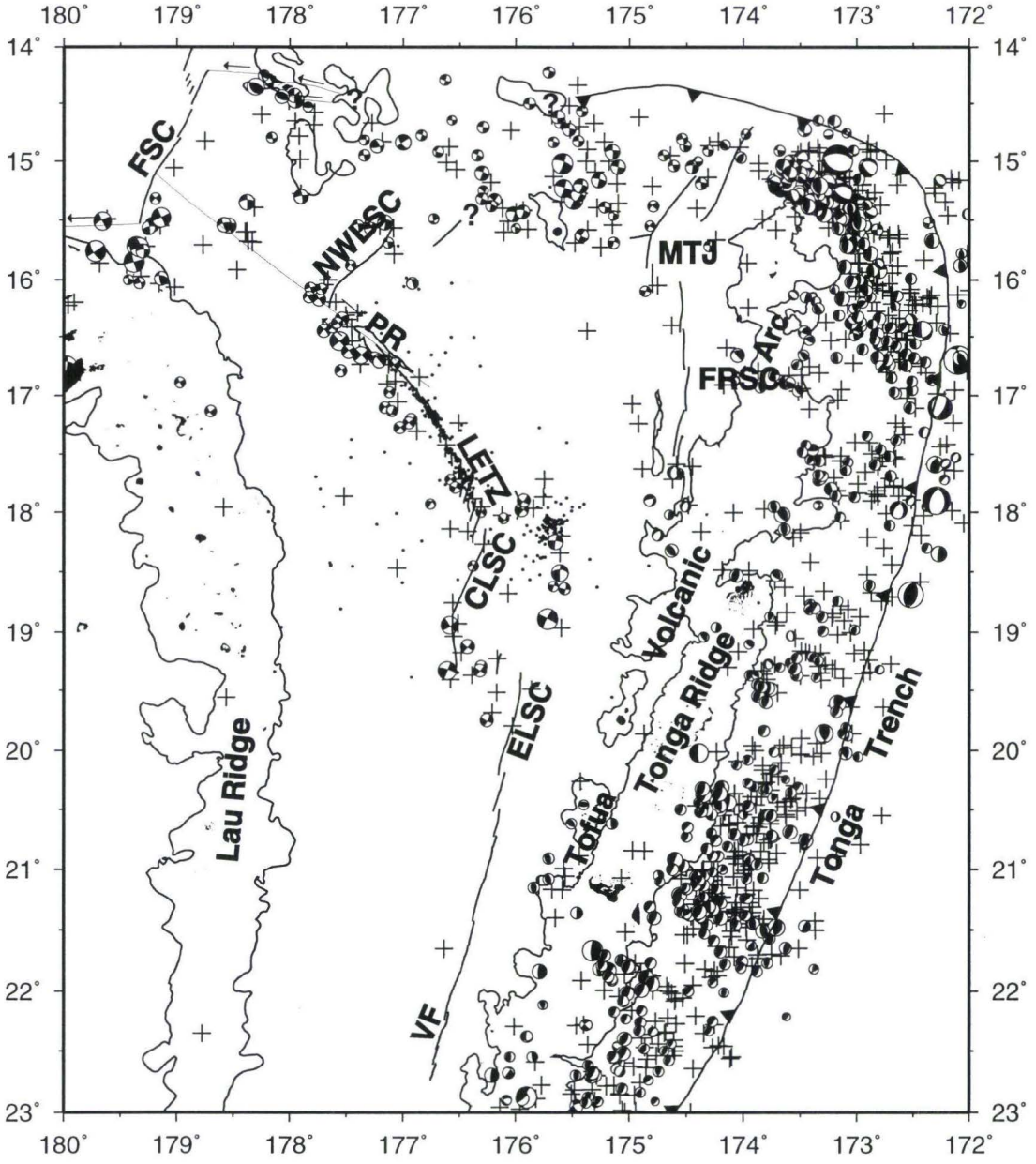
180°
179°
178°
177°
176°
175°
174°
173°
172°
14°
15°
16°
17°
18°
19°
20°
21°
22°
23°
FSC
NWBSC
PR
LETZ
CLSC
ELSC
VF
Lau Ridge
Volcanic
Tonga Ridge
Trench
Tonga
Arc
MTJ
FRSC
Tofua

Fig. 1.13. Proposed Plate Model. A=Australian Plate, N=Niuafo'ou Microplate, T=Tongan Plate. The main A-T boundary is plotted in green. In addition, geodetic vectors describing A-T relative plate motion (in mm/yr) are plotted as green arrows. The main A-N boundary is plotted in red, and the main N-T boundary is plotted in blue. Gray areas are regions of positively magnetized crust. (Refer also to Fig. 1.2 for a list of plate boundary names).

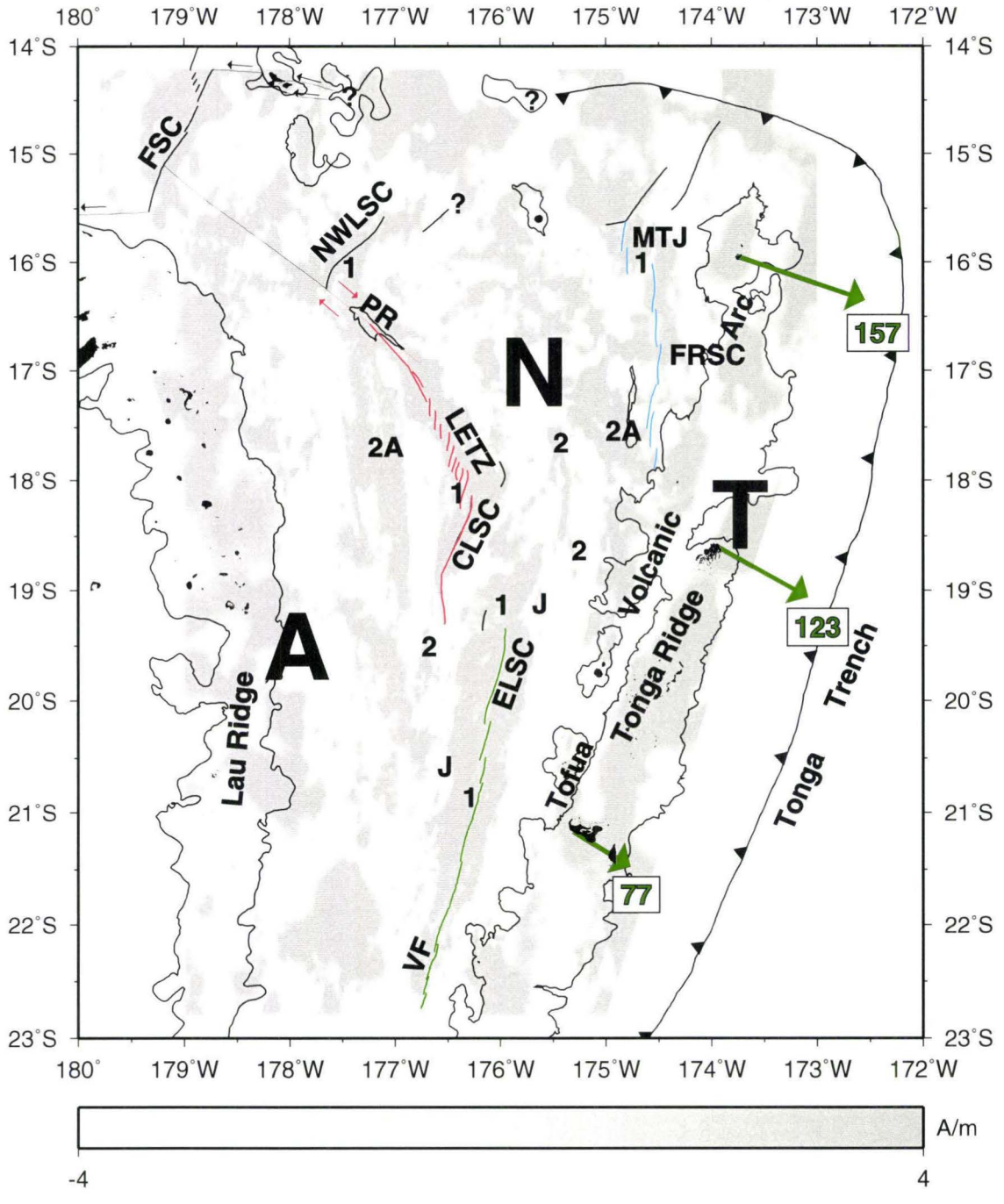
180°
179°W
178°W
177°W
176°W
175°W
174°W
173°W
172°W
14°S
15°S
16°S
17°S
18°S
19°S
20°S
21°S
22°S
23°S
FSC
NWLSC
PR
LETZ
CLSC
ELSC
VF
MTJ
FRSC
Arc
Volcanic
Tonga Ridge
Tonga Trench
Lau Ridge
Tofua
N
A
T
2A
2
1
J
?
157
123
77
A/m
-4
4

CHAPTER 2. DATA PROCESSING AND COMPILATION

2.1 Introduction

The four main data sets that pertain to this study are bathymetry, magnetic anomalies, acoustic imagery, and seismicity. Of the four, compiling the bathymetry data was the most complicated process due to the large amounts of overlap in the available data. Magnetic anomalies could not be easily identified until a magnetization inversion was completed (Taylor et al., 1996). Details of plate boundary locations and their associated morphology were recognized and mapped after four sets of acoustic imagery sonar data of varying quality were joined. Earthquake epicenters help define the location of active plate boundaries and rifting regimes. Strike-slip vectors and T-Axes of normal faults obtained from focal mechanisms constrain the sense of relative plate motion.

2.2 Bathymetry Data Processing and Compilation

Lau Basin bathymetric data has been collected since at least the 1950s. As data acquisition methods have improved, the resolution and accuracy of the data sets has greatly increased. Data sets of differing quality were used to construct the detailed bathymetric map presented in Fig. 1.2.

2.2.1 Main Data Sets

The main Lau Basin bathymetric data sets fall into four broad categories: (1) regional, (2) digitized (3) single-beam and (4) swath bathymetry. Regional data (Fig. 2.1) consists of a relatively low resolution 2 arc-min grid of predicted bathymetry (Smith and Sandwell, 1997) and a detailed "zero-depth"

Fig. 2.1. Regional predicted bathymetry map of the Lau Basin (Smith and Sandwell, 1997). Resolution is 2 arc-min. Depth scale is in km.

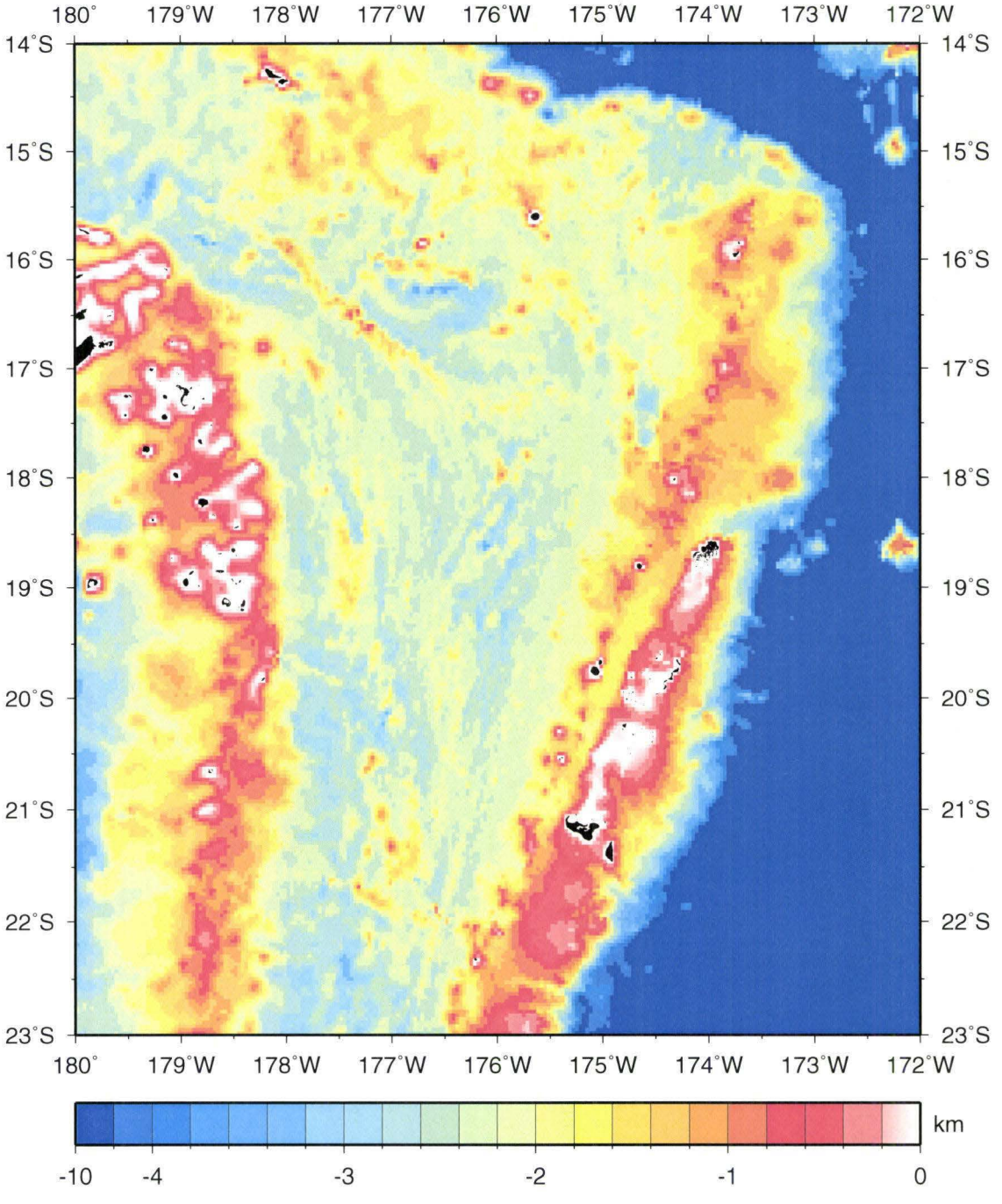
180°
179°W
178°W
177°W
176°W
175°W
174°W
173°W
172°W
14°S
15°S
16°S
17°S
18°S
19°S
20°S
21°S
22°S
23°S
km
-10
-4
-3
-2
-1
0

shoreline file that originates from two sources: (1) the World Vector Shorelines (WVS) and (2) the CIA World Data Bank II (WDBII). Table 2.1 lists a collection of various miscellaneous digitized data sets. The location of these data sets is plotted in Fig. 2.2. The single-beam data sets have two sources: (1) MGD77-formatted data files from the National Geophysical Data Center (NGDC) and (2) ASCII-formatted bathymetric data files from the South Pacific Applied Geoscience Commission (SOPAC). Table 2.2 lists source information pertaining to 16 cruises that have collected very high resolution (200 m or better) swath bathymetry in the Lau Basin over the past two decades. Fig. 2.3 plots both the single-beam data tracks and the center beam of the swath data tracks and illustrates the large amount of data available for the area. Fig. 2.4 shows the approximate extent of the various swath bathymetry data that was used in the compilation.

Location	**Source**
Lau Ridge	Defense Mapping Agency: "Fiji Iles de Horne 83034"
Tonga Ridge	Defense Mapping Agency: "Tonga Islands 83560"
CLSC	Wiedicke and Collier, 1993 (Cruises: SO-35, SO-48, SO-67)
VF	Wiedicke and Habler, 1993 (Cruises: SO-35, SO-48, SO-67)

Table 2.1. Sources of digitized data used in the bathymetric compilation.

2.2.2 Data Editing

Detecting errors within the bathymetric data sets requires familiarity with the both the data itself and the regional geology. Single-beam track data sets were analyzed individually and compared with the other available data sets. Obvious "bad" tracks (or pieces of tracks) were identified and removed

Fig. 2.2. Location of digitized data sets used in the Lau Basin bathymetric compilation.

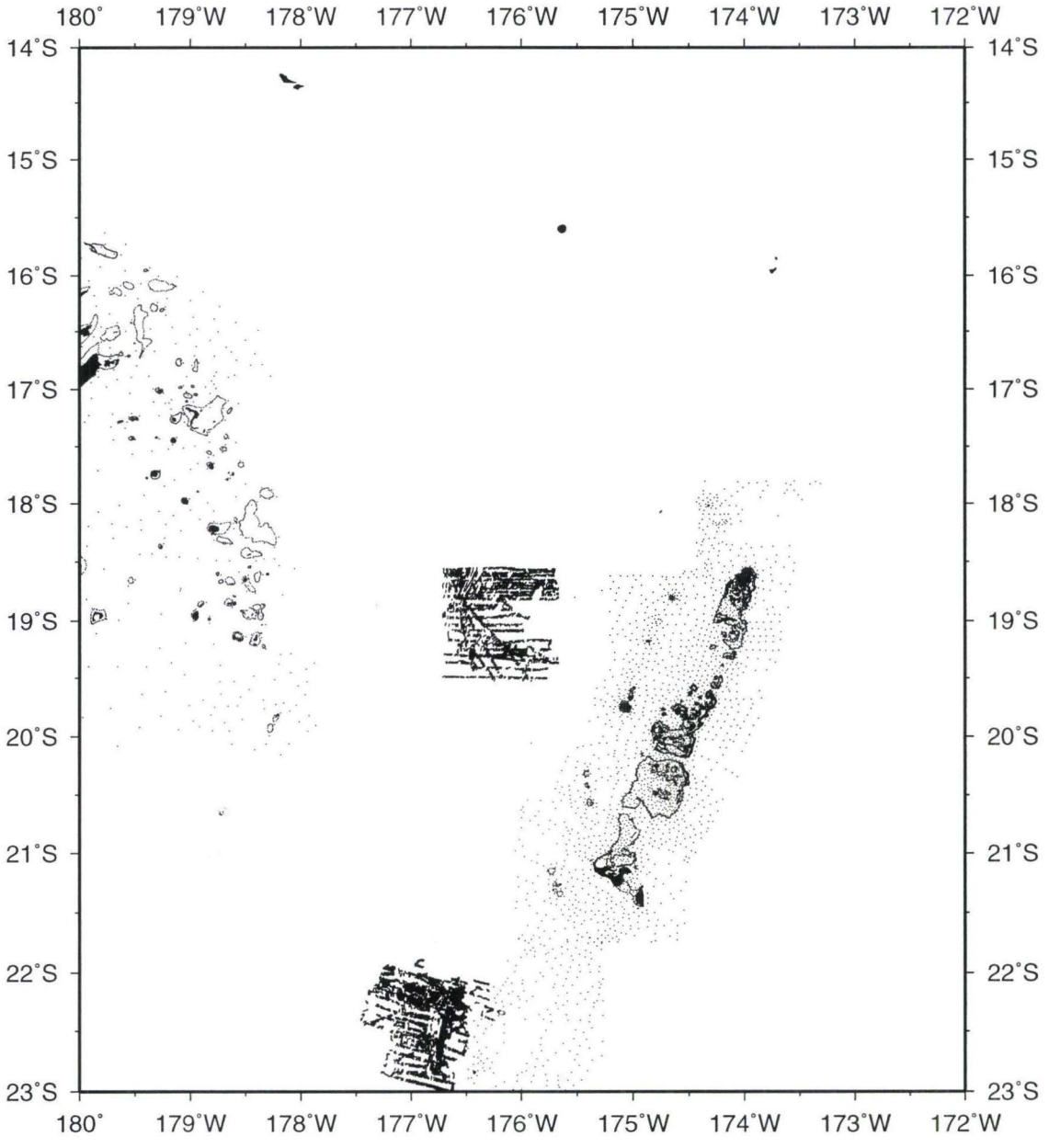
180°
179°W
178°W
177°W
176°W
175°W
174°W
173°W
172°W
14°S
15°S
16°S
17°S
18°S
19°S
20°S
21°S
22°S
23°S

Cruise	Year Collected	Ship
BMRG08	1996	R/V *Melville*
CK8915	1989	HMAS *Cook*
EW9106	1991	R/V *Ewing*
EW9512	1995	R/V *Ewing*
EW9914	1999	R/V *Ewing*
HM9507	1995	R/V *Hakurei Maru #2*
MW9603	1996	R/V *Moana Wave*
MRTN06WT	1984	R/V *Washington*
PPTU04WT	1986	R/V *Washington*
PPTU05WT	1986	R/V *Washington*
RNDB14WT	1989	R/V *Washington*
RNDB15WT	1989	R/V *Washington*
WEST05MV	1994	R/V *Melville*
WEST06MV	1994	R/V *Melville*
WEST12MV	1995	R/V *Melville*
Y9614	1997	R/V *Yokosuka*

Table 2.2. Information regarding swath data used in the bathymetric compilation.

Fig. 2.3. Track chart of single-beam data and centerbeam profiles of swath bathymetric data.

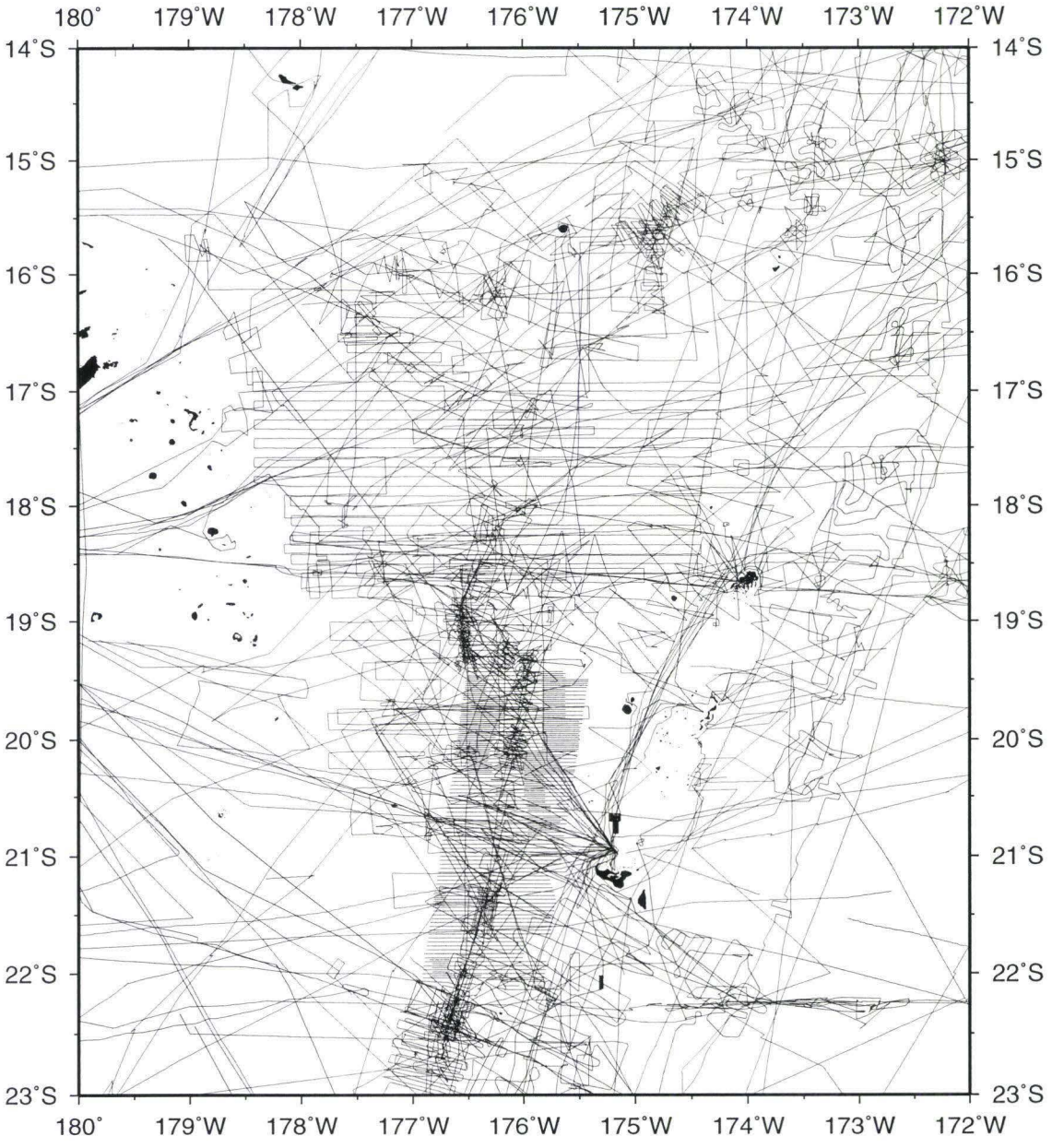
180°
179°W
178°W
177°W
176°W
175°W
174°W
173°W
172°W
14°S
15°S
16°S
17°S
18°S
19°S
20°S
21°S
22°S
23°S

Fig. 2.4. Approximate extent of swath bathymetry data available for the Lau Basin. Resolution is 200m. Depth scale is in km.

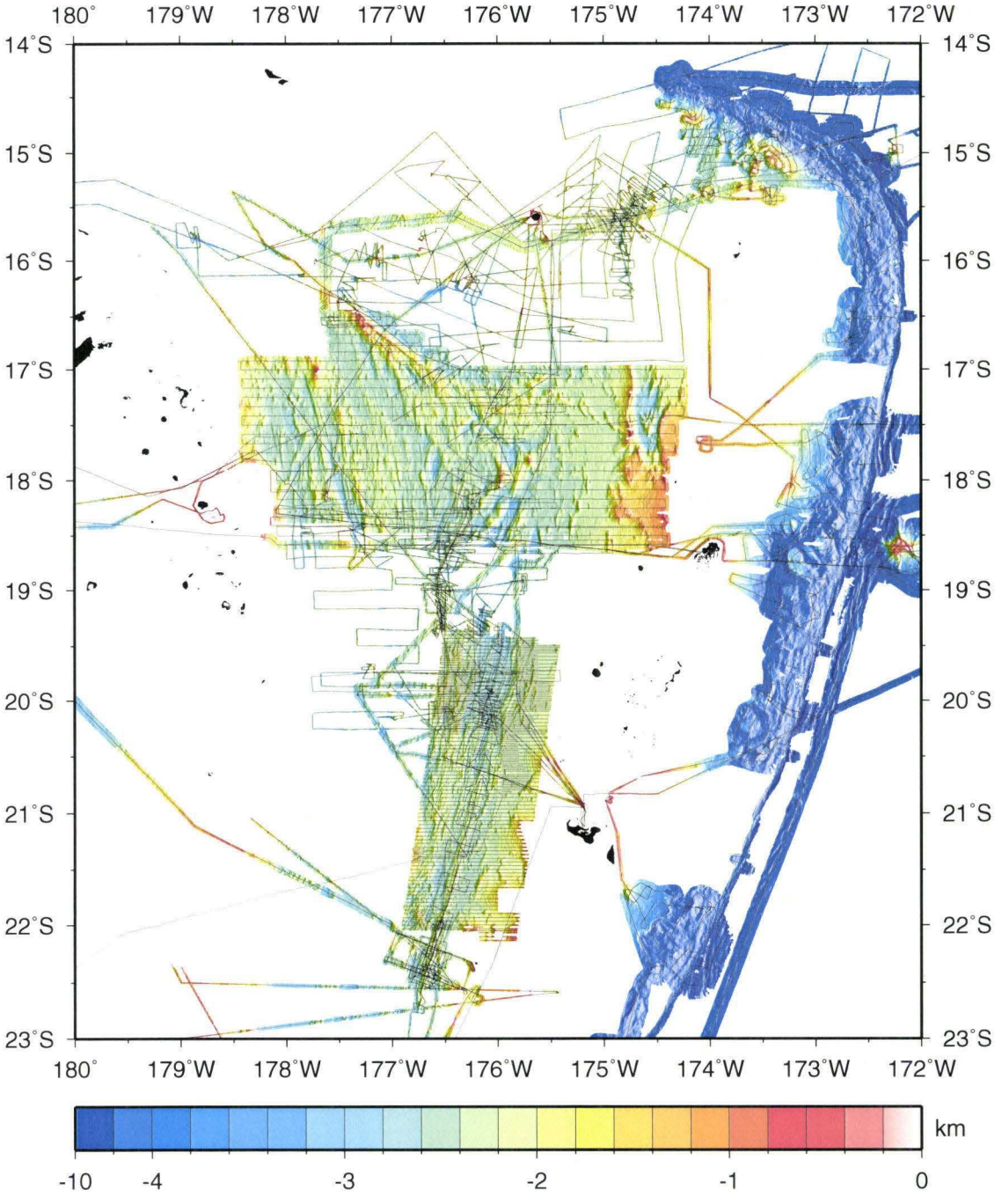
180°
179°W
178°W
177°W
176°W
175°W
174°W
173°W
172°W
14°S
15°S
16°S
17°S
18°S
19°S
20°S
21°S
22°S
23°S
km
-10
-4
-3
-2
-1
0

from the main data set (Fig. 2.5). Unfortunately, the predicted bathymetry is also affected by "bad" tracks that were not removed from the ship-board data set prior to its inversion. Therefore, it was necessary to keep the identified "bad" tracks and use them as a guide for removing poor data from the predicted bathymetric data set. To do this, first a 3X3 arc-min gaussian filter was passed over the "bad" tracks (thus widening the tracks slightly). The locations of this widened track were used as the guide for removing bad data from the "underlying" predicted bathymetry grid.

In a similar manner, the filtered positions of all ship tracks, digitized data, and shoreline data are removed from the predicted bathymetry. The purpose of this step is to avoid interference between the lower resolution predicted bathymetry data and the higher resolution single-beam, digitized and shoreline information during the final gridding process. This process forces the two data sets to become mutually exclusive. When they are ultimately combined, the resultant grid is unaffected by the lower resolution data in areas where the higher resolution data are available.

Finally, the predicted bathymetry grid was "warped" to meet a 2 arc-min shipboard data grid via a simple method of differencing the two grids, filtering these differences (using a 15 arc-min gaussian filter), and adding the result back into the predicted grid. The warping of the predicted bathymetry grid rarely produced changes of more than 200m. The final edited predicted bathymetry is plotted in Fig. 2.6. The complete process used to create the gaps and warp the predicted bathymetry grid was conducted using the Generic Mapping Tools (GMT) software package (Wessel and Smith, 1991).

The swath data also needed to be analyzed and subjectively edited. This editing phase required that each individual day file of all swath cruises

Fig. 2.5. Track chart of bathymetry and/or navigation data identified as bad. The errors along these tracks affect the regional predicted bathymetry plotted in Fig 2.1. These tracks are used solely as a guide to remove the artifacts that they caused in the original predicted bathymetry.

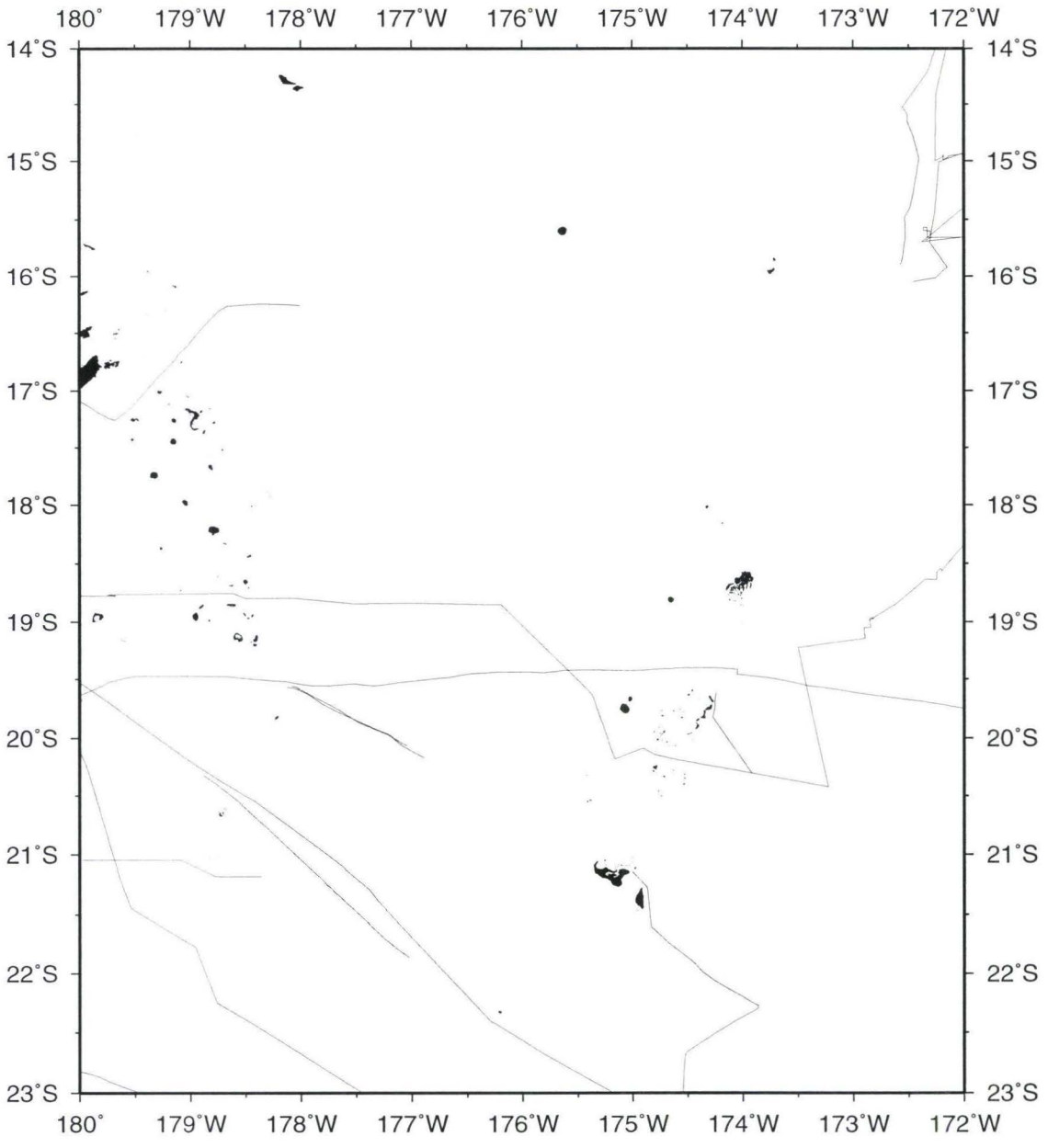
180°
179°W
178°W
177°W
176°W
175°W
174°W
173°W
172°W
14°S
15°S
16°S
17°S
18°S
19°S
20°S
21°S
22°S
23°S

Fig. 2.6. Edited regional predicted bathymetry. The locations of all single-beam, digitized, shoreline data, and tracks identified as bad are first filtered using a 3X3 arc-min gaussian filter resulting in a coarse "widening" of the data positions. These filtered positions are used as a guide to remove data from the original regional predicted bathymetry (Fig 2.1). This edited data set becomes the first "layer" in the bathymetric compilation process. The original single-beam, digitized, shoreline data are added back to the compilation in a later process. Resolution is 2 arc-min. Depth scale is in km.

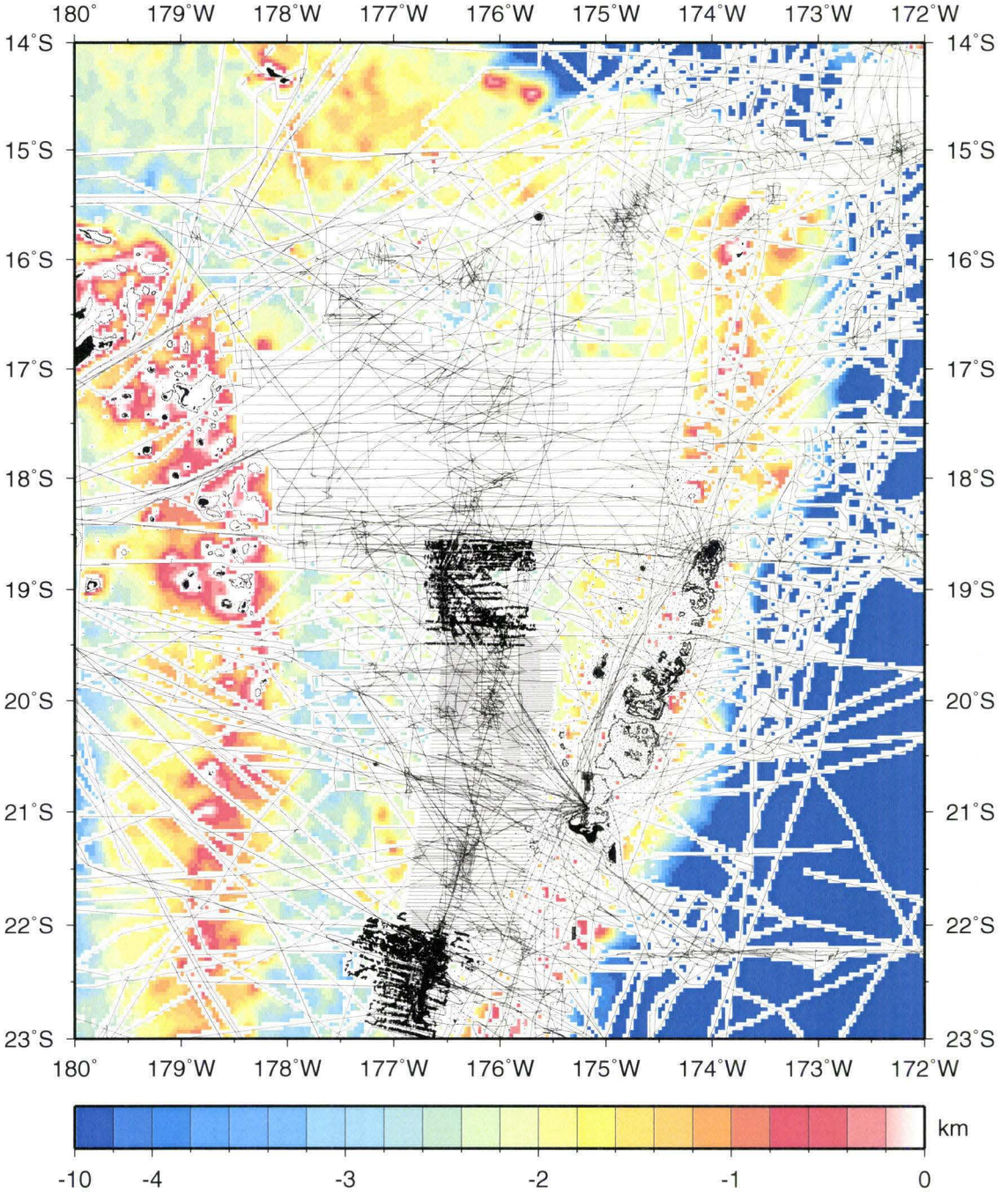
180°
179°W
178°W
177°W
176°W
175°W
174°W
173°W
172°W
14°S
15°S
16°S
17°S
18°S
19°S
20°S
21°S
22°S
23°S
km
-10
-4
-3
-2
-1
0

be studied. Outer beams that were causing edge effects and/or whole portions of the swath were removed using MB-system (Caress, 1995) where data merging was poor. Basically this process was an iterative one, i.e., the data were compiled, obvious gross errors in the resultant image were located, corrections were made to the data set, and the edited data set was then compiled again until the input was as artifact-free as possible.

2.2.3 Data Compilation

The compilation process brings together all of the data available for the area and outputs a bathymetric grid that is as artifact-free as possible. The main goal is to favor the highest resolution data available where possible. This is accomplished via a "layering" process in which appropriate data sets are allowed to take precedence over other data in the same area. Decisions regarding the hierarchy of the various data sets were determined via trial and error. All of the compilation techniques described in this section rely upon a series of GMT scripts independently developed and written specifically for the Lau Basin.

Initially, all of the edited and cleaned bathymetric data are brought in and gridded as follows: (a) first, a reduced data set is generated by taking median values for 1 arc-min blocks. (b) The reduced data set is combined with the original data and median values are then determined for 0.002° blocks. The purpose of the decimated 1 arc-min data set is to avoid unwanted bathymetric "spikes" in the final image. (c) The 0.002° median values are piped directly into a simple unsurfaced grid to create the base grid in this process. Because all of the data were brought in all at once, no consideration

of the resolution of the various data sets is included at this stage in the process.

To generate the "layering" effect without producing undesirable edge artifacts at data boundaries, a series of swath data sets (identified to be of high quality) are used to create a "hole" of a specific shape and size within the base grid (Fig. 2.7). The hole is purposefully created to be slightly larger than the data set used to guide it. The high quality data is then added back into the hole, and this new data set (now free of unnecessary lower resolution data) is then run through the same 1 arc-min/0.002° median process and gridded again. This process is actually run twice for the area, with the very best data used to generate a second hole in the semi-processed data (Fig. 2.8). Once the final "best" data is added back in and run through the median process, the resultant 0.002° values are then transferred directly into the surfacing algorithms of Smith and Wessel (1990) to generate the final grid used to produce the image shown in Fig. 1.2. Overall, the purpose of the successive hole-generation and layering is twofold: (1) the slight increase in size of the hole vs. the data being added back in guarantees that the final surfacing is as smooth as possible, and (2) many potential unwanted data artifacts are avoided because the lower quality data sets are not allowed to interfere with the preferred data.

The process described above illustrates the main process used, however, it should be noted that due to the large amounts of data, the actual process was forced to be completed in twelve pieces (each buffered with a 0.25° border to avoid edge effects). Ultimately, these twelve areas were joined to generate the final bathymetric map shown in Fig. 1.2.

Fig. 2.7. Swath data determined to be of high quality are filtered and used as a guide to create a "hole" in the compiled bathymetric data set. The purpose of the "hole" is to eliminate regions in the grid that have both low and high resolution data competing for the same grid node locations. Because the swath data is added back in a later process, the final grid will contain only high resolution data in the blank region shown. In addition, the hole is forced to be slightly larger than the location of the original high resolution data, thus guaranteeing that the final surfacing across both types of data is as smooth as possible. Resolution is 200m. Depth scale is in km.

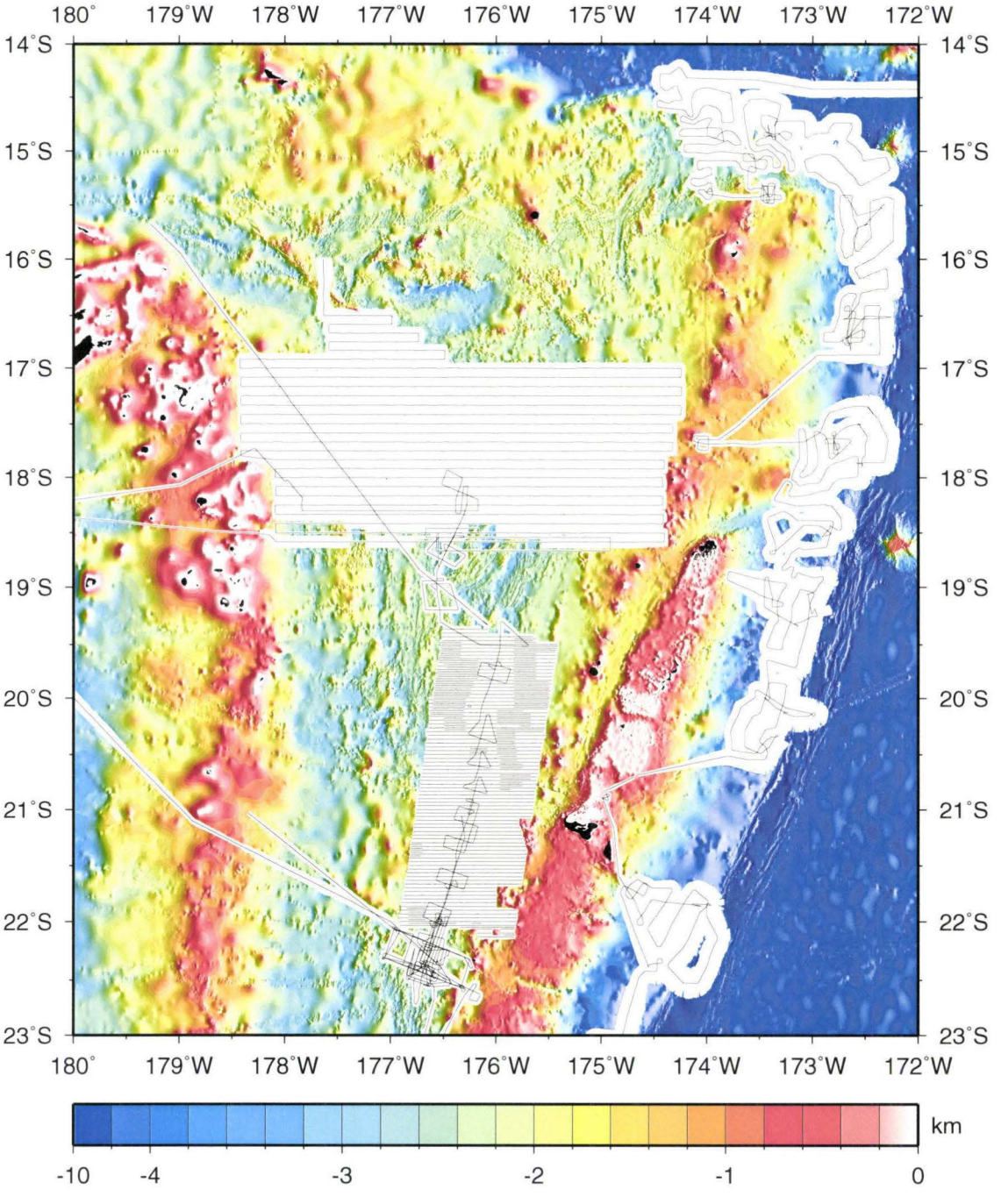
180°
179°W
178°W
177°W
176°W
175°W
174°W
173°W
172°W
14°S
15°S
16°S
17°S
18°S
19°S
20°S
21°S
22°S
23°S
km
-10
-4
-3
-2
-1
0

Fig. 2.8. Second "hole" generated in the Lau Basin bathymetric process. The data added back in to this blank region will take highest precedence in the final image. Resolution is 200m. Depth scale is in km.

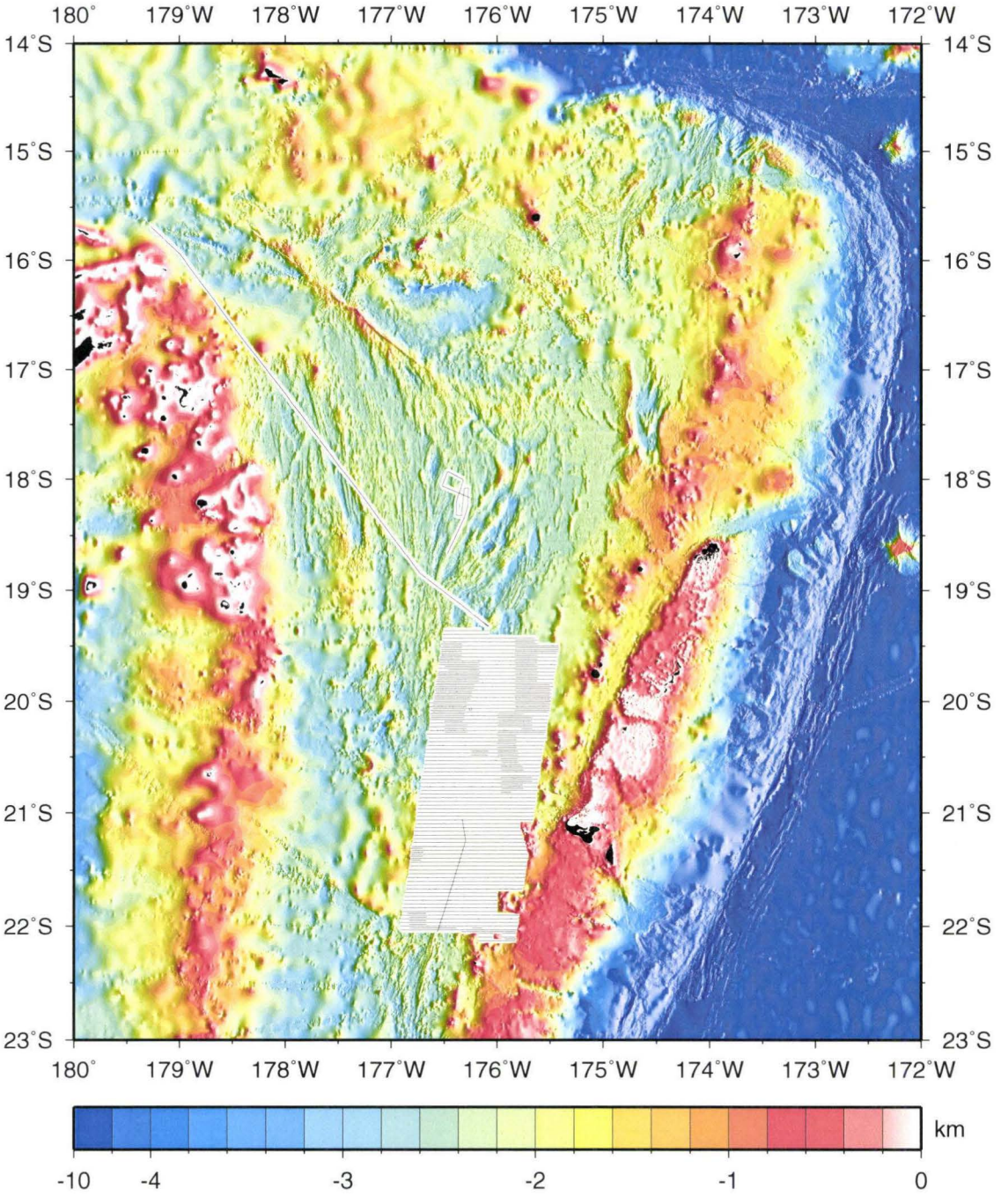
180°
179°W
178°W
177°W
176°W
175°W
174°W
173°W
172°W
14°S
15°S
16°S
17°S
18°S
19°S
20°S
21°S
22°S
23°S
km
-10
-4
-3
-2
-1
0

2.3 Magnetic Data Compilation and Inversion

The Lau Basin magnetic data set is smaller (in number of data points) than the bathymetry data set, and thus much of the editing was also less complicated. The inversion of the gridded magnetic anomalies to create the magnetization grid is the most important step in this process as the result clearly highlights anomaly boundaries important to this study.

2.3.1 Main Data Sets

The main Lau Basin magnetic data sets fall into two broad categories: (1) shipboard and (2) aeromagnetic. Both data sets used in this compilation come from the NGDC. During the years 1977-1979, the Naval Research Laboratory (NRL) conducted a series of aeromagnetic surveys of the Lau Basin. Shipboard marine magnetic tracks are shown in Fig. 2.9, and the NRL flight lines are plotted in Fig. 2.10.

2.3.2 Data Editing and Compilation

The shipboard magnetic data are assumed to be the more reliable data set in this compilation for to two reasons: (1) there is less ambiguity in true distance from the seafloor, and (2) better navigation. To additionally improve the internal consistency of the marine magnetic data, it was necessary to perform cross-over analysis with the 1986 cruise PPTU04WT, chosen for its extent throughout the basin. Discrepancies in magnetic values at cross-over points were determined and eliminated.

To grid the magnetic data, the process used is similar to that for the bathymetry. First, the marine magnetic data *alone* are reduced into median

Fig. 2.9. Track chart of shipboard magnetic data for the Lau Basin, after cross-over corrections were completed. Positive magnetic anomalies are plotted in red; negative magnetic anomalies are plotted in blue.

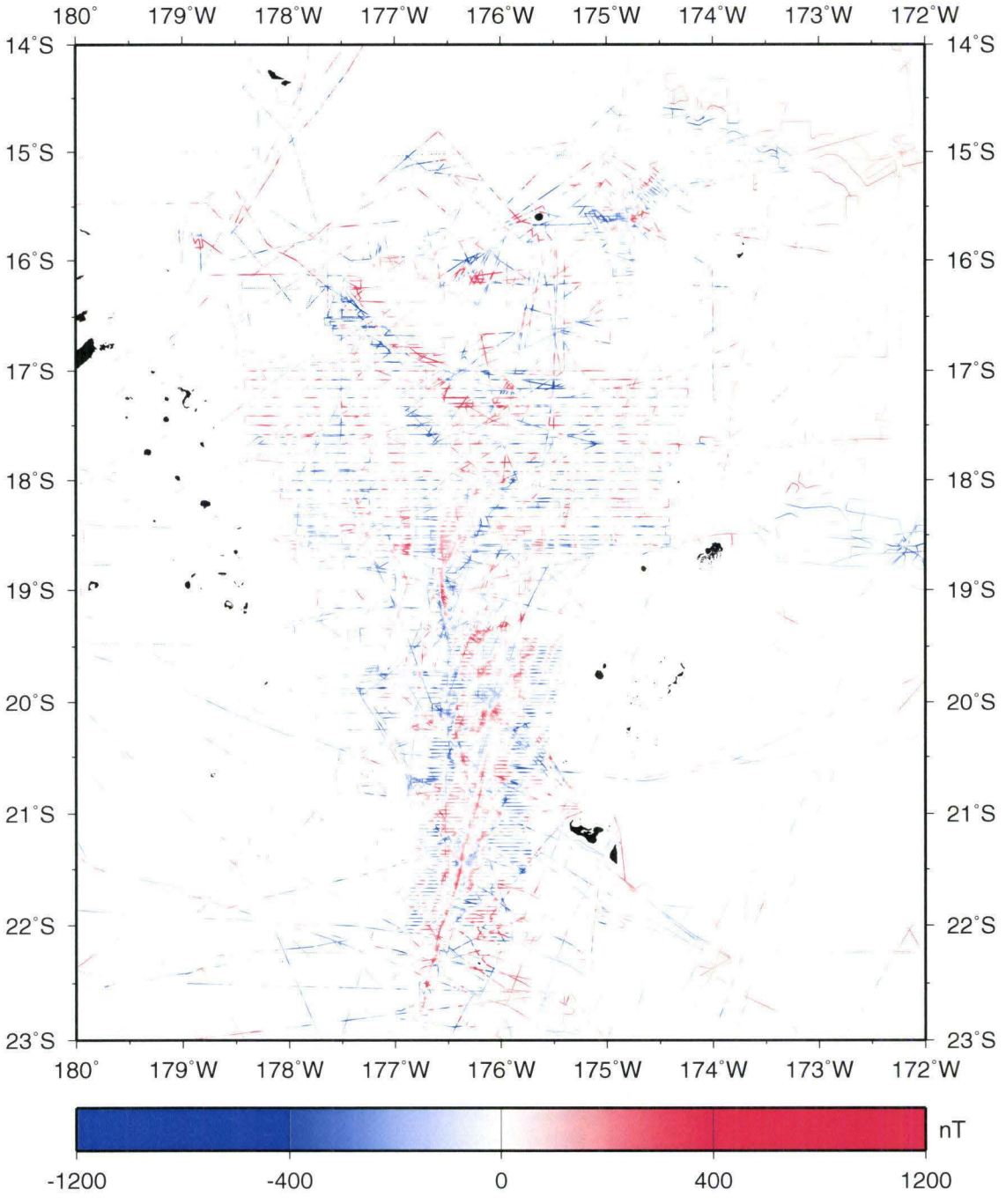
180°
179°W
178°W
177°W
176°W
175°W
174°W
173°W
172°W
14°S
15°S
16°S
17°S
18°S
19°S
20°S
21°S
22°S
23°S
nT
-1200
-400
0
400
1200

Fig. 2.10. Track chart of flight lines for the 1977-1979 NRL aeromagnetic survey, after editing. Cross-over analysis with the marine magnetics allowed for small adjustments to be made to the navigation of seventeen of the flight lines. Positive magnetic anomalies are plotted in red; negative magnetic anomalies are plotted in blue.

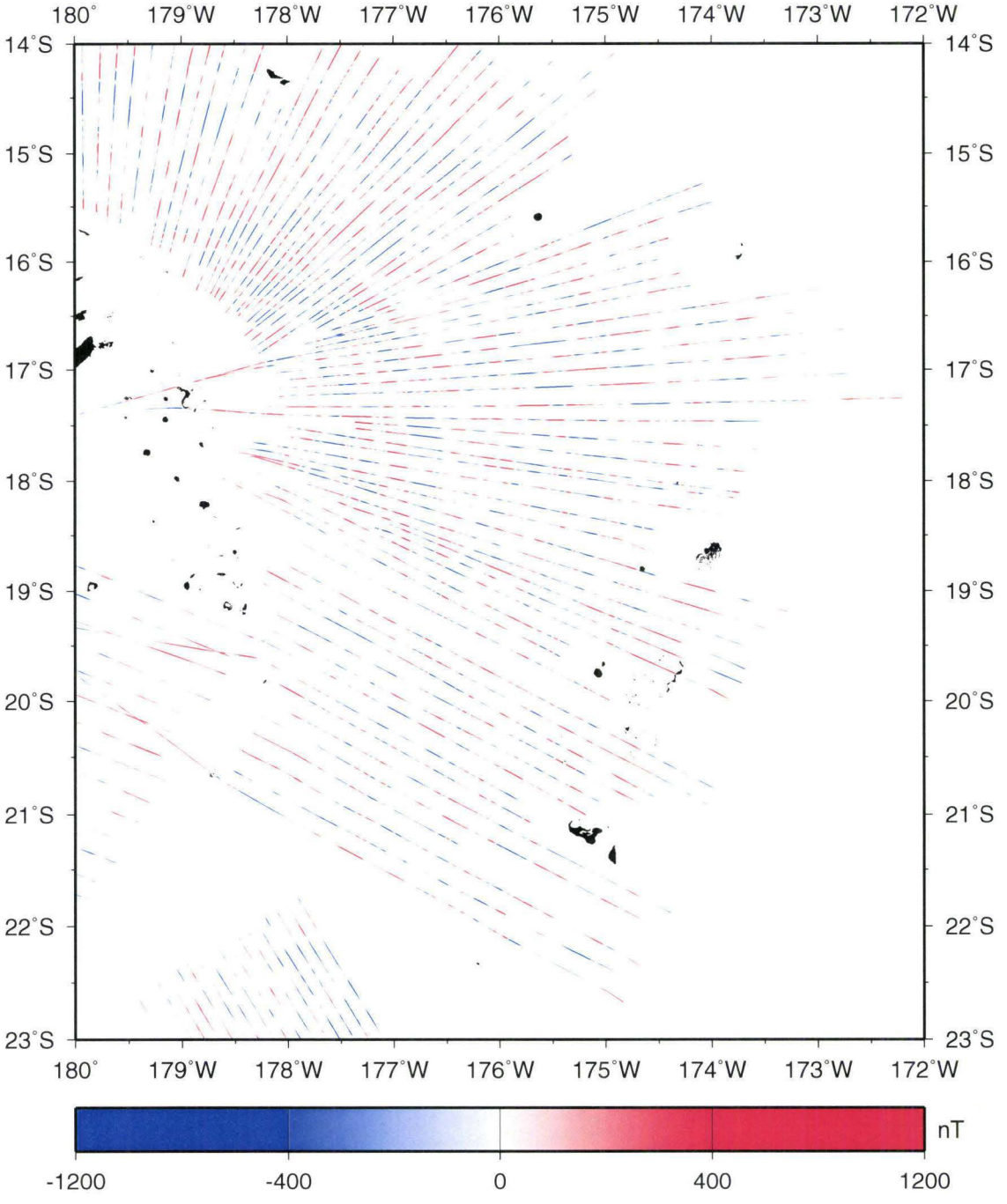
180°
179°W
178°W
177°W
176°W
175°W
174°W
173°W
172°W
14°S
15°S
16°S
17°S
18°S
19°S
20°S
21°S
22°S
23°S
nT
-1200
-400
0
400
1200

values for 10 arc-min blocks. Then median values in 1 arc-min blocks are calculated for the 10 arc-min reduced data and the original marine data. This 1 arc-min data are then gridded using the same surfacing program as for the bathymetry. The marine magnetic data grid is stored for use with making corrections to the aeromagnetic data.

The aeromagnetic data, although considered to be reasonably self-consistent, did require a few adjustments prior to its compilation with the marine magnetic data. Following cross-over analysis between the aeromagnetic data and the gridded marine data, navigation adjustments were made to 17 flight lines. Poor aeromagnetic data were identified and removed. In addition, a consistent planar increase in values to the north was removed in stages from the aeromagnetic data set. Finally, the resultant aeromagnetic data was again compared to the marine magnetic data grid and was consistently lowered to fully match with the marine magnetic grid.

As a final step, the cleaned and edited shipboard and aeromagnetic data were run through the 10 arc-min/1 arc-min median process (described above for the marine magnetic data) and surfaced to produce the magnetic anomaly grid imaged in Fig. 2.11.

2.3.3 Magnetization Inversion

The distribution of source rock magnetization can be inferred indirectly by inverting the gridded magnetic anomaly data and bathymetric data. Although magnetic lineations do appear in the anomaly grid (Fig. 2.11), completing a magnetization inversion further aids in recognizing true anomaly boundaries. A magnetization inversion (a) corrects for known skewness in the magnetic field and (b) accounts for variations in the source

Fig. 2.11. Lau Basin magnetic anomaly compilation results. Positive magnetic anomalies are plotted in red; negative magnetic anomalies are plotted in blue. The anomalies are additionally highlighted ("sunlit" from the east) to emphasize their location. Resolution is 1 arc-min.

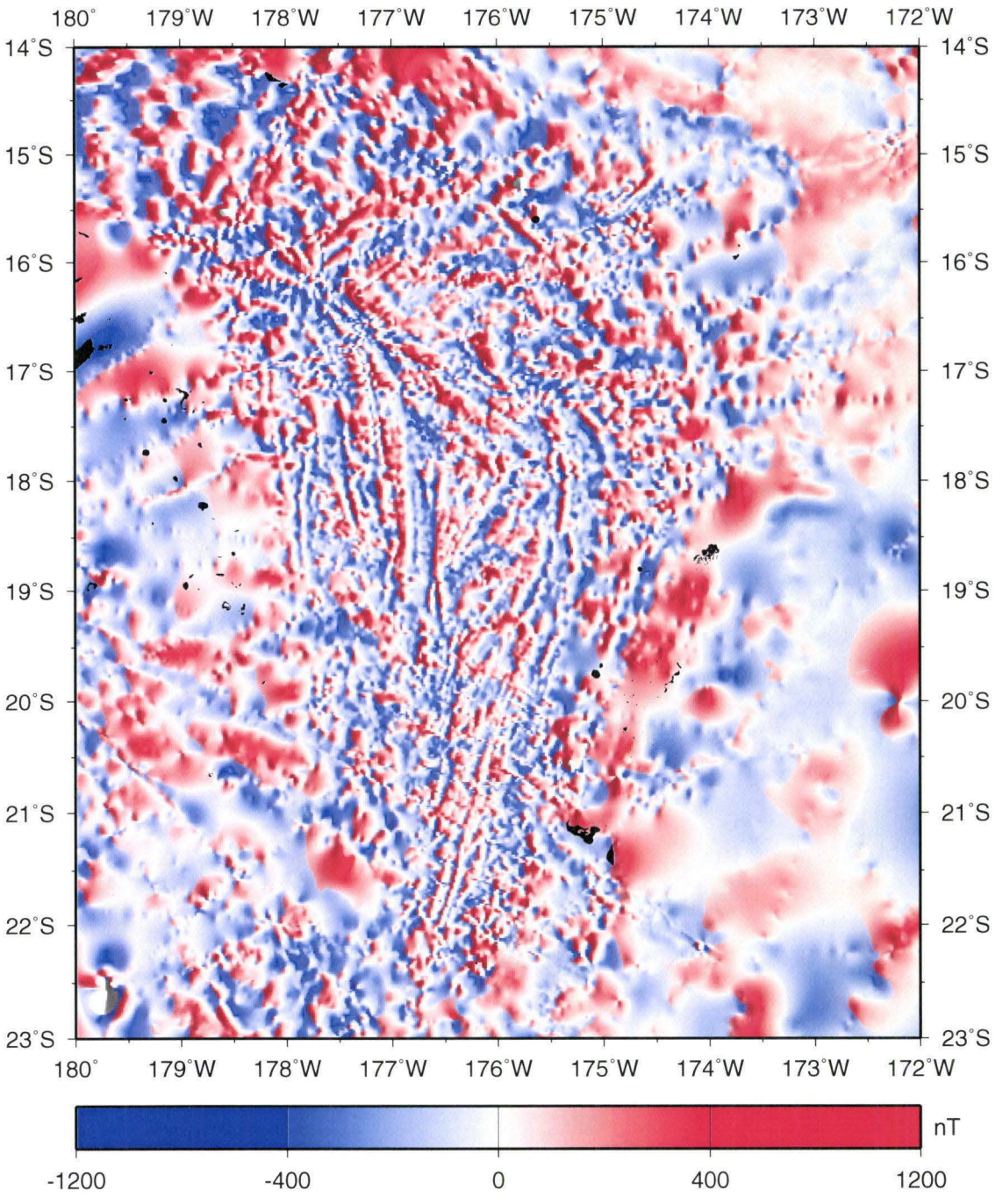
180°
179°W
178°W
177°W
176°W
175°W
174°W
173°W
172°W
14°S
15°S
16°S
17°S
18°S
19°S
20°S
21°S
22°S
23°S
nT
-1200
-400
0
400
1200

layer depth. Both the magnetic anomaly and the bathymetry grids are inputs to the inversion process. The magnetic source layer in this inversion was assumed to be 1 km in thickness beneath the known seafloor surface topography. The inversion method details are more fully described by Parker and Huestis (1974). This method has previously been employed in the Mariana Basin (Martinez et al., 1995) where magnetic lineations were brought into sharper contrast by the process. Current magnetization inversion results for Lau Basin are shown in Fig. 2.12.

2.4 Acoustic Imagery Processing

The acoustic imagery map shown in Fig. 1.11 was generated by Andrew Goodliffe from data compiled by Brian Taylor. Only four cruises (Table 2.3) collected acoustic data. Data quality varies due to the differences in acquisition methods. Each data set was ultimately rasterized and compiled in GMT.

Cruise	Year Collected	Ship	System
CK8915	1989	HMAS *Cook*	GLORIA
HM9507	1995	R/V *Hakurei Maru #2*	Hydrosweep
MW9603	1996	R/V *Moana Wave*	HMR1
CD3388	1988	RRS *Charles Darwin*	GLORIA

Table 2.3. Information regarding cruises that collected acoustic imagery data.

Fig 2.12. Map of Lau Basin magnetization. Although magnetic lineations do appear in the anomaly grid (Fig. 2.11), the magnetization inversion further aids in recognizing true anomaly boundaries. This inversion assumed a 1 km thick source layer beneath the bathymetry (Fig. 1.2). Positively magnetized crust is plotted in red; negatively magnetized crust is plotted in blue. The lineations are additionally highlighted ("sunlit" from the east) to emphasize their location. Resolution is 1 arc-min.

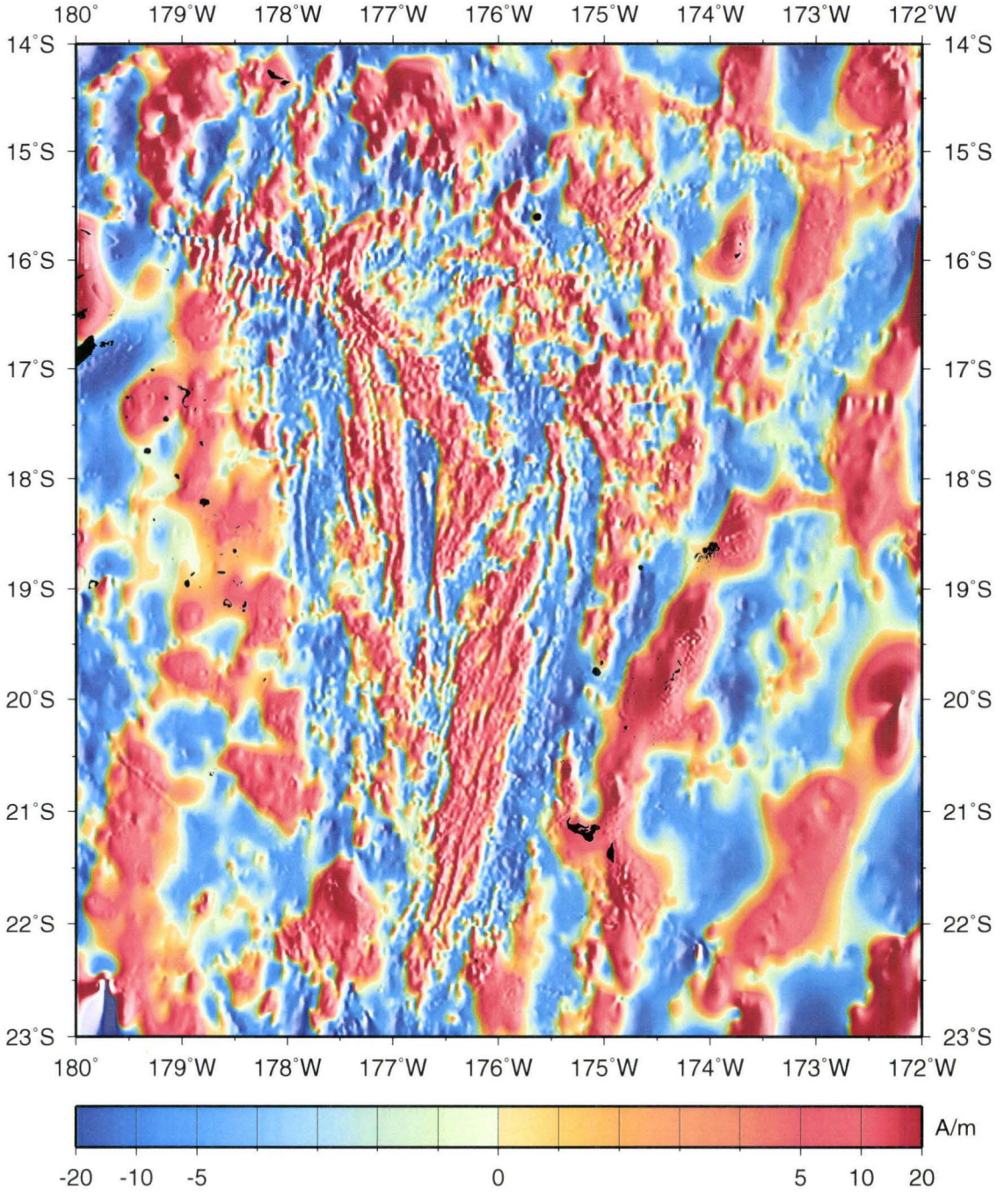
180°
179°W
178°W
177°W
176°W
175°W
174°W
173°W
172°W
14°S
15°S
16°S
17°S
18°S
19°S
20°S
21°S
22°S
23°S
A/m
-20
-10
-5
0
5
10
20

2.5 Seismicity Compilation and Associated Calculations

Three main seismicity data sets exist for the Lau Basin (Fig. 1.12): (1) Centroid Moment Tensor (CMT) focal mechanisms (as compiled by Pelletier et al., 1998), (2) a set of shallow earthquakes from the International Seismological Center (ISC), and (3) microearthquake locations ascertained from an Ocean Bottom Seismometer (OBS) survey that took place in 1984 (Eguchi et al., 1987). T-axes and slip vectors associated with the strike, dip and rake values of the focal mechanisms were calculated.

CHAPTER 3. KINEMATIC MODELING

3.1 Introduction

The main goal of our kinematic model is to determine Euler poles that describe relative motion between tectonic plates. The Euler pole position is a physical point on the earth that acts as a pivot point for the motion of two plates relative to each other (Cox, 1986). The Euler pole is unique in that it is the only point that remains stationary relative to either plate in the system. Specifying an Euler pole location and angular rotation rate is the most compact way to describe the relative plate motion.

In a plate tectonic realm, the Euler pole can be located through analysis of the geometry of the boundary between the plates and the systematic change in relative plate velocity throughout the plate. For example, Fig. 3.1 (a) illustrates a simple schematic two-plate system in which the Euler pole (E) has been located. The pole describes two main geophysical features: (1) transform faults theoretically subtend small circles about the pole and (2) the relative plate velocities systematically increase away from the pole (at the pole itself, velocity drops to zero). In addition to the *location* of an Euler pole, one must specify an *angular rate*, ω to complete the full description of plate motion in the system. The value of ω determines how fast the plates are moving relative to each other.

In a theoretical three-plate system on a globe (Fig. 3.1 (b)) the relative motions between the three plates are described by three unique Euler poles. The total motion between the three plates must sum to zero, i.e. the poles must satisfy the following vector summation equation:

Fig. 3.1. Illustrations of Euler poles in plate tectonic settings (reproduced from Cox (1986)). (a) Simple two plate scenario. Tranform faults theoretically lie on small circles subtended about the pole (E). Plate velocity (shown as arrows) systematically increases away from the pole. (b) Three plate scenario on a sphere. Angular rate ( ) describes the speed at which each of the the plates is moving relative to each other. (c) The three Euler poles all lie on a great circle when they meet three-plate closure criteria (i.e., all relative plate velocity vectors sum to zero.)

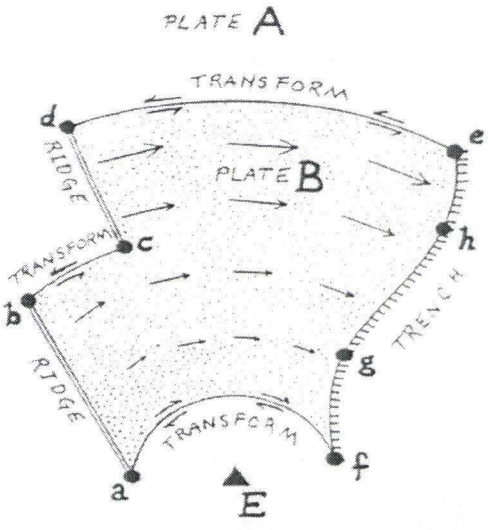
PLATE A
TRANSFORM
d
e
RIDGE
PLATE B
TRANSFORM
c
h
b
TRENCH
RIDGE
g
TRANSFORM
a
f
E

(a)

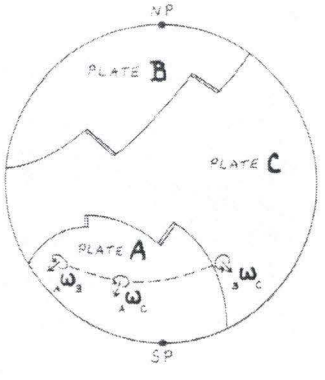
NP
PLATE B
PLATE C
PLATE A
SP

(b)

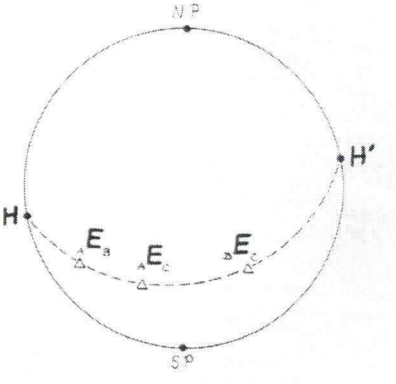
NP
H'
H
SP

(c)

$$_A\omega_C = {}_A\omega_B + {}_B\omega_C \quad (1)$$

where A, B, and C are three theoretical plates, and $_A\omega_C$ should be read as "The motion of plate C relative to plate A". In physical terms, equation (1) means that the three Euler poles that describe the motion on each of the three respective plate boundaries must lie on a great circle (Fig. 3.1 (c)).

In this study, we carry out a kinematic analysis of a three-plate system for the Lau Basin. The main goal in this kinematic model is to find the three poles of opening that can match a variety of disparate geophysical features throughout the basin and simultaneously meet the three-plate closure criteria of Eqn. (1). The following Lau Basin observations are used as model constraints: (1) spreading rates (finite over 0.78 Ma and/or GPS relative velocities), (2) focal mechanisms (either T-axes or slip directions), and (3) ridge and transform fault azimuths.

Finding poles of opening for the Lau Basin was difficult, in part because there is only one transform fault (PR) in the area. In addition, PR lacks significant curvature, which further increases the difficulty in locating poles of opening. The magnetization images, however, are quite clear, thus it was possible to pick reasonable locations for the outer edges of the 0.78 Ma Brunhes crustal anomaly where appropriate. Although focal mechanisms are fairly abundant in the region, earthquake epicenters are not located by a local seismic network, so their locations have relatively large uncertainties. Our early attempts to locate poles by spreading rate variation alone proved insufficient, so ridge azimuth at the centers of spreading segments was also added to the data set. Overall, it is possible to weight all of these elements

appropriately, and obtain a best-fit set of poles that describe motion on the major plate boundaries in the Lau Basin.

3.2 Main Plate Boundaries and their Associated Model Constraints

Fig. 3.2 shows the main plates, their boundaries, and all of the model constraints used as inputs to help determine Euler pole locations. Because the model constraints were chosen by closely studying the bathymetric, magnetization, and acoustic imagery maps simultaneously, sets of detailed maps of the three main boundaries are shown with their associated model constraints: A-T (Fig. 3.3 - 3.5), A-N (Fig. 3.6 - 3.8), and N-T (Fig. 3.9 - 3.11). The bounds of oceanic crust formed during the Brunhes Chron were picked carefully to avoid complex areas produced by features such as overlapping spreading centers. This method assumes that the pairs of points chosen along the Brunhes Chron magnetic lineation edge were at the same location along the ridge at 0.78 Ma. (Earlier tests allowed for iterations on the points chosen which were initially located by studying the conjugate off-axis ridge morphologies.) Azimuthal data derived from focal mechanisms, ridge axes and transform faults are plotted in Fig. 3.2 - 3.11. Details regarding the data from all the model constraints as well as GPS data describing the motion relative to Australia of the three locations on the Tonga Plate as reported by Bevis et al., (1997) are included in Tables 3.1 - 3.7 (located in the appendix).

3.3 Description of Method

The overall procedure in the kinematic modeling is carried out in two steps. First, a grid search is conducted to find the poles of opening that best fit the geophysically observed model constraints for each of the three plate

Fig. 3.2. Model constraints used to locate Euler poles. Ridge azimuths, T-axes and slip vectors are plotted (↗). Gray areas are regions of positively magnetized crust. Brunhes/Matuyama boundary pairs of picks are plotted (⊢ ⊣). In addition, geodetic vectors describing A-T relative plate motion (in mm/yr) are plotted as green arrows. The green box indicates the location for A-T plots in Fig. 3.2-3.4. The red box indicates the location for the A-N plots in Fig. 3.5-3.7. The blue box indicates the location of the N-T plots in Fig. 3.8-3.10. Model constraints are similarly assigned these colors according to their respective plate pair. Refer to Fig. 1.2 for a list of plate boundary names.

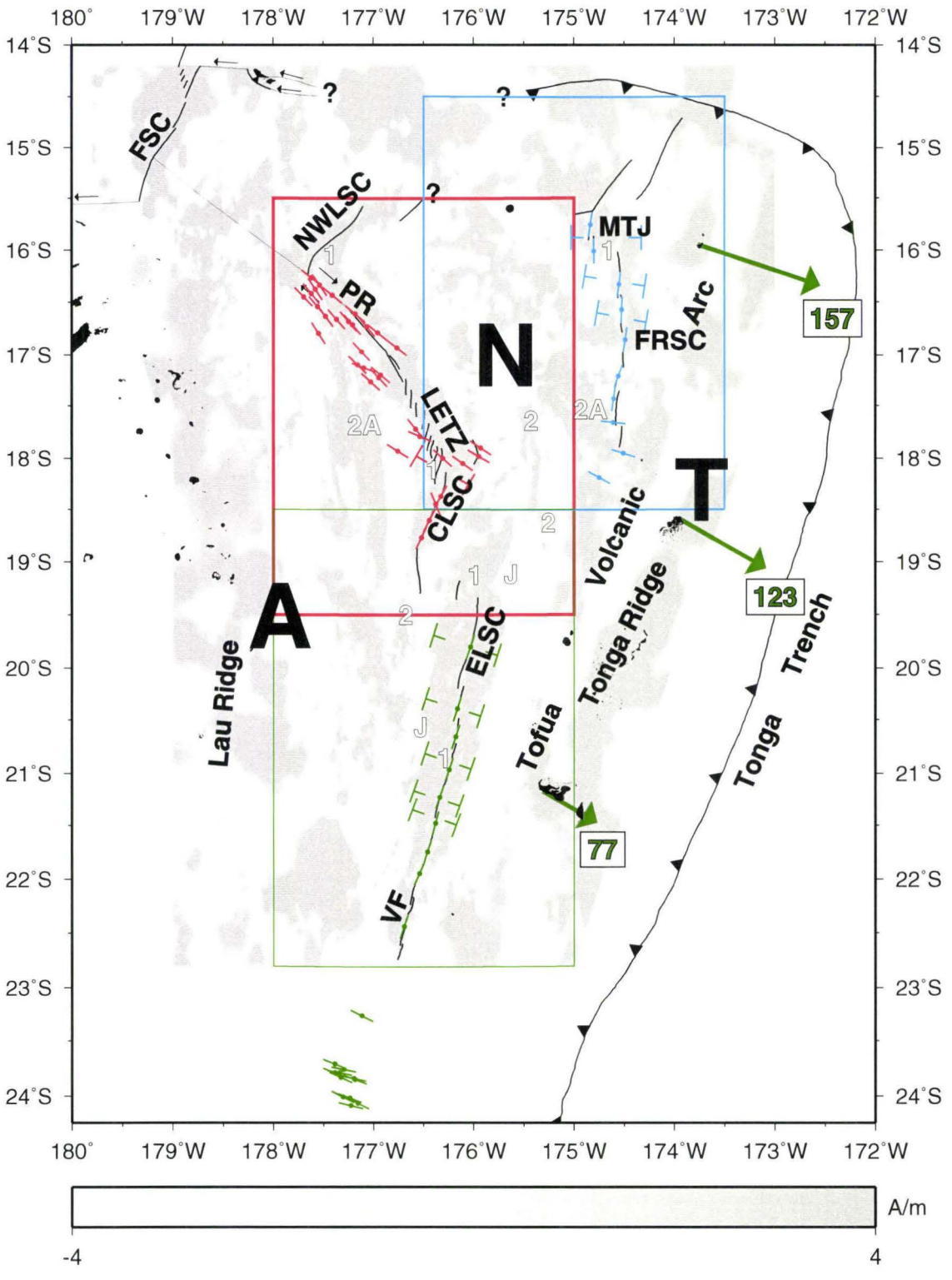
180°
179°W
178°W
177°W
176°W
175°W
174°W
173°W
172°W
14°S
15°S
16°S
17°S
18°S
19°S
20°S
21°S
22°S
23°S
24°S
FSC
NWLSC
PR
LETZ
CLSC
ELSC
VF
MTJ
FRSC
Arc
Volcanic
Tonga Ridge
Tofua
Tonga
Trench
Lau Ridge
N
A
T
157
123
77
A/m
-4
4

Fig. 3.3. Bathymetric map of the A-T boundary and its associated model constraints (refer also to Fig. 3.2). All available seismic data is plotted (refer to Fig. 1.11 for seismic symbol definitions). T-Axes south of the ELSC (shown in Fig. 3.2) are not included in this plot. Ridge azimuths were chosen on sections of the ELSC that were far from overlapping spreading centers.

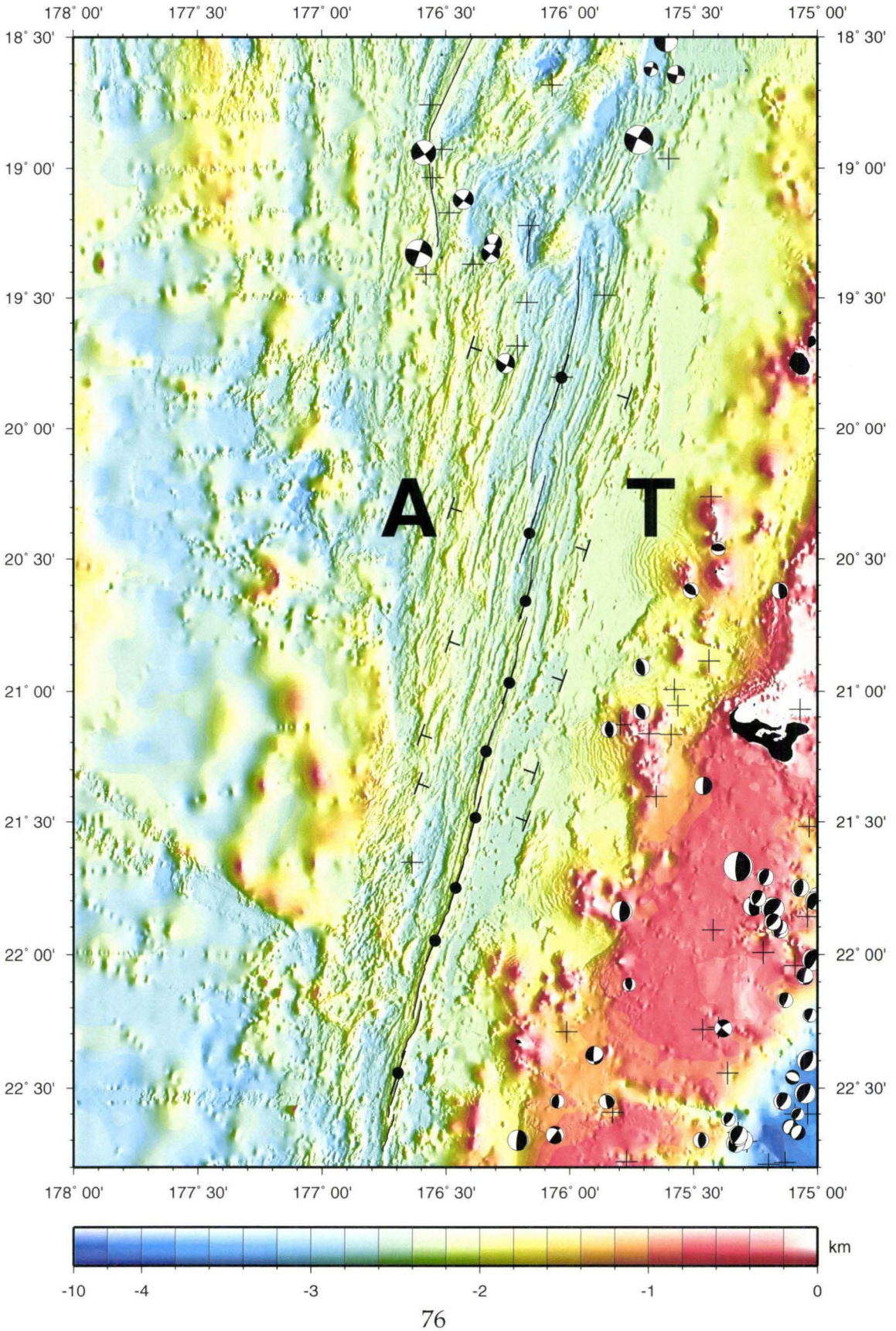
178° 00'
177° 30'
177° 00'
176° 30'
176° 00'
175° 30'
175° 00'
18° 30'
19° 00'
19° 30'
20° 00'
20° 30'
21° 00'
21° 30'
22° 00'
22° 30'
A
T
km
-10
-4
-3
-2
-1
0

Fig. 3.4. Magnetization map of the A-T boundary and positions of associated model constraints (refer also to Fig. 3.2). Positively magnetized crust is plotted in red; negatively magnetized crust is plotted in blue. The map is additionally highlighted with crustal fabric ("sunlit" from the east). All available seismic data is plotted (refer to Fig. 1.11 for seismic symbol definitions). T-Axes south of the ELSC (shown in Fig. 3.2) are not included in this plot. Pairs of Brunhes/Matuyama picks were carefully chosen in areas with clean boundaries and symmetric tectonic fabric.

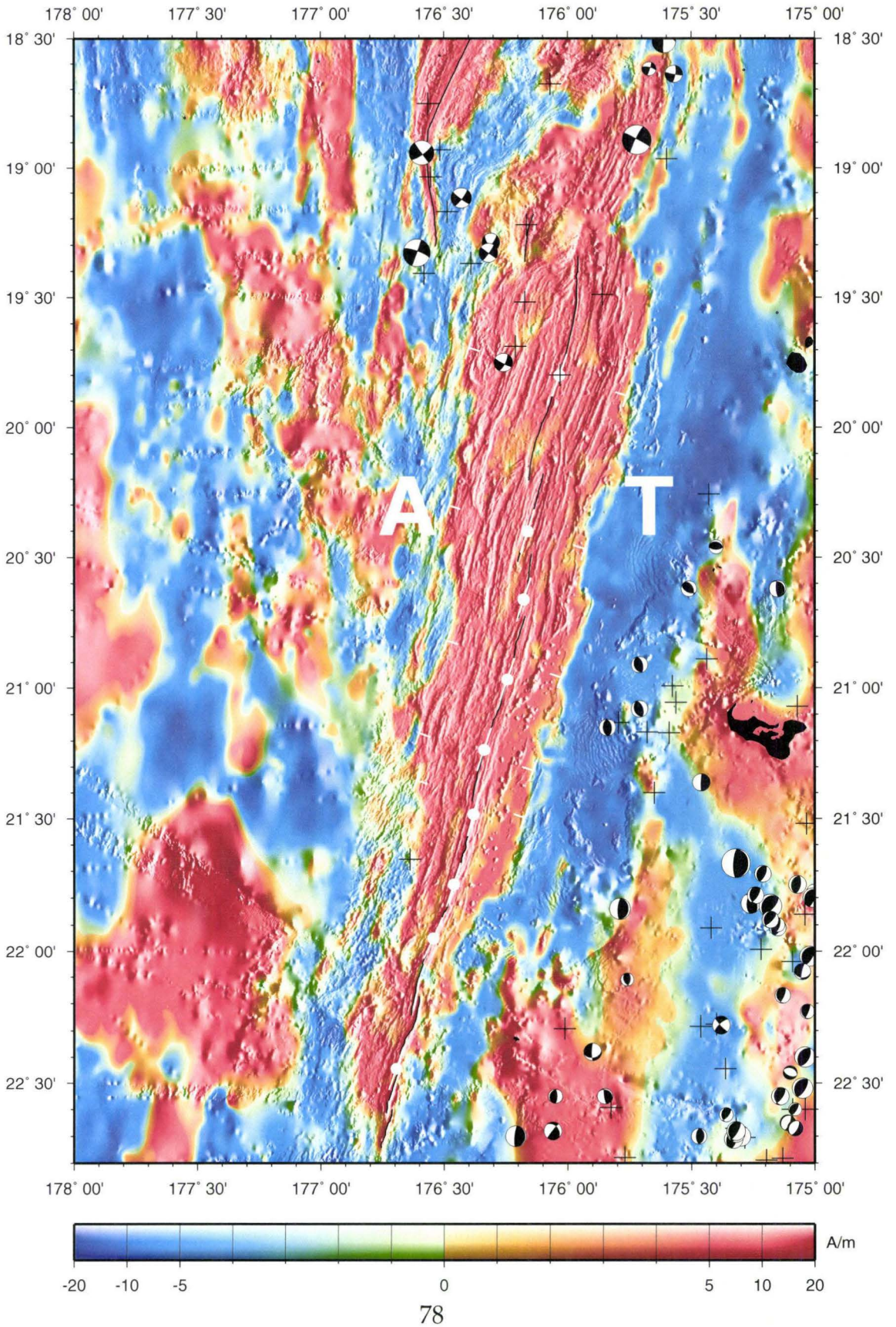
178° 00'
177° 30'
177° 00'
176° 30'
176° 00'
175° 30'
175° 00'
18° 30'
19° 00'
19° 30'
20° 00'
20° 30'
21° 00'
21° 30'
22° 00'
22° 30'
A
T
A/m
-20
-10
-5
0
5
10
20

Fig. 3.5. Acoustic reflectivity map of the A-T boundary and its associated model constraints (refer also to Fig. 3.2). The reflectivity scale (Ref) has been normalized between 0 (white, low reflectivity) and 1 (black, high reflectivity). All available seismic data is plotted (refer to Fig. 1.11 for seismic symbol definitions). T-Axes south of the ELSC (shown in Fig. 3.2) are not included in this plot. The ELSC plate boundaries are characterized by high reflectivity (black on image).

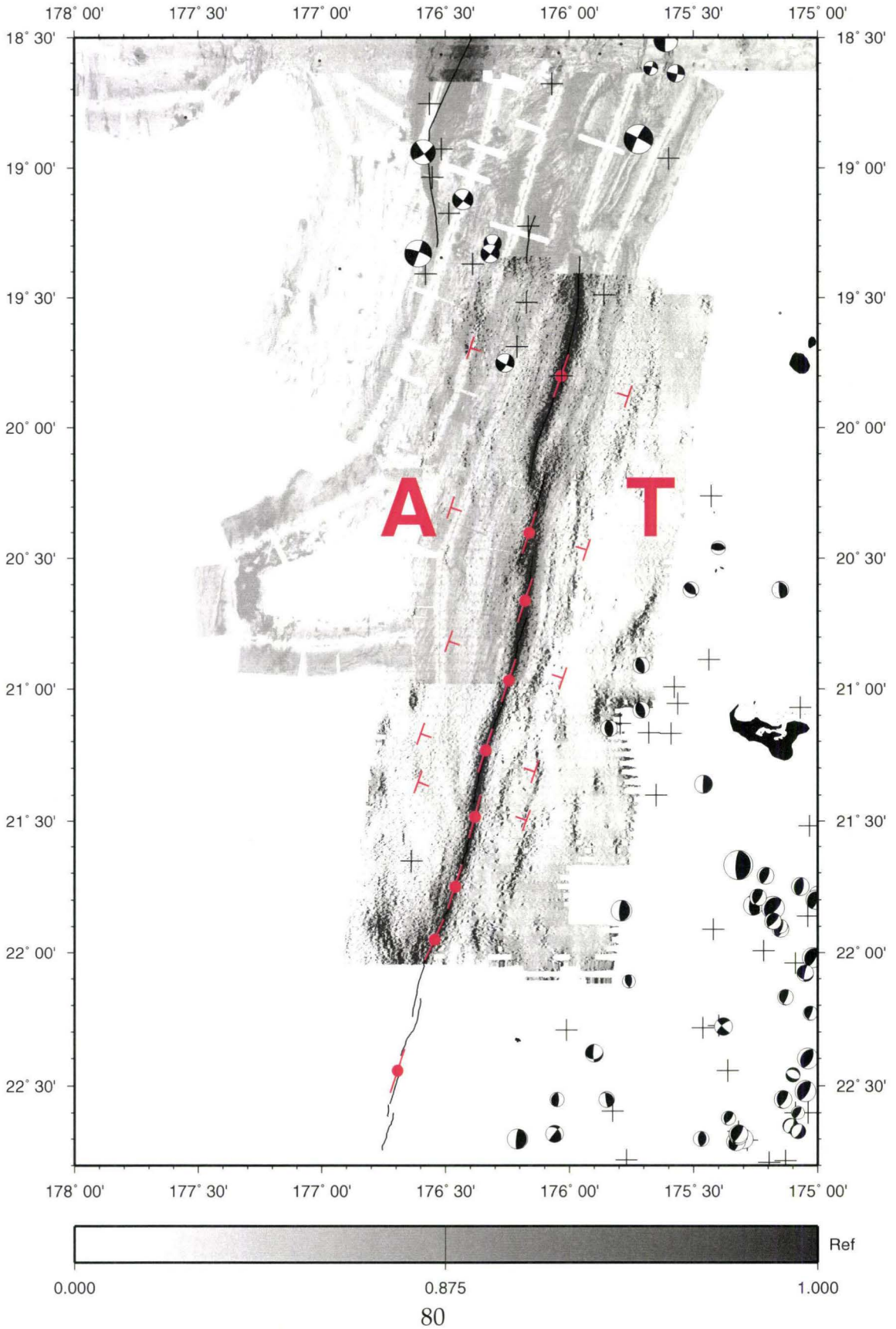
178° 00'
177° 30'
177° 00'
176° 30'
176° 00'
175° 30'
175° 00'
18° 30'
19° 00'
19° 30'
20° 00'
20° 30'
21° 00'
21° 30'
22° 00'
22° 30'
A
T
Ref
0.000
0.875
1.000

Fig 3.6. Bathymetric map of the A-N boundary and its associated model constraints (refer also to Fig. 3.2). All available seismic data is plotted (refer to Fig. 1.11 for seismic symbol definitions). Ridge azimuths were chosen along the CLSC in areas unaffected by the LETZ and the overlapping spreading center with the ELSC. Transform fault azimuths were picked on the active part of PR.

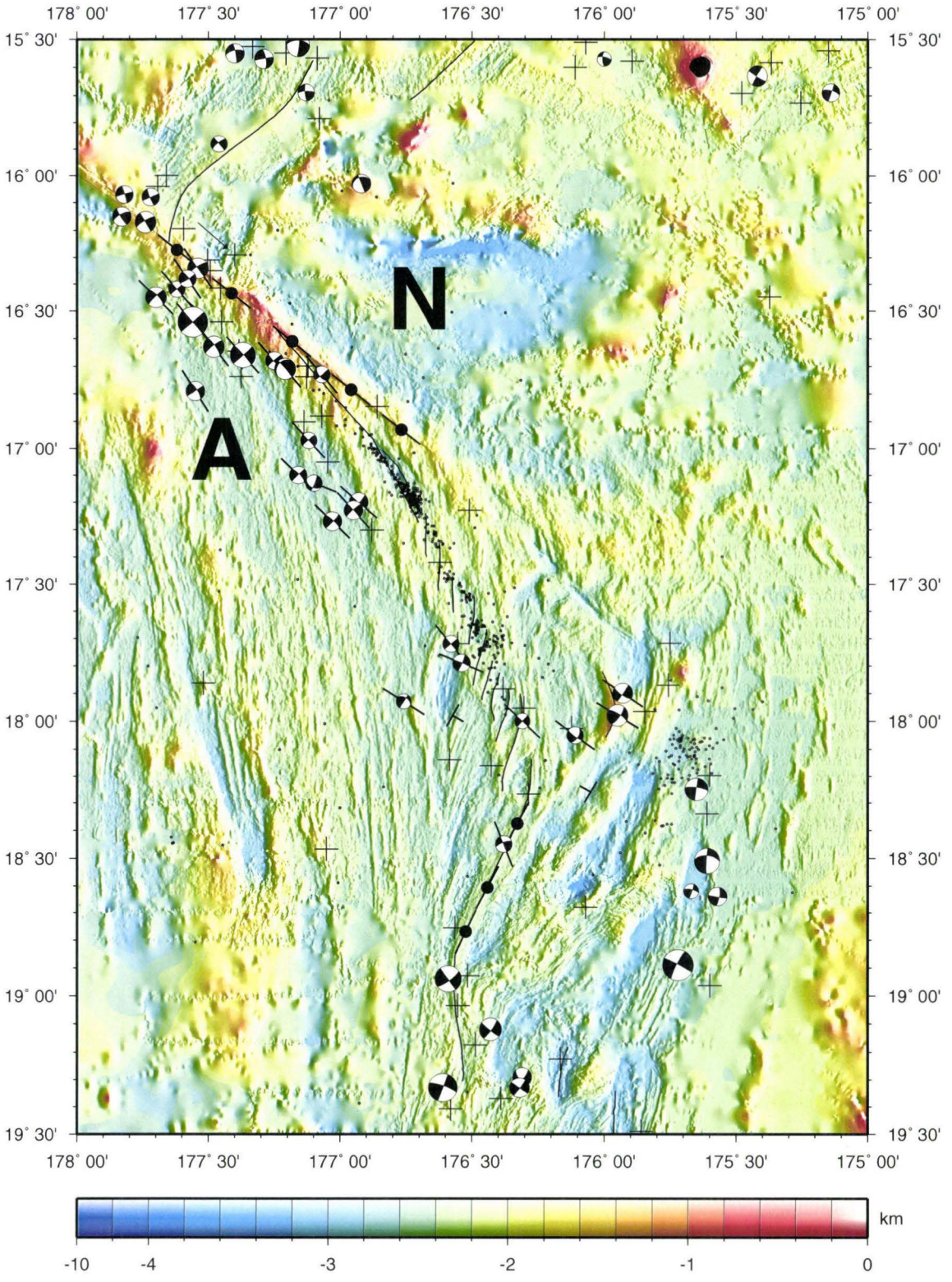
178° 00'
177° 30'
177° 00'
176° 30'
176° 00'
175° 30'
175° 00'
15° 30'
16° 00'
16° 30'
17° 00'
17° 30'
18° 00'
18° 30'
19° 00'
19° 30'
N
A
km
-10
-4
-3
-2
-1
0

Fig. 3.7. Magnetization map of the A-N boundary and its associated model constraints (refer also to Fig. 3.2). Positively magnetized crust is plotted in red; negatively magnetized crust is plotted in blue. The map is additionally highlighted with crustal fabric ("sunlit" from the east). All available seismic data is plotted (refer to Fig. 1.11 for seismic symbol definitions). In this region, only one pair of Brunhes/Matuyama picks could be made. We interpret the magnetic boundary just south of the pick is a propagation boundary.

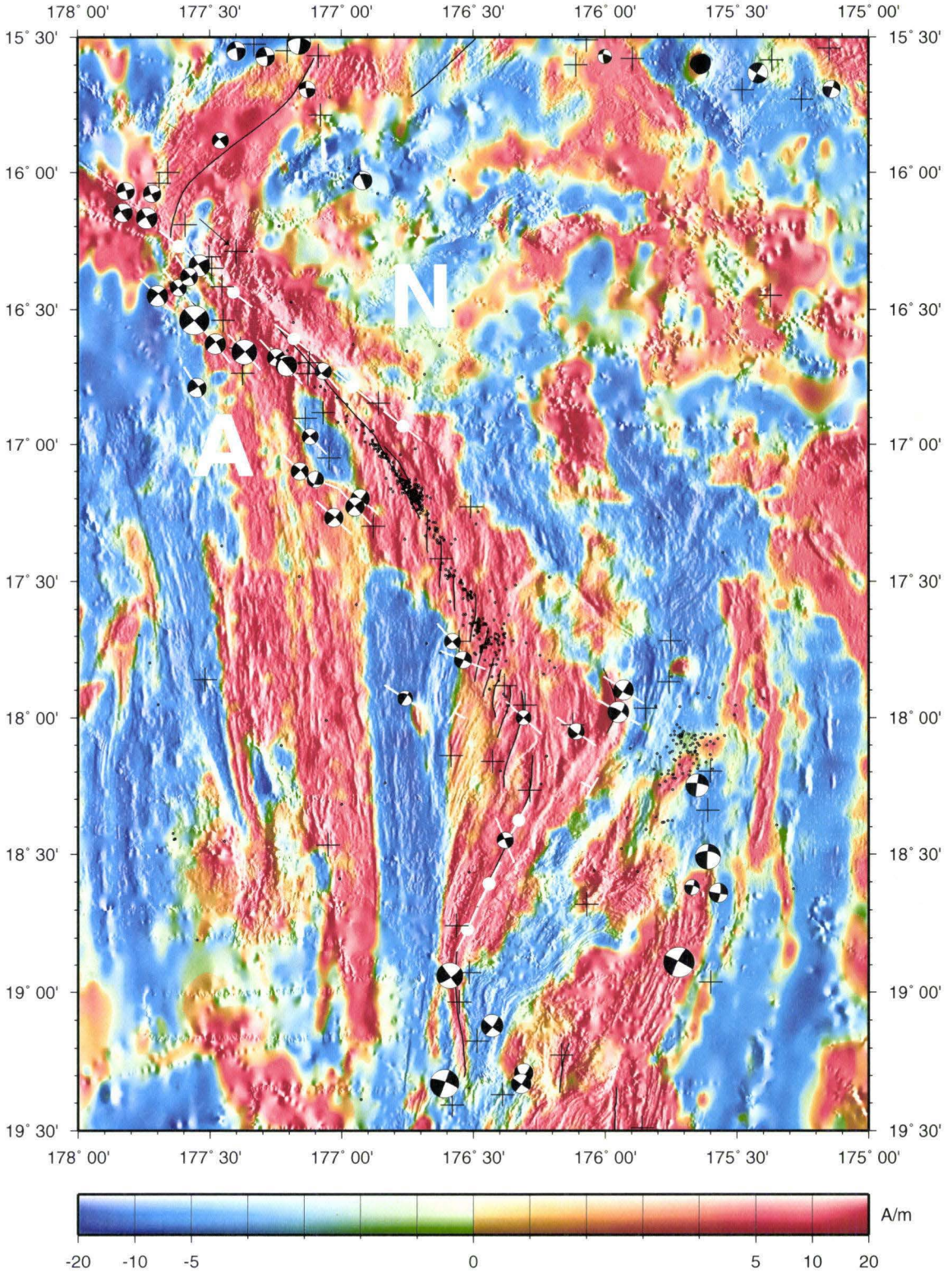
178° 00'
177° 30'
177° 00'
176° 30'
176° 00'
175° 30'
175° 00'
15° 30'
16° 00'
16° 30'
17° 00'
17° 30'
18° 00'
18° 30'
19° 00'
19° 30'
N
A
A/m
-20
-10
-5
0
5
10
20

Fig. 3.8. Acoustic reflectivity map of the A-N boundary and its associated model constraints (refer also to Fig. 3.2). The reflectivity scale (Ref) has been normalized between 0 (white, low reflectivity) and 1 (black, high reflectivity). All available seismic data is plotted (refer to Fig. 1.11 for seismic symbol definitions). The most prominent highly reflective features are the CLSC and the LETZ. The southern boundary of the N microplate shows no visible plate boundary in the acoustic reflectivity, however there is a band of seismicity in this region.

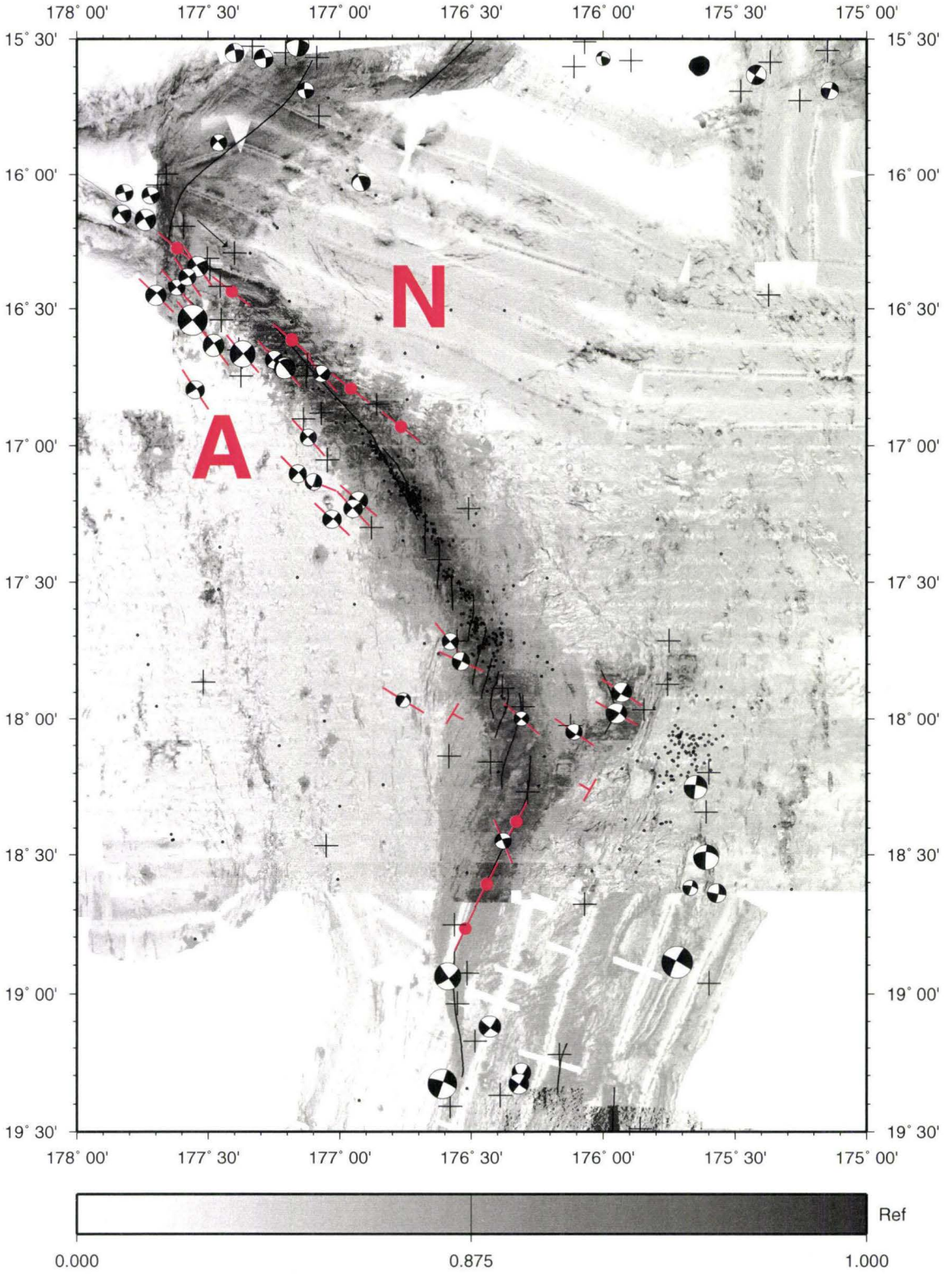
178° 00'
177° 30'
177° 00'
176° 30'
176° 00'
175° 30'
175° 00'
15° 30'
16° 00'
16° 30'
17° 00'
17° 30'
18° 00'
18° 30'
19° 00'
19° 30'
N
A
Ref
0.000
0.875
1.000

Fig. 3.9. Bathymetric map of the N-T boundary and its associated model constraints (refer also to Fig. 3.2). All available seismic data is plotted (refer to Fig. 1.11 for seismic symbol definitions). Ridge azimuths were chosen along the southern limb of the MTJ and the FRSC away from overlapping spreading centers.

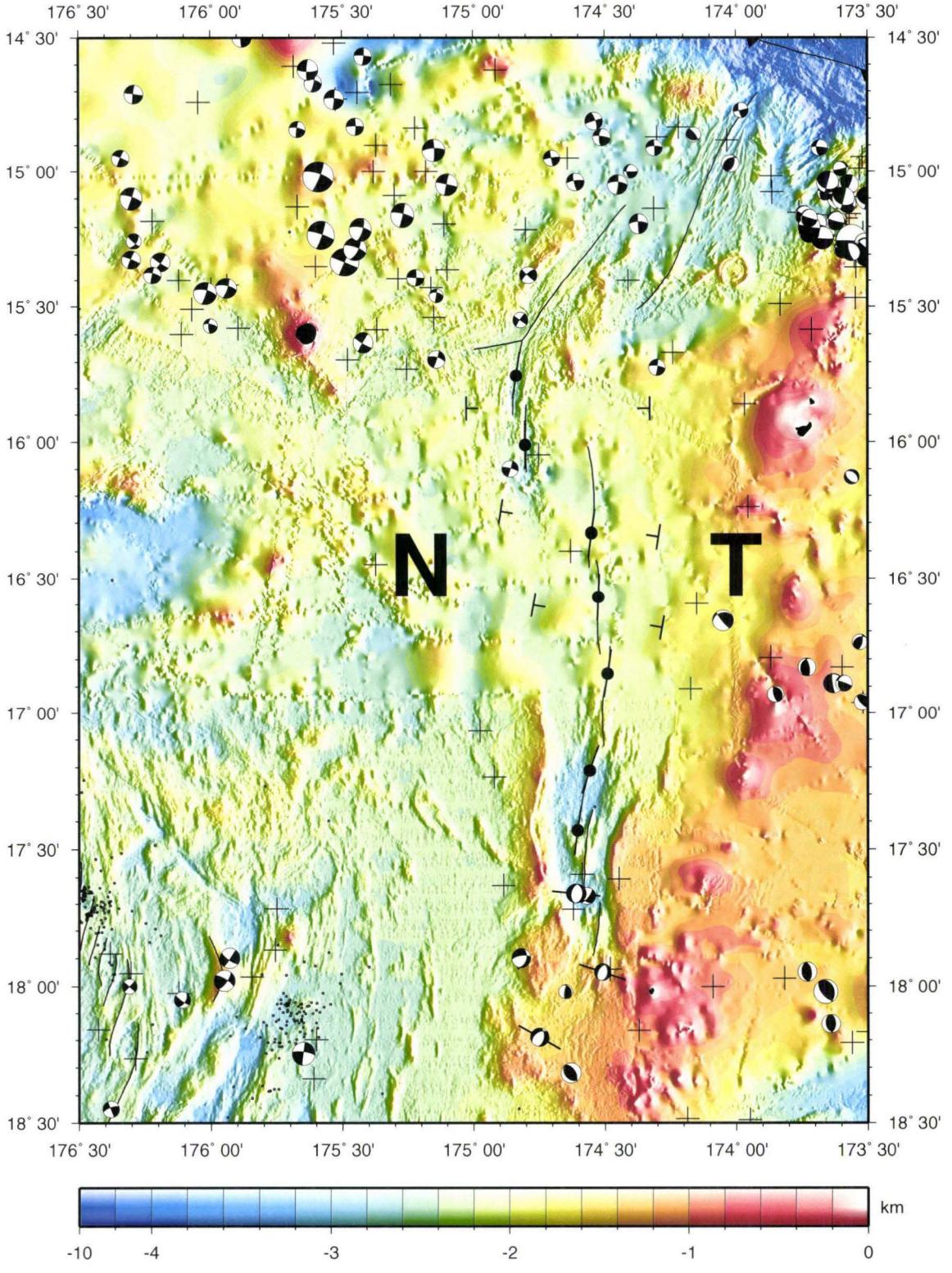
176° 30'
176° 00'
175° 30'
175° 00'
174° 30'
174° 00'
173° 30'
14° 30'
15° 00'
15° 30'
16° 00'
16° 30'
17° 00'
17° 30'
18° 00'
18° 30'
N
T
km
-10
-4
-3
-2
-1
0

Fig. 3.10 Magnetization map of the N-T boundary and its associated model constraints (refer also to Fig. 3.2). Positively magnetized crust is plotted in red; negatively magnetized crust is plotted in blue. The map is additionally highlighted with crustal fabric ("sunlit" from the east). All available seismic data is plotted (refer to Fig. 1.11 for seismic symbol definitions). Despite weakness in the magnetization field near 16° 15'S, three pairs of Brunhes/Matuyama picks were made.

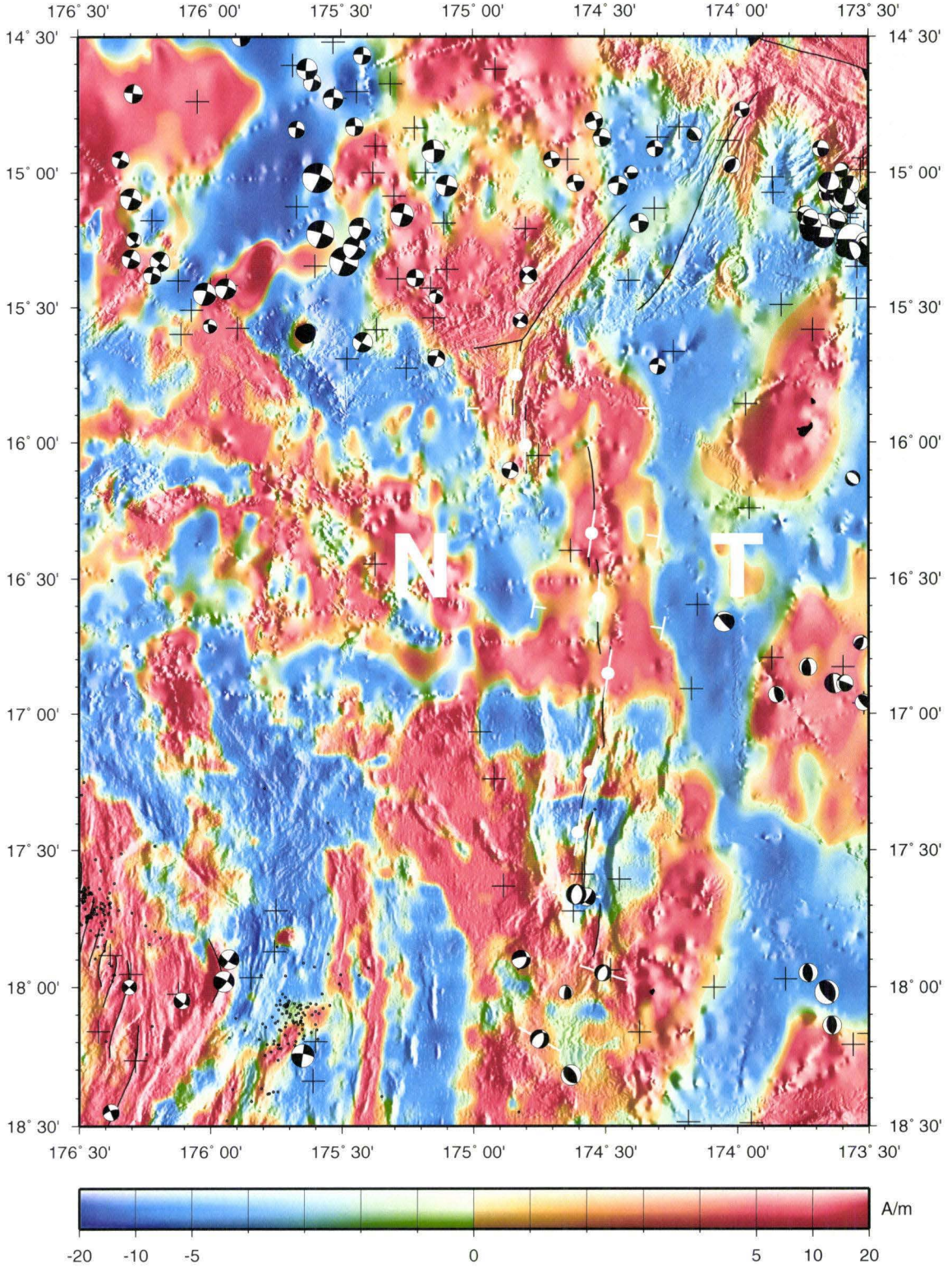
176° 30'
176° 00'
175° 30'
175° 00'
174° 30'
174° 00'
173° 30'
14° 30'
15° 00'
15° 30'
16° 00'
16° 30'
17° 00'
17° 30'
18° 00'
18° 30'
N
T
A/m
-20
-10
-5
0
5
10
20

Fig. 3.11. Acoustic reflectivity map of the N-T boundary and its associated model constraints (refer also to Fig. 3.2). The reflectivity scale (Ref) has been normalized between 0 (white, low reflectivity) and 1 (black, high reflectivity). All available seismic data is plotted (refer to Fig. 1.11 for seismic symbol definitions). Both the MTJ and the FRSC are highly reflective.

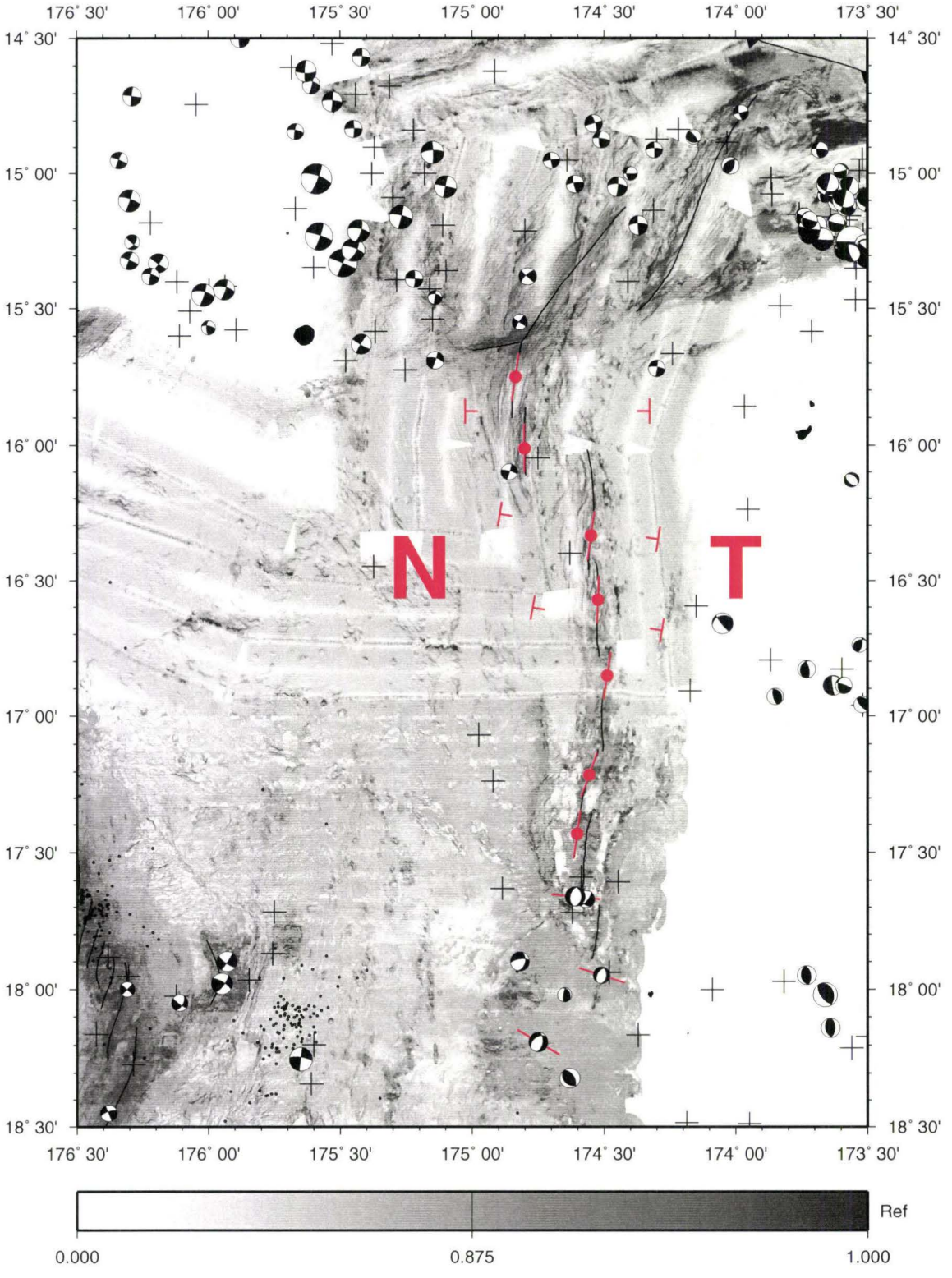
176° 30'
176° 00'
175° 30'
175° 00'
174° 30'
174° 00'
173° 30'
14° 30'
15° 00'
15° 30'
16° 00'
16° 30'
17° 00'
17° 30'
18° 00'
18° 30'
N
T
Ref
0.000
0.875
1.000

boundaries. At this stage, the three resultant Euler poles are referred to as "two-plate solutions" because they have *not yet* met the three-plate closure criteria of Eqn. (1). A "three-plate solution" is a single set of three poles that simultaneously best-fits all of the model constraints along all three boundaries while *also* meeting vector addition criteria. The two-plate pole solutions statistically best fit their model constraints along their respective boundaries, but in this procedure are only used as a means to assess the ability of the final "three-plate solutions" to match their respective model constraints while *additionally* adhering to the plate closure criteria. In order to find the three-plate pole solutions, we first use a bootstrap method to generate error ellipsoids about each of the three previously calculated "two-plate" poles. The three error regions that result from the bootstrap analysis are simultaneously searched to find the final "three-plate solution" that fully describes the kinematics.

3.3.1 Initial Calculations

The code locates best-fit poles of opening with a basic grid-search method. Tests are first conducted on a broad scale to find appropriate regions for the three grids to be located. A coarse grid of 0.5° is constructed for each of the three search-areas, and for each grid node (i.e., for each trial pole) a series of calculations are made (square brackets [] refer to a set of values):

(1) [delta] = angular distance from the trial pole location. For the pairs of locations bounding crust formed during the Brunhes Chron, angular distances to both edges are calculated and averaged. It is assumed that the true pole location should yield nearly identical delta values for either point, therefore the averaged value is acceptable for use. For the geodetic data, delta

represents simply the angular distance between the trial pole location and the GPS station position.

(2) [ωs] = a set of angular velocities for each pair of Brunhes Chron boundaries or geodetic vector. For the magnetic picks, both points in the pair are projected relative to the trial pole location and the angular difference between them is calculated and converted to an angular velocity. For the instantaneous geodetic data, values of ωs are determined directly from their recorded relative velocity and delta value.

(3) ωo = a single median value of all ωs calculations for each trial pole. The value of ωo is used *only* as an initial guess for the trial pole's associated angular velocity and is discussed in further detail in section 3.3.2.

(4) [spreading rate] = either (a) the distance between each pair of points as measured along a small circle subtended about the trial pole location at an angular distance of delta divided by the Brunhes anomaly duration (0.78 Ma), or (b) the instantaneous relative velocity calculated directly from the geodetic measurements.

To facilitate iterations on the pole location search, a second higher resolution 0.1° rectangular grid (2° north-south by 1° east-west) centered about each coarse grid node is also constructed, and all of the previously discussed calculations are repeated for each of these grids. Early tests indicated that when refining the pole location using the methods of 3.3.2, the pole was more likely to migrate north-south rather than east-west; this is why the rectangular 0.1° grid is used to search areas are elongated to the north and the south.

3.3.2 Finding Best-Fit Pole Solutions for Individual Two-Plate Systems

The general method for finding the pole location for any given two-plate system involves an initial latitude-longitude grid search at 0.5°, then a refinement at 0.1°. The angular rate of opening, ω, is assigned an initial value of ωo and is simultaneously refined to a resolution of 0.1°/Ma utilizing the high resolution grids discussed in section 3.3.1. Statistics assigned to each tested grid node are based on two main categories: (1) spreading rate observations along the respective boundary, and (2) observed azimuthal values, α, as compared to great circles radiating from the pole location. The value of ωo is used as an initial "guess" for the angular rate of the pole, and is varied by ±1 °/Ma in 0.1°/Ma increments. Predicted values of spreading rate are expected to vary as a function of angular rate and delta. Observed azimuthal values along the respective boundary are compared to the radial great circles that extend from the trial pole.

Best-fit statistics are generated assuming that errors in spreading rate and azimuth are equal in importance, i.e., a 1 mm/yr deviation in spreading rate is weighted the same as a 1° azimuthal deviation from a great circle relative to the trial pole. Statistics are based on a weighted least-squares method:

$$\text{stat (rate or azimuth)} = \frac{[\text{weight}]*[\text{expected value-observed value}]^2}{\Sigma(\text{weights})}, \qquad (2)$$

and the rate and azimuth statistics for each grid node and trial ω values are averaged. A weighting scheme was introduced to underweight less reliable data. Weights for each of the model constraints are listed Tables 3.1 - 3.7 located in the appendix. Weights are normalized to 1.0. The values of the T-axes and slip vectors are known to vary by up to 10°, therefore have been assigned a weight of 0.1. The two-plate solution for a given boundary is determined by the latitude-longitude grid node (and associated ω value) that carries the lowest statistic.

3.3.3 Error Analysis via the Bootstrap Method

Several methods have been proposed and analyzed for carrying out error analysis of data subtended about poles of opening (Wilson, 1993). The method used in this procedure is based on bootstrap resampling (Efron and Tibshirani, 1986), in which data inputs are randomly resampled such that some data values are selected multiple times while others are left out. Using this "resampled" set of inputs, calculations are then completed exactly as described in section 3.3.2. This method generates a scatter of points about the three two-plate pole solutions, and are thought to be a reasonable indication of error inherent within the data.

To generate contours of confidence limits about the best-fitting pole, a density function described by Wilson (1993) is utilized. In this method, a density value, d, is assigned to each pole that emerges from the bootstrap resampling. The value of d is near unity when solutions are clustered tightly, whereas the value of d drops to values near zero for outlier solutions. Bootstrap pole solutions are converted to Cartesian coordinates, normalized, and both the mean and covariance matrix about the mean are calculated for

the normalized poles. Eigenvectors and eigenvalues of the covariance matrix correspond to the orientations of the principal axes and the variance about these axes respectively. Here the principal axes refer to variations in latitude, longitude, and ω about the two-plate pole solution. Bootstrap pole solutions are projected on to these axes and tested for their proximity to other solutions in the data set. To contour the 95% confidence region, density values are gridded, filtered, and sorted, and the value above which 95% of the other solutions lies becomes the "threshold value" for the 95% confidence contour. Because a pole of opening has three parameters associated with it (latitude, longitude, and ω), the threshold value applies to all values simultaneously.

3.3.4 Finding Best-Fit Pole Solutions for the Three-Plate System

The final set of three-plate pole solutions must sum to zero as well as statistically matching the model constraints on all of the boundaries. To find this final set Euler poles, the three confidence regions generated using the bootstrap method of section 3.3.3 are used to generate a new set of trial poles. Since any two poles determine the third (Eqn. 1), three "clouds" of predicted poles are generated using all possible pairs of poles within the system. These "clouds" of predicted poles are reduced, gridded, and assigned density values and contoured at the 100% confidence level. Solid overlap zones between the two-plate pole clouds and the predicted pole clouds are determined to give three final subsets of trial poles for use with the three-plate solution method. This method is used to constrain the number of points in the final search.

To determine the best-fit three-plate solution, the two smallest of the three final subsets are used to predict the third pole using the Euler vector summation constraints. If the third pole falls within the pre-determined

"acceptable" overlap region, it is kept as a possible three-plate solution. Each of these possible three-plate solutions also has a single least-squares statistic associated with it as in equation (1) except all statistics for all three of the individual two-plate solutions are stored before dividing by the total sum of weights. This method assures that all of the model constraints on all three of the boundaries are considered simultaneously. As for the two-plate solution, the set of poles that carries the lowest statistic is assigned to be the final three-plate kinematic solution for the entire system.

CHAPTER 4. RESULTS AND DISCUSSION

4.1 Introduction

4.1.1 Why a Three-Plate model?

The original focus of the kinematic model was simply to find the location of the A-T pole. Working under the early hypothesis that the ELSC and the CLSC/LETZ/PR plate boundaries were *both* separating Australia and Tonga, all of the model constraints described in chapter 3 for these two boundaries were initially included as one single input data set and an A-T pole was determined. This calculation revealed that the model constraints (i.e., spreading rate data, ridge azimuths, transform fault azimuths, and slip vectors) observed along the CLSC/LETZ/PR system did not fit well with a pole derived from the data for the ELSC system (Fig. 4.1). This discovery was fundamental because the result implied that motions across the ELSC and the CLSC/LETZ/PR were not co-polar. In other words, a system of more than two plates was necessary to adequately model the kinematics of the Lau Basin. This observation prompted the three-plate model illustrated in Fig. 1.13. Motions across the recently recognized FRSC plate boundary had previously not been considered in a whole-basin kinematic analysis. In addition, the revised geodetic vectors reported by Bevis (1997) revealed that the northern region of Tonga (north of ~18°S) was moving in a different direction than southern Tonga. As stated in Chapter 1, the Niuafo'ou microplate was proposed as an intervening plate wedged between the Australian and Tongan plates, and it was hypothesized that motion at the edges of this microplate could explain these observations. The proposed Niuafo'ou microplate lacks a classical narrow, identifiable southern boundary. Despite this obvious

Fig. 4.1. Model constraints: (a) spreading rates and (b) azimuths along the ELSC (green open circles) are incompatible with those near the PR/CLSC/LETZ (red open circles) system when used together to predict an A-T pole of opening. Weighted observed values=large open circles; underweighted observed values=small open circles; predicted values=solid line or closed circles. This figure shows that the motions across these two boundaries are not co-polar.

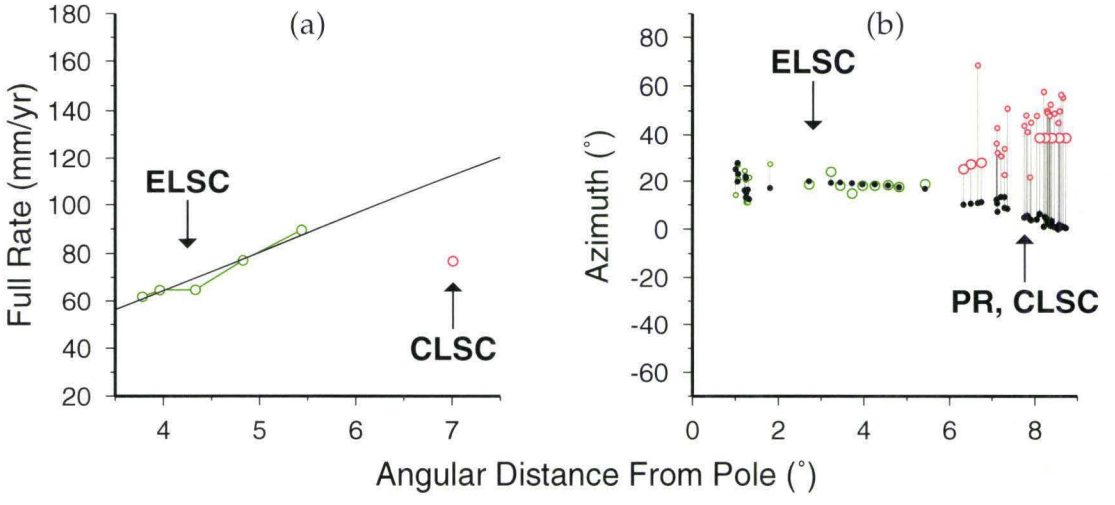
(a)
(b)
ELSC
CLSC
ELSC
PR, CLSC
Full Rate (mm/yr)
Azimuth (°)
Angular Distance From Pole (°)
180
160
140
120
100
80
60
40
20
80
60
40
20
0
-20
-40
-60
4
5
6
7
0
2
4
6
8

problem, it was further hypothesized that the motion of the Niuafo'ou microplate was disparate enough from the Australian and Tongan plates to be kinematically modeled using constraints at the boundaries that could be mapped.

4.1.2 Description of Calculations

Here we present the results of two main calculation "runs" for the proposed three-plate system. The first is based on model constraints derived from focal mechanisms, spreading rates determined from marine magnetic data and ridge azimuths *only* and the second additionally includes the geodetic vectors of by Bevis (1997). The purpose of the first run is to calculate Euler poles based *solely* on non-geodetic data to independently assess the compatibility of the geodetic vectors with the other geophysical observations throughout the Lau Basin. As will be shown, a three-plate system is modeled that is consistent with the geodetic data.

4.2 First Run: Marine and Seismicity Data Inputs Independent of Geodetic Data

4.2.1 Two-Plate Solutions and Their 95% Confidence Regions

As described in Chapter 3, the first stage of the calculation involves finding "two-plate" poles of opening that best fit model constraints associated with their respective boundary. Table 4.1 lists these best-fit two-plate poles according to their plate system and boundaries, and their locations are plotted as solid stars in Fig. 4.2 and Fig. 4.3.

Fig. 4.2. Euler poles and the two-plate 95% confidence regions (longitude-latitude space) for the first run. Solid stars show the locations of the two-plate pole solutions; open stars show the locations of the three-plate pole solutions. The A-T boundary is plotted in green; A-N boundary is plotted in red; N-T boundary is plotted in blue. Both the A-T and the N-T pole are tightly constrained spatially, whereas the A-N pole is not.

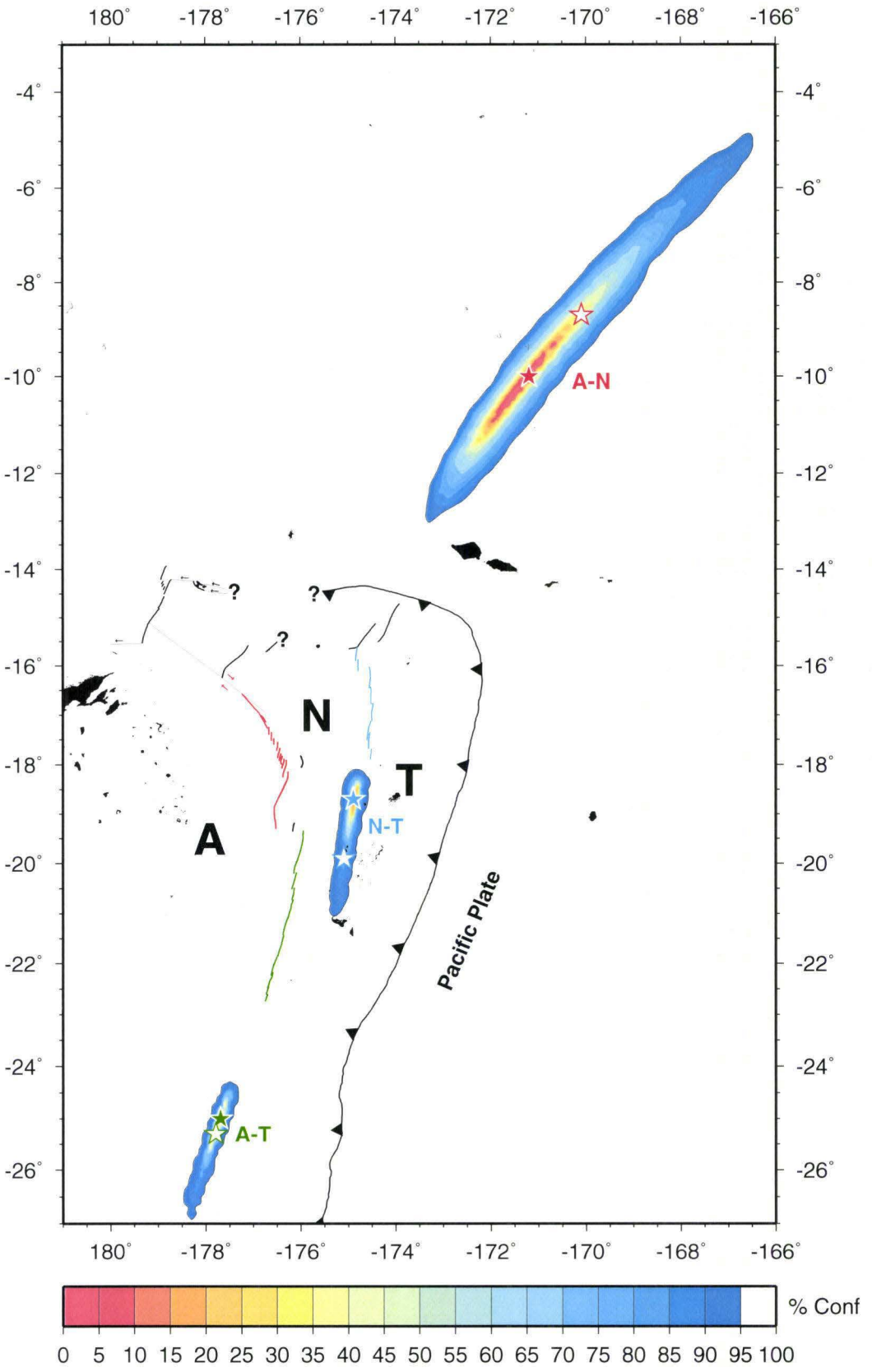
180°
-178°
-176°
-174°
-172°
-170°
-168°
-166°
-4°
-6°
-8°
-10°
-12°
-14°
-16°
-18°
-20°
-22°
-24°
-26°
A-N
N
T
A
N-T
Pacific Plate
A-T
% Conf
0 5 10 15 20 25 30 35 40 45 50 55 60 65 70 75 80 85 90 95 100

Fig. 4.3. Euler poles and the two-plate 95% confidence regions (ω-latitude space) for the first run. Solid stars show the locations of the two-plate pole solutions; open stars show the locations of the three-plate pole solutions. The A-T pole is tightly constrained in ω. The N-T pole shows a wide range of possible omega values. Due to the close spatial proximity of the N-T pole to the FRSC and MTJ (refer to Fig. 4.2), a small change spatially requires a large change in ω.

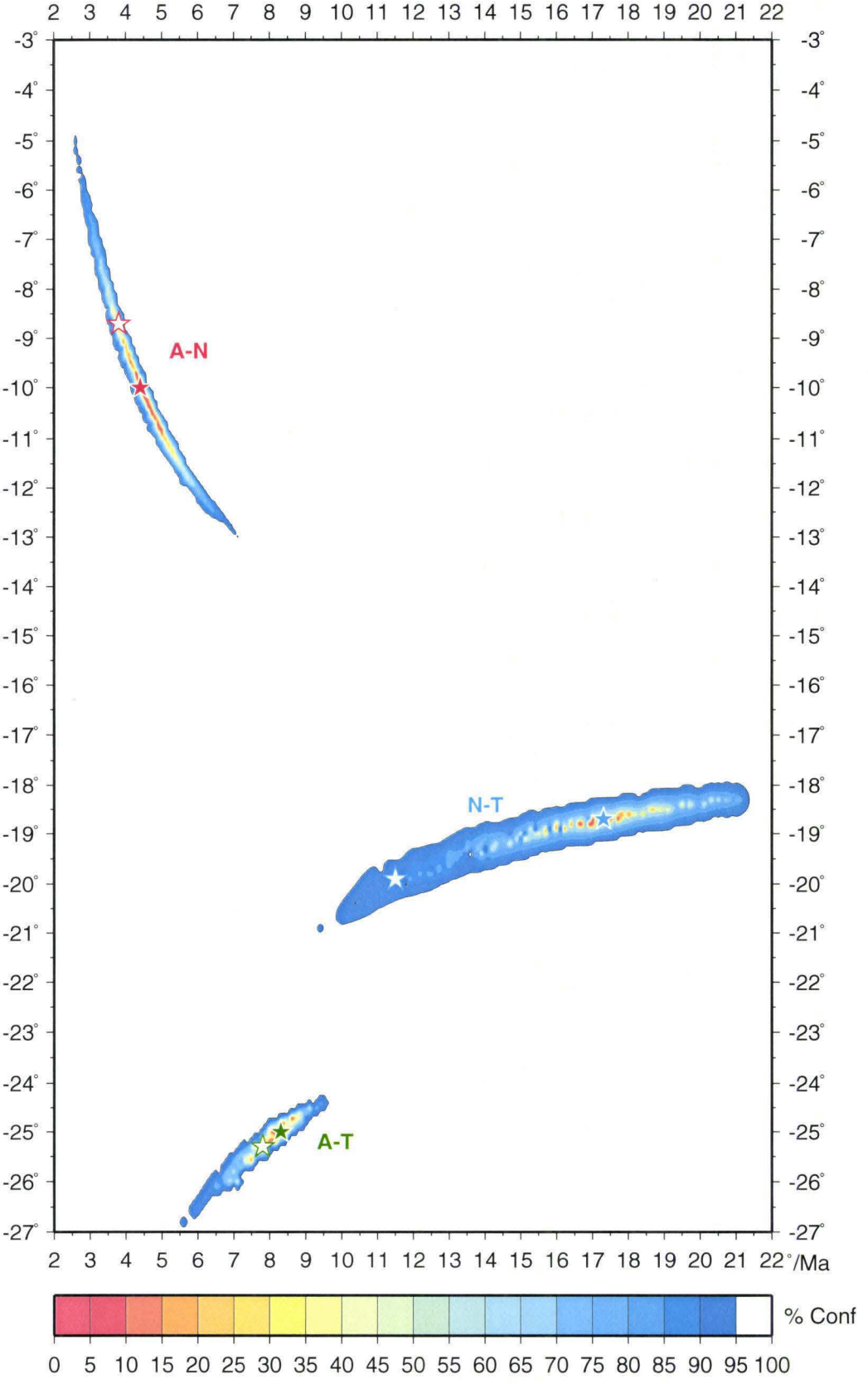
2 3 4 5 6 7 8 9 10 11 12 13 14 15 16 17 18 19 20 21 22
-3° -4° -5° -6° -7° -8° -9° -10° -11° -12° -13° -14° -15° -16° -17° -18° -19° -20° -21° -22° -23° -24° -25° -26° -27°
A-N
N-T
A-T
°/Ma
% Conf
0 5 10 15 20 25 30 35 40 45 50 55 60 65 70 75 80 85 90 95 100

Pole	Boundary	Long (°W)	Lat (°S)	ω (°/Ma)
A-T	ELSC	177.7	25.0	8.3
A-N	CLSC,PR	171.2	10.0	4.4
N-T	FRSC	174.9	18.7	17.3

Table 4.1 Best fit two-plate poles of opening for the marine and seismicity data.

Error analysis about these two-plate poles was conducted, and 95% confidence regions were determined for each of the poles using the bootstrap methods described in section 3.3.3. These regions are plotted in Fig. 4.2 and Fig. 4.3. Fig. 4.2 shows the error region in latitude-longitude space, and Fig. 4.3 shows the error region in longitude-ω space. The A-T pole has the smallest error region (in all three dimensions), in part due to the good coverage along the ELSC which resulted in a reliable set of marine magnetic Brunhes/Matuyama boundary picks. The A-N pole is the least well-constrained for two main reasons: (1) only one magnetic pick could be made on the CLSC. Just south of the single A-N magnetic anomaly pick, the magnetic boundary actually marks the edge of new crust propagating into old crust and thus is not a true 0.78 Ma boundary. (2) earthquake focal mechanisms, which make up a large portion of the inputs, are not well located. Although these inputs were underweighted, the resultant pole is less tightly constrained. The N-T pole is tightly bound spatially, but spans a wide range of possible ω-values. This is mainly due to the close proximity of the N-T pole to its plate boundary; i.e., a small change spatially results in a great change in angular rate.

4.2.2 Three-Plate Solution

A best-fitting three-plate solution was found using the methods described in chapter 3. This set of poles is plotted in Fig. 4.2 and Fig. 4.3 as open stars, and listed in Table 4.2.

Pole	Boundary	Long (°W)	Lat (°S)	ω (°/Ma)
A-T	ELSC	177.8	25.3	7.8
A-N	CLSC,PR	170.1	8.7	3.8
N-T	FRSC	175.1	19.9	11.5

Table 4.2 Best fit three-plate pole solution for the marine and seismicity input run.

The fact that a compatible set of three poles can be defined within the 95% confidence ellipsoids of the three two-plate poles is significant. It means that relative motions that meet the closure criteria of Eqn. (1) can be realized for the Tongan forearc Plate, the Niuafo'ou microplate, and the large Australian Plate system for periods ≥ 0.78 Ma.

As can be seen by comparing Table 4.1 to Table 4.2, the three-plate solution forces all of the rates to decrease from their respective two plate solutions because the poles all move farther away from their respective plate boundaries. An increase in the distance from the pole will always result in a decrease in ω. The A-T pole is least affected by the additional constraints applied to complete the plate circuit. The N-T pole drops dramatically in angular rate when compared to its two-plate solution, although some believe

that the 11.5 °/Ma is a more reasonable rate for plate motion when compared to typical rates worldwide (D. Wilson, personal communication, 1999).

4.2.3 Fit to Pole Solutions

Fig. 4.4 (a - f) shows the compatibility between the observed model constraints and the rates and azimuths calculated from the two-plate pole solutions of the first run. In all three two-plate cases, the observed velocity values all match their modeled values to within 2 mm/yr on average (Fig. 4.4 (a, c, e)). Weighted azimuthal observations generally deviate from their expected values by less than 5° whereas the less-trusted and therefore underweighted values tend to deviate by more than 10° (Fig. 4.4 (b, d, f)). Most notable is the consistent mismatch of the underweighted azimuthal values for the two-plate A-N pole (Fig. 4.4. (d)). The seismicity data in this area generally does not follow the same trend as is observed along the PR transform fault. The PR transform fault trace and the trend of the CLSC are considered to be the more reliable azimuthal data available for the kinematic inversion because their locations are well known. The slip vectors determined from focal mechanisms are poorly constrained and do not reflect any component of extension in regions near the LETZ where both types of motion are taking place simultaneously. The weighting value of 1.0 on the PR and the CLSC reflects this bias.

Fig. 4.5 (a - f) shows similar compatibility plots for the first run's three-plate solution. In a perfect theoretical case, the two- and three-plate solutions would be identical. This would imply that the three poles describing the tectonics in the region best-fit model constraints on their boundaries *and* met closure criteria. Because there is inherent error in our model, some

Fig. 4.4. Compatibility plots of spreading rate and azimuth data for the two-plate solutions of the first run. Predicted values are calculated from the two-plate pole solutions from the first run and are colored according to their respective pole as follows: A-T pole=green; A-N pole=red; N-T pole=blue. Weighted observed values=large open circles; underweighted observed values=small open circles; predicted values=solid black line or closed black circles. (a) Fit of spreading rate to the two-plate A-T pole. (b) Fit of azimuthal model constraints to the two-plate A-T pole. (c) Fit of spreading rate to the two-plate A-N pole. (d) Fit of azimuthal model constraints to the two-plate A-N pole. (e) Fit of spreading rate to the two-plate N-T pole. (f) Fit of azimuthal model constraints to the two-plate N-T pole. The two-plate solutions are expected to give the best statistical fit possible to their respective model constraints because no compromise has been made to meet three-plate closure criteria at this step in the modeling procedure.

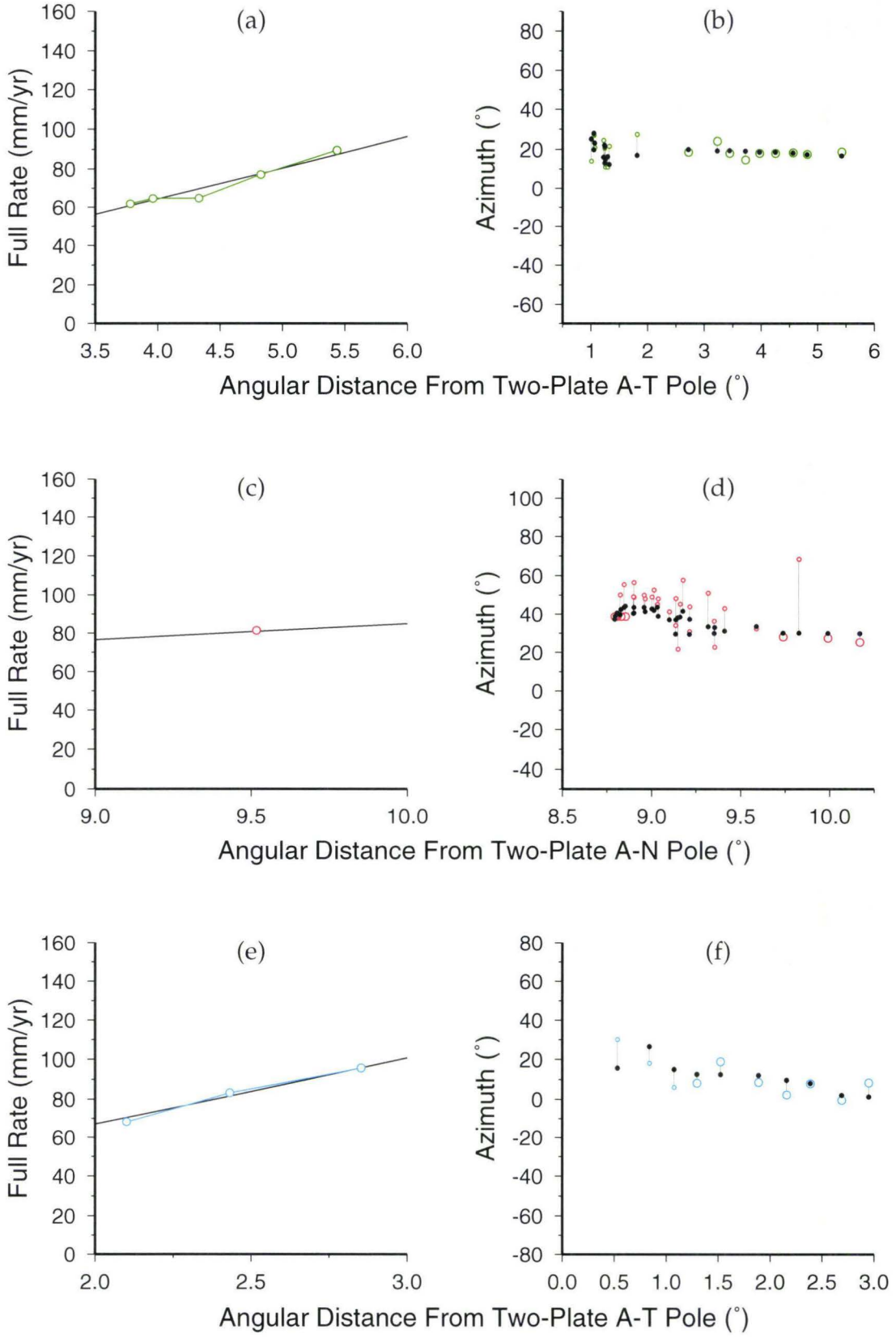
(a)
(b)
(c)
(d)
(e)
(f)
Full Rate (mm/yr)
Azimuth (°)
Angular Distance From Two-Plate A-T Pole (°)
Angular Distance From Two-Plate A-N Pole (°)
Angular Distance From Two-Plate A-T Pole (°)

Fig. 4.5. Compatibility plots of spreading rate and azimuth data for the three-plate solutions of the first run. Predicted values are calculated from the three-plate pole solutions from the first run and are colored according to their respective pole as follows: A-T pole=green; A-N pole=red; N-T pole=blue. Weighted observed values=large open circles; underweighted observed values=small open circles; predicted values=solid black line or closed black circles. (a) Fit of spreading rate to the three-plate A-T pole. (b) Fit of azimuthal model constraints to the three-plate A-T pole. (c) Fit of spreading rate to the three-plate A-N pole. (d) Fit of azimuthal model constraints to the three-plate A-N pole. (e) Fit of spreading rate to the three-plate N-T pole. (f) Fit of azimuthal model constraints to the three-plate N-T pole. The three-plate solutions show a slight compromise in compatibility (compare to Fig. 4.4) due to the additional constraint of three-plate closure criteria.

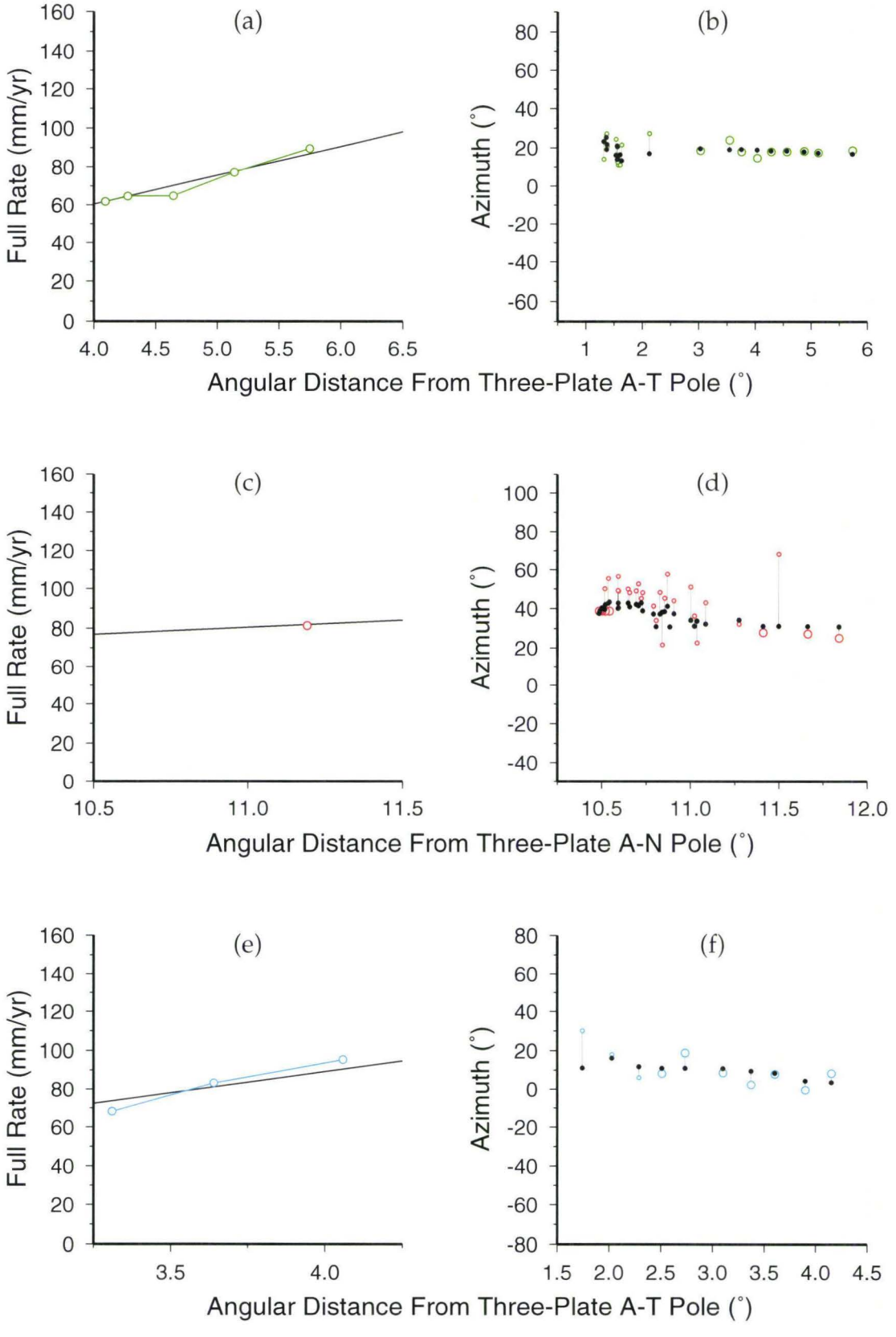
(a)
(b)
(c)
(d)
(e)
(f)
Full Rate (mm/yr)
Azimuth (°)
Angular Distance From Three-Plate A-T Pole (°)
Angular Distance From Three-Plate A-N Pole (°)
Angular Distance From Three-Plate A-T Pole (°)

compromise of the two-plate poles is required to close the plate circuit.

Comparisons between Fig. 4.4 and Fig. 4.5 do reveal slight differences in the matches to the calculated values, however, the compromise undertaken to meet closure criteria is not drastic. The A-T and A-N poles generally match velocity values to within 2 mm/yr (Fig. 4.5 (a) and Fig. 4.5 (c) respectively). The N-T pole, however, shows deviations as large as 6 mm/yr (Fig. 4.5 (e)). Azimuthal data for all three poles, like the two-plate scenario, show the same deviations on average of less than 5° for the weighted values and less than 10° for the underweighted values. Overall, the compromise undertaken to complete the plate circuit generates acceptable variations about the modeled values, as is expected given that the three-plate solutions lie within the 95% confidence contours plotted in Fig. 4.2 and Fig. 4.3.

4.2.4 Is the Geodetic Data Compatible With a Three-Plate Model?

In order to test the compatibility of the marine and geodetic data, the three-plate solution for the A-T pole was used to calculate expected velocities at the GPS locations. Results are plotted in Fig. 4.6. Modeled plate velocities match observed plate velocities with a discrepancy of less than 10% (Fig. 4.6 (a)). Observed and modeled azimuths generally match to within 5° (Fig. 4.6 (b)). Thus, the revised geodetic relative plate velocity values of Bevis (1997) are still greater than those determined by marine magnetic data, but the discrepancy is much less than that reported by Taylor et al., (1996) and illustrated in Fig. 1.10. Fig. 4.6 shows that the Lau Basin marine magnetic data and geodetic data are indeed compatible enough to be included in the same data set.

Fig. 4.6. Using the three-plate A-T pole solution from the first run, observed geodetic velocities (open circles) are independently tested against calculated predicted values (solid black line or closed black circles). (a) Predicted velocity values come to within 90% of the geodetically observed relative plate velocities, and (b) predicted azimuths all match generally to within 5°. The geodetic vectors are considered compatible with the other A-T model constraints.

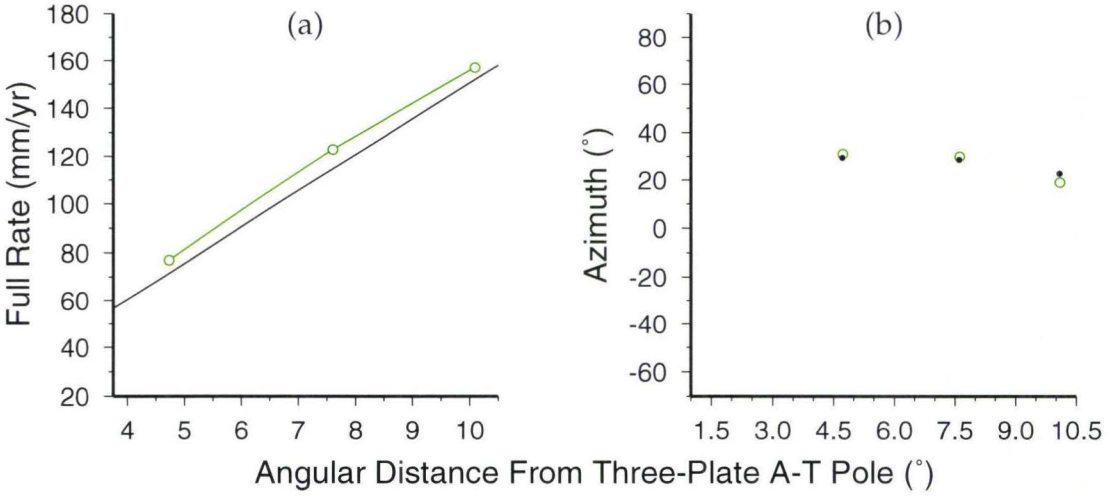
(a)
(b)
Full Rate (mm/yr)
Azimuth (°)
180
160
140
120
100
80
60
40
20
80
60
40
20
0
-20
-40
-60
4 5 6 7 8 9 10
1.5 3.0 4.5 6.0 7.5 9.0 10.5
Angular Distance From Three-Plate A-T Pole (°)

4.3 Second Run: Incorporation of Geodetic Data

The geodetic data are shown to be consistent with the marine magnetic data in the three-plate model for the first run, it was reasonable to then combine the geodetic data with other A-T model constraints. Additionally, because the GPS stations lie at an increased range of angular distances and azimuths away from the (first run) A-T pole, the revised input set of data is more robust.

4.3.1 Revised Two- and Three-Plate Pole Solutions and Their 95% Confidence Regions

Results of the revised two-plate and three-plate solutions are reported in Table 4.3 and Table 4.4 respectively, and plotted in Fig. 4.7 - 4.8. The revised results are very similar to the first run.

Pole	Boundary	Long (°W)	Lat (°S)	ω (°/Ma)
A-T	ELSC	177.7	25.0	8.4
A-N	CLSC,PR	171.2	10.0	4.4
N-T	FRSC	174.9	18.7	17.3

Table 4.3 Best fit two-plate poles of opening for combined marine, seismic and geodetic data.

The most striking difference between the first run and the second run is that the A-T 95% confidence region shrinks dramatically. This is due, in part, to the strict match to the geodetic plate vectors required for each trial pole, i.e., they are unaffected by the spatial location of the poles being tested statistically. Because no geodetic data are available for the A-N and N-T poles,

Fig. 4.7. Euler poles and the two-plate 95% confidence regions (longitude-latitude space) for the second run. Solid stars show the locations of the two-plate pole solutions; open stars show the locations of the three-plate pole solutions. The A-T boundary is plotted in green; A-N boundary is plotted in red; N-T boundary is plotted in blue. The A-T pole is now very tightly constrained due to the addition of the geodetic relative plate velocity vectors. The confidence regions for the N-T and A-N poles remains unchanged from the first run (compare Fig. 4.2) because no geodetic data is available to constrain them.

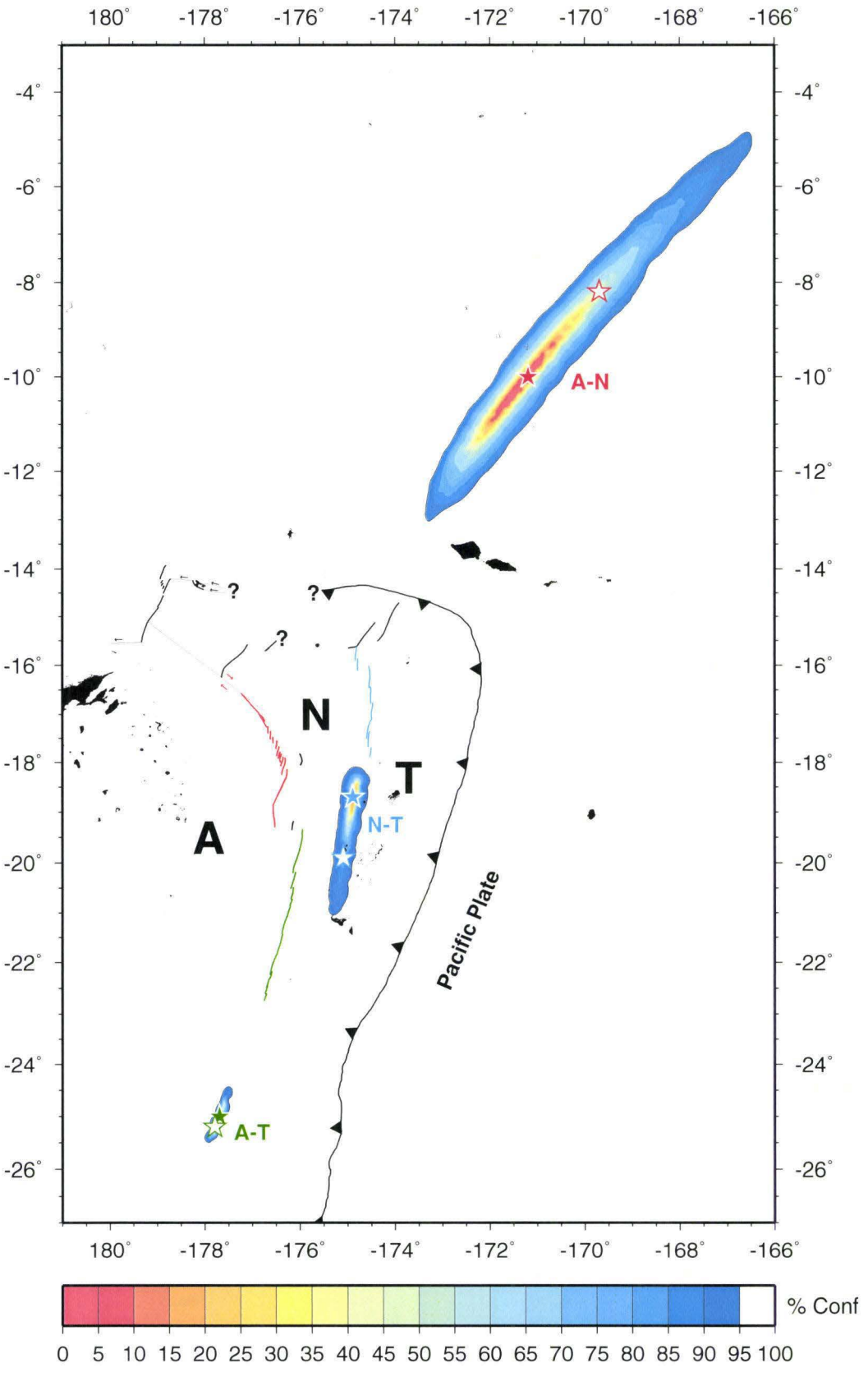
180°
-178°
-176°
-174°
-172°
-170°
-168°
-166°
-4°
-6°
-8°
-10°
-12°
-14°
-16°
-18°
-20°
-22°
-24°
-26°
A-N
N
T
A
N-T
A-T
Pacific Plate
?
% Conf
0 5 10 15 20 25 30 35 40 45 50 55 60 65 70 75 80 85 90 95 100

Fig. 4.8. Euler poles and the two-plate 95% confidence regions (ω-latitude space) for the second run. Solid stars show the locations of the two-plate pole solutions; open stars show the locations of the three-plate pole solutions. The A-T pole is very tightly constrained in ω. The confidence regions for the N-T and A-N poles remains unchanged from the first run (compare Fig. 4.3) because no geodetic data is available to constrain them.

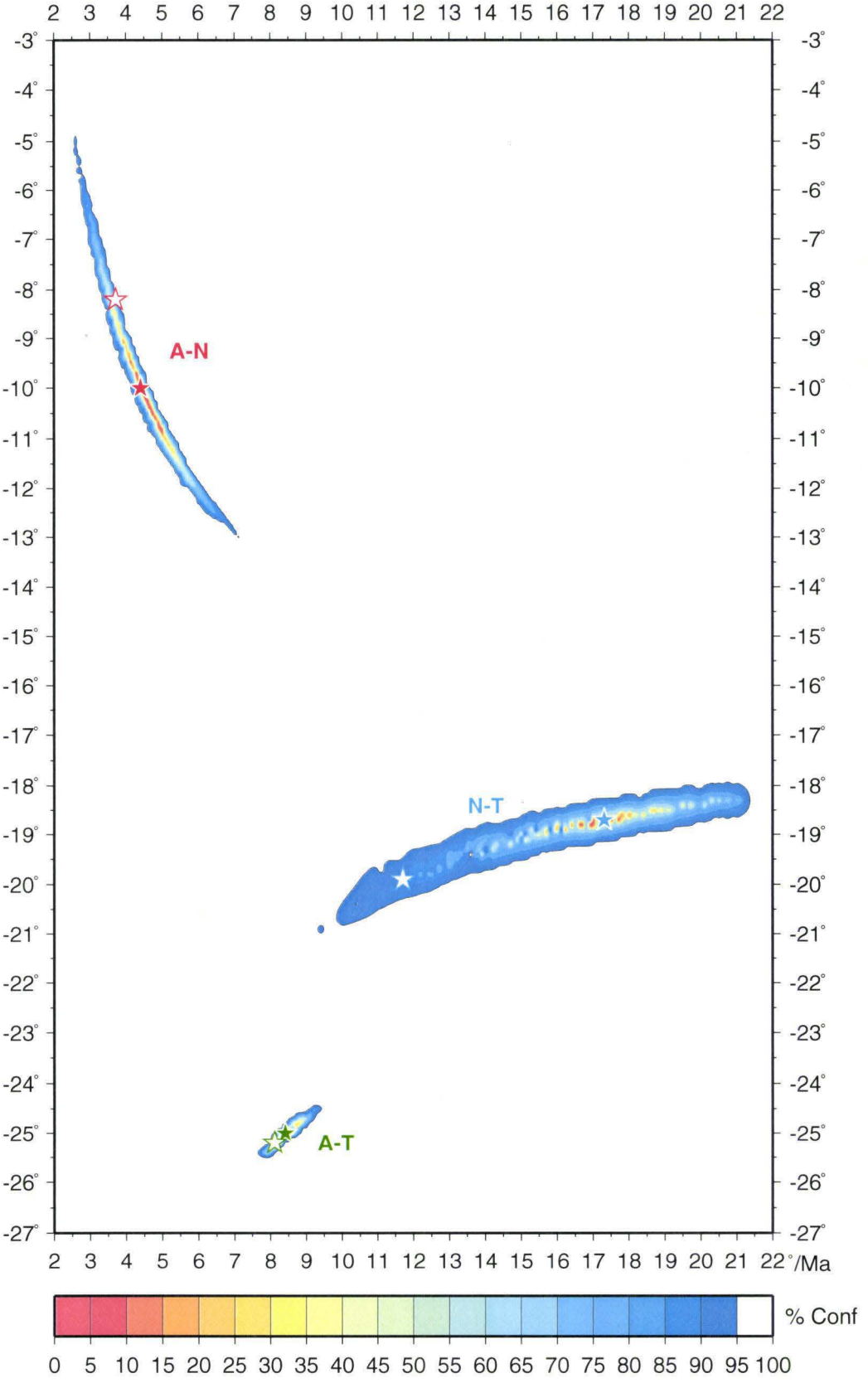
2 3 4 5 6 7 8 9 10 11 12 13 14 15 16 17 18 19 20 21 22
-3° -4° -5° -6° -7° -8° -9° -10° -11° -12° -13° -14° -15° -16° -17° -18° -19° -20° -21° -22° -23° -24° -25° -26° -27°
A-N
N-T
A-T
°/Ma
% Conf
0 5 10 15 20 25 30 35 40 45 50 55 60 65 70 75 80 85 90 95 100

their 95% confidence contours remain the same as were plotted for the first run.

Pole	Boundary	Long (°W)	Lat (°S)	ω (°/Ma)
A-T	ELSC	177.8	25.2	8.1
A-N	CLSC,PR	169.7	8.2	3.7
N-T	FRSC	175.1	19.9	11.7

Table 4.4 Best fit three-plate pole solution for combined marine, seismic and geodetic data.

4.3.2 Fit to Revised Two- and Three-Plate Pole Solutions

Fig. 4.9 (a - f) shows the two-plate compatibility for the second run. The new two-plate A-T pole shows that there is indeed a pole that is highly compatible with the magnetic and the geodetic data (Fig. 4.9 (a, b)). On average, modeled plate velocity values deviate by less than 3 mm/yr from those of the two-plate poles (Fig. 4.9 (a, c, e)). Azimuthal trends again show generally less than 5° deviations for the weighted data and the approximately less than 10° deviations for the underweighted data (Fig. 4.9 (b, d, f)).

Finally, Fig. 4.10 (a - f) shows the three-plate solution for the whole data set. Again, because the three-plate solution lies within the 95% confidence contours displayed in Fig. 4.7 and Fig. 4.8, the overall compromise to meet the three-plate circuit criteria is acceptable. All spreading rate/plate velocity data match on average to within 4 mm/yr (Fig. 4.10 (a, c, e)), and azimuthal deviations (Fig. 4.10 (b, d, f)) show very similar trends as in the two-plate comparison of Fig. 4.9.

Fig. 4.9. Compatibility plots of spreading rate and azimuth data for the two-plate solutions of the second run. Predicted values are calculated from the two-plate pole solutions from the first run and are colored according to their respective pole as follows: A-T pole=green; A-N pole=red; N-T pole=blue. Weighted observed values=large open circles; underweighted observed values=small open circles; predicted values=solid black line or closed black circles. (a) Fit of spreading rate and geodetic velocities to the two-plate A-T pole. (b) Fit of azimuthal model constraints to the two-plate A-T pole. (c) Fit of spreading rate and geodetic velocities to the two-plate A-N pole. (d) Fit of azimuthal model constraints to the two-plate A-N pole. (e) Fit of spreading rate and geodetic velocities to the two-plate N-T pole. (f) Fit of azimuthal model constraints to the two-plate N-T pole. The two-plate solutions are expected to give the best statistical fit possible to their respective model constraints because no compromise has been made to meet three-plate closure criteria at this step in the modeling procedure. Here, the addition of the geodetic vectors (A-T pole only) gives a greater range of angular distances and azimuths from the pole, and in turn helps to constrain velocity measurements to a greater extent than in the first run.

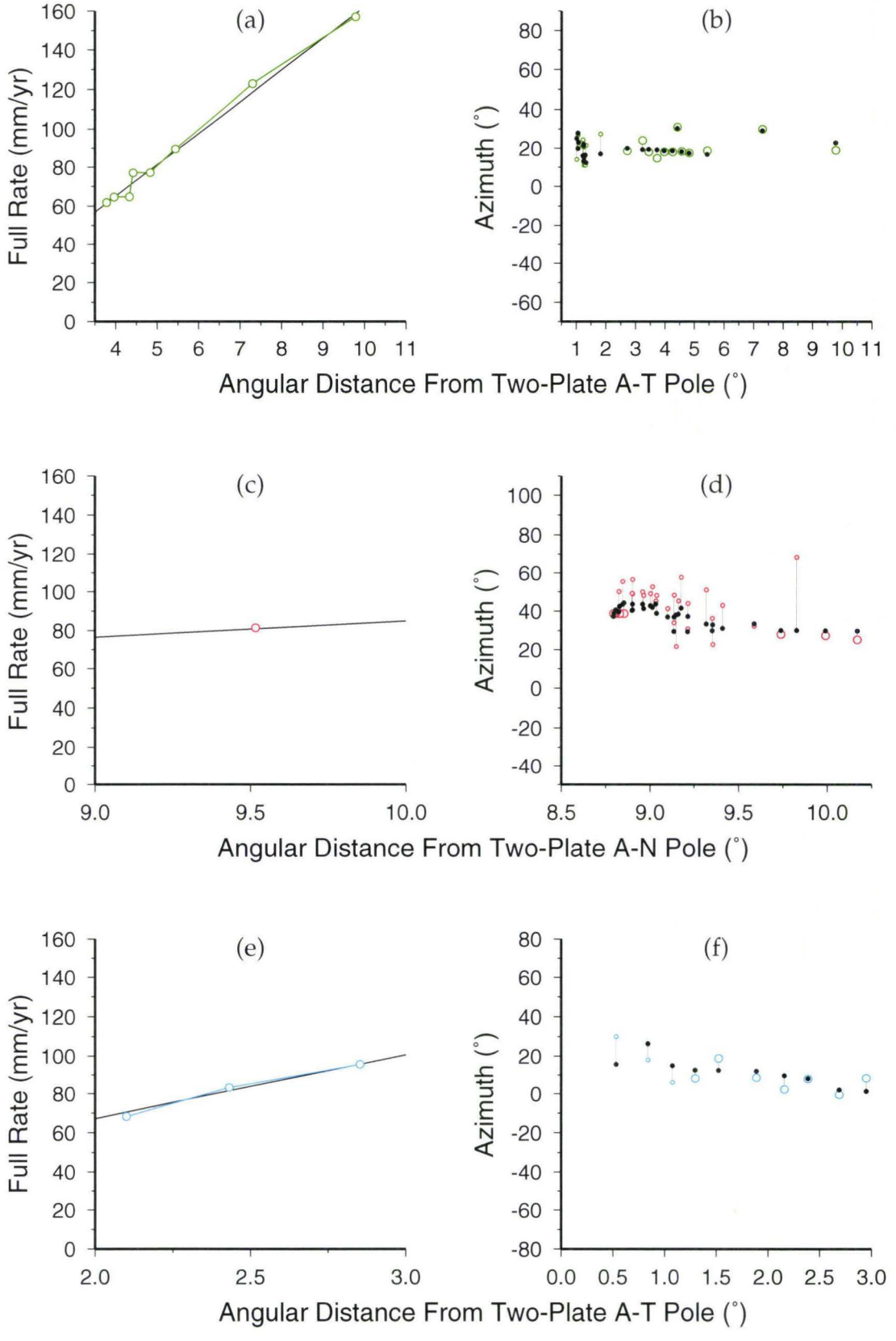
(a)
(b)
(c)
(d)
(e)
(f)
Full Rate (mm/yr)
Azimuth (°)
Angular Distance From Two-Plate A-T Pole (°)
Angular Distance From Two-Plate A-N Pole (°)
Angular Distance From Two-Plate A-T Pole (°)

Fig. 4.10. Compatibility plots of spreading rate and azimuth data for the three-plate solutions of the second run. Predicted values are calculated from the three-plate pole solutions from the first run and are colored according to their respective pole as follows: A-T pole=green; A-N pole=red; N-T pole=blue. Weighted observed values=large open circles; underweighted observed values=small open circles; predicted values=solid black line or closed black circles. (a) Fit of spreading rate and geodetic velocities to the three-plate A-T pole. (b) Fit of azimuthal model constraints to the three-plate A-T pole. (c) Fit of spreading rate and geodetic velocities to the three-plate A-N pole. (d) Fit of azimuthal model constraints to the three-plate A-N pole. (e) Fit of spreading rate and geodetic velocities to the three-plate N-T pole. (f) Fit of azimuthal model constraints to the three-plate N-T pole. The three-plate solutions show a slight compromise in compatibility (compare to Fig. 4.9) due to the additional constraint of three-plate closure criteria.

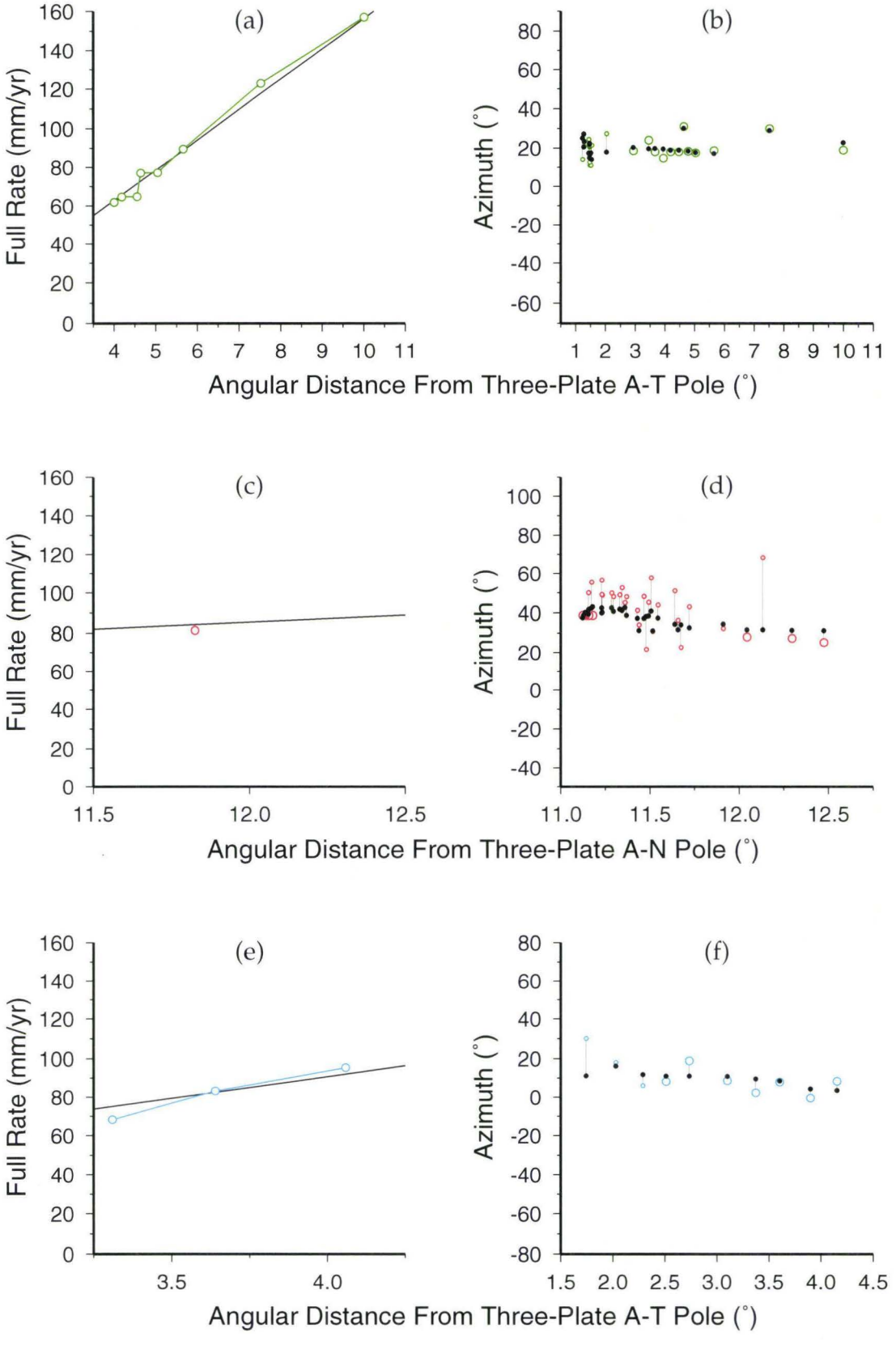
(a)
(b)
(c)
(d)
(e)
(f)
Full Rate (mm/yr)
Azimuth (°)
Angular Distance From Three-Plate A-T Pole (°)
Angular Distance From Three-Plate A-N Pole (°)
Angular Distance From Three-Plate A-T Pole (°)

4.4 Summary of Results

Using the three-plate pole results from the second run, results for the main boundaries in the A-N-T plate system are plotted in Figs. 4.11-4.13. Graphical comparisons between the observed the modeled azimuthal values are plotted. (In the cases where the observed and modeled azimuths are perfectly matched, only the predicted values can be seen on the plot. The greater the azimuthal mismatch shown in Fig. 4.10, the more obvious the error shown in Figs. 4.11-4.13.)

Because "observed" values of spreading rates (in mm/yr) are a function of the pole and the pairs of Brunhes/Matuyama end points, they are also included in Figs. 4.11-4.13 and correspond to the values plotted in Fig. 4.10. The resultant small circles subtended between the chosen Brunhes/Matuyama boundaries and their respective three-plate pole solution are additionally plotted. The closer the pole is to the boundary, the greater the curvature in the subtended small circle.

4.4.1 Australia-Tonga (A-T) Pole

Fig. 4.11 graphically displays the "tightness" of the 95% confidence region of A-T pole, as little difference between the weighted ELSC ridge azimuths and the modeled values is observed. In addition, small circles subtended about this pole match picked Brunhes/Matuyama boundaries well, as was expected given the close match of expected and observed velocity values shown in the three-plate comparisons of Fig. 4.10. In the case of the A-T pole, the curvature of the subtended small circles is very slight due to the relatively great distance away from the pole of opening.

Fig. 4.11. Graphical comparison between observed model constraints (green Brunhes/Matuyama boundary markers and green ridge azimuth observations; refer also to Fig. 3.2) and the predicted values (same symbols are overlaid in black) for the revised three-plate A-T pole. T-Axes south of the ELSC (shown in Fig. 3.2) are not included in this plot. Observed spreading rates (green) and predicted spreading rates (black) are labeled in mm/yr (within boxes). Gray areas are regions of positively magnetized crust. All available seismic data is plotted (refer to Fig. 1.11 for seismic symbol definitions). Both the velocity and azimuthal model constraints match very well, which is additionally reflected in Fig. 4.7, Fig. 4.8, and Fig. 4.10.

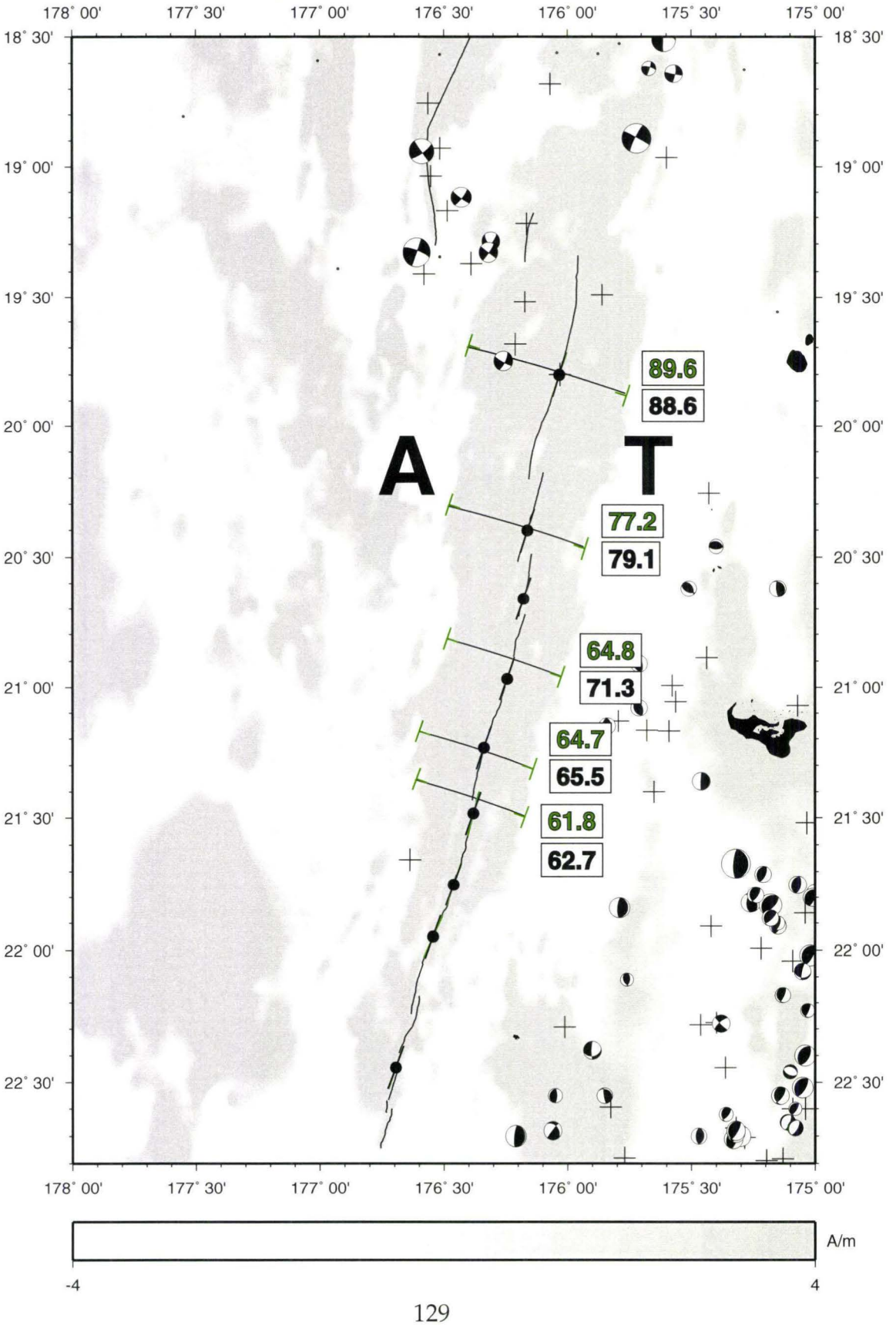
178° 00'
177° 30'
177° 00'
176° 30'
176° 00'
175° 30'
175° 00'
18° 30'
19° 00'
19° 30'
20° 00'
20° 30'
21° 00'
21° 30'
22° 00'
22° 30'
A T
89.6
88.6
77.2
79.1
64.8
71.3
64.7
65.5
61.8
62.7
A/m
-4
4

Fig. 4.12. Graphical comparison between observed model constraints (red Brunhes/Matuyama boundary markers and red ridge azimuth observations; refer also to Fig. 3.2) and the predicted values (same symbols are overlaid in black) for the revised three-plate A-N pole. Observed spreading rates (red) and predicted spreading rates (black) are labeled in mm/yr (within boxes). Gray areas are regions of positively magnetized crust. All available seismic data is plotted (refer to Fig. 1.11 for seismic symbol definitions). The ~10° mismatch in the underweighted seismic slip vectors (refer also to Fig. 4.10 (d)) is due to the introduced bias of forcing the pole to match weighted model constraints along the PR and CLSC.

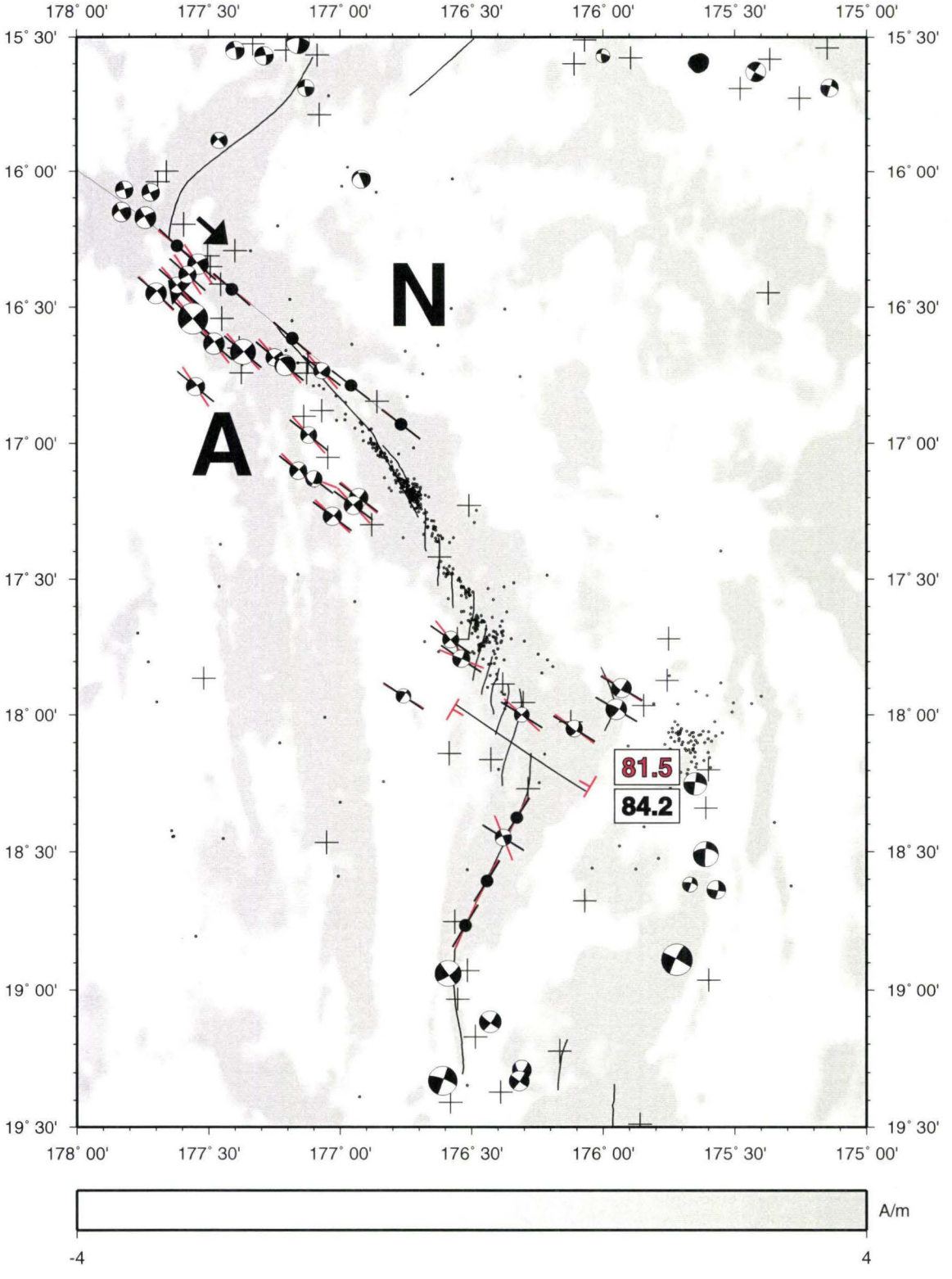
178° 00'
177° 30'
177° 00'
176° 30'
176° 00'
175° 30'
175° 00'
15° 30'
16° 00'
16° 30'
17° 00'
17° 30'
18° 00'
18° 30'
19° 00'
19° 30'
N
A
81.5
84.2
A/m
-4
4

Fig. 4.13. Graphical comparison between observed model constraints (blue Brunhes/Matuyama boundary markers and blue ridge azimuth observations; refer also to Fig. 3.2) and the predicted values (same symbols are overlaid in black) for the revised three-plate N-T pole. Observed spreading rates (blue) and predicted spreading rates (black) are labeled in mm/yr (within boxes). Gray areas are regions of positively magnetized crust. All available seismic data is plotted (refer to Fig. 1.11 for seismic symbol definitions). Weighted ridge azimuths match on average to <5° (refer also to Fig. 4.10 (f)). Small circles subtended about the N-T pole show high curvature due to their close proximity to the pole (refer to Fig. 4.7).

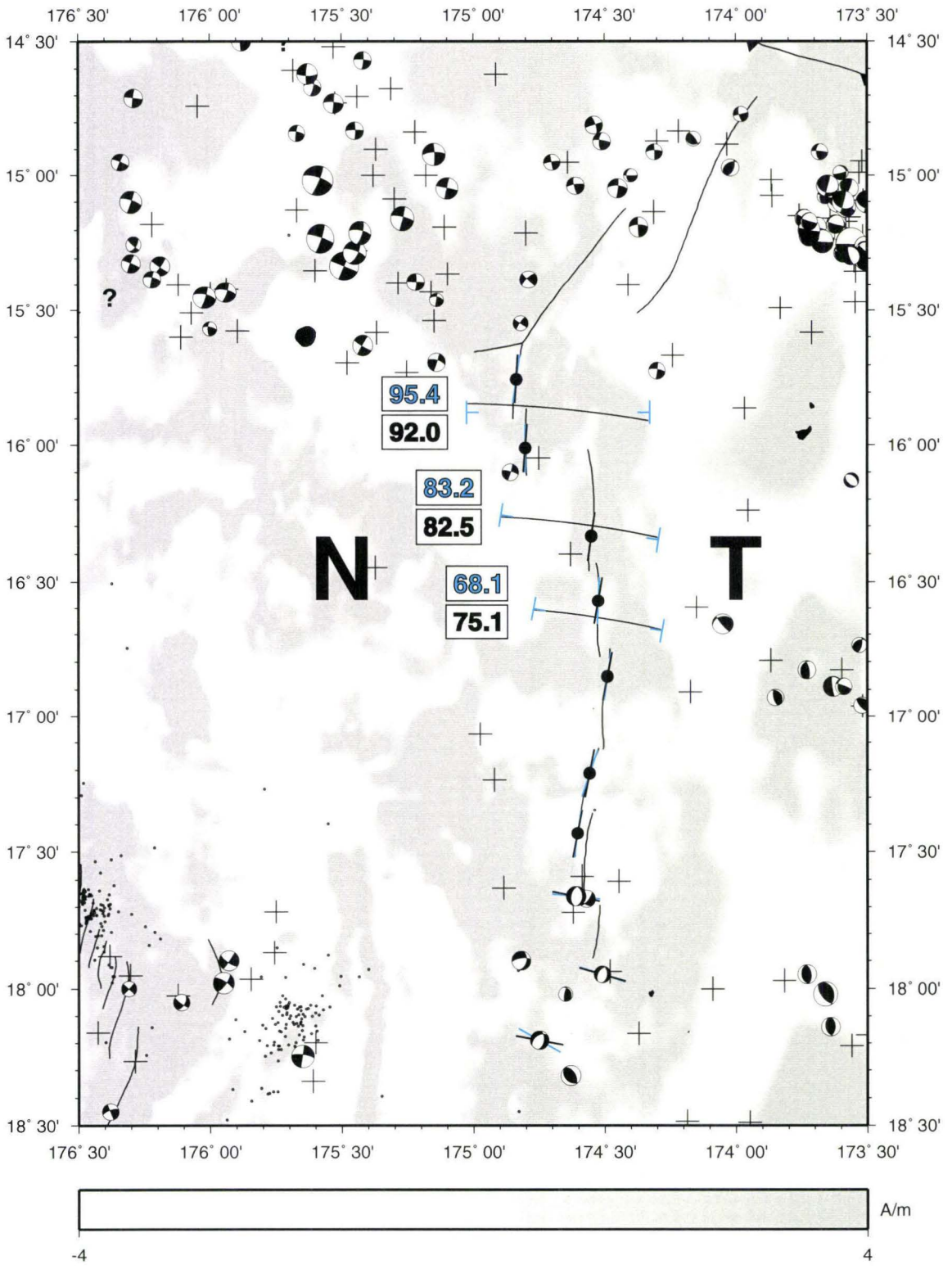
176° 30'
176° 00'
175° 30'
175° 00'
174° 30'
174° 00'
173° 30'
14° 30'
15° 00'
15° 30'
16° 00'
16° 30'
17° 00'
17° 30'
18° 00'
18° 30'
?
95.4
92.0
83.2
82.5
68.1
75.1
N
T
A/m
-4
4

4.4.2 Australia-Niuafo'ou (A-N) Pole

Fig. 4.12, on the other hand, again reflects the greater uncertainty of the A-N pole: the previously discussed ~10° mismatch of the underweighted slip vectors near the transform, the reasonable fit to the single pair of Brunhes/Matuyama boundaries, and the close fit to the weighted azimuths along PR and the CLSC. Modeled weighted azimuths along the PR and CLSC match very well. Any mismatch in these azimuths may be due, in part, to the systematic anticlockwise rotation of the seismic slip azimuths. Slip vectors cannot reflect any component of extension that may be occurring near the PR and the LETZ, which may explain why they do not match the trace of the transform fault.

4.4.3 Niuafo'ou-Tonga (N-T) Pole

Fig. 4.13 displays the reasonable fit of the modeled parameters predicted by the three-plate N-T pole to the model constraints along the FRSC. The great range of possible angular rates for the N-T pole and the close proximity of the N-T pole (Fig. 4.8) to the FRSC are the main causes of misfit to the spreading rate inputs. Weighted ridge azimuthal observations match predictions to within 5° (refer also to Fig. 4.10), with the exception of one underweighted focal mechanism very close to the N-T pole.

4.5 Discussion of Results and Their Implications

Final results of the Lau Basin tectonics according to the revised three-plate model are summarized in Fig. 4.14. In this section the main tectonic implications of the three-plate kinematic model are summarized.

Fig. 4.14. Summary of tectonic results for the revised three-plate pole solution set. Observed spreading rates and GPS relative plate velocities are labeled in mm/yr (within boxes). Gray areas are regions of positively magnetized crust. All available seismic data is plotted (refer to Fig. 1.11 for seismic symbol definitions). Refer also to Fig. 1.2 for a list of plate boundary names. Results of the kinematic model are colored according to their respective pole: A-T pole=green; A-N pole=red; N-T pole=blue.

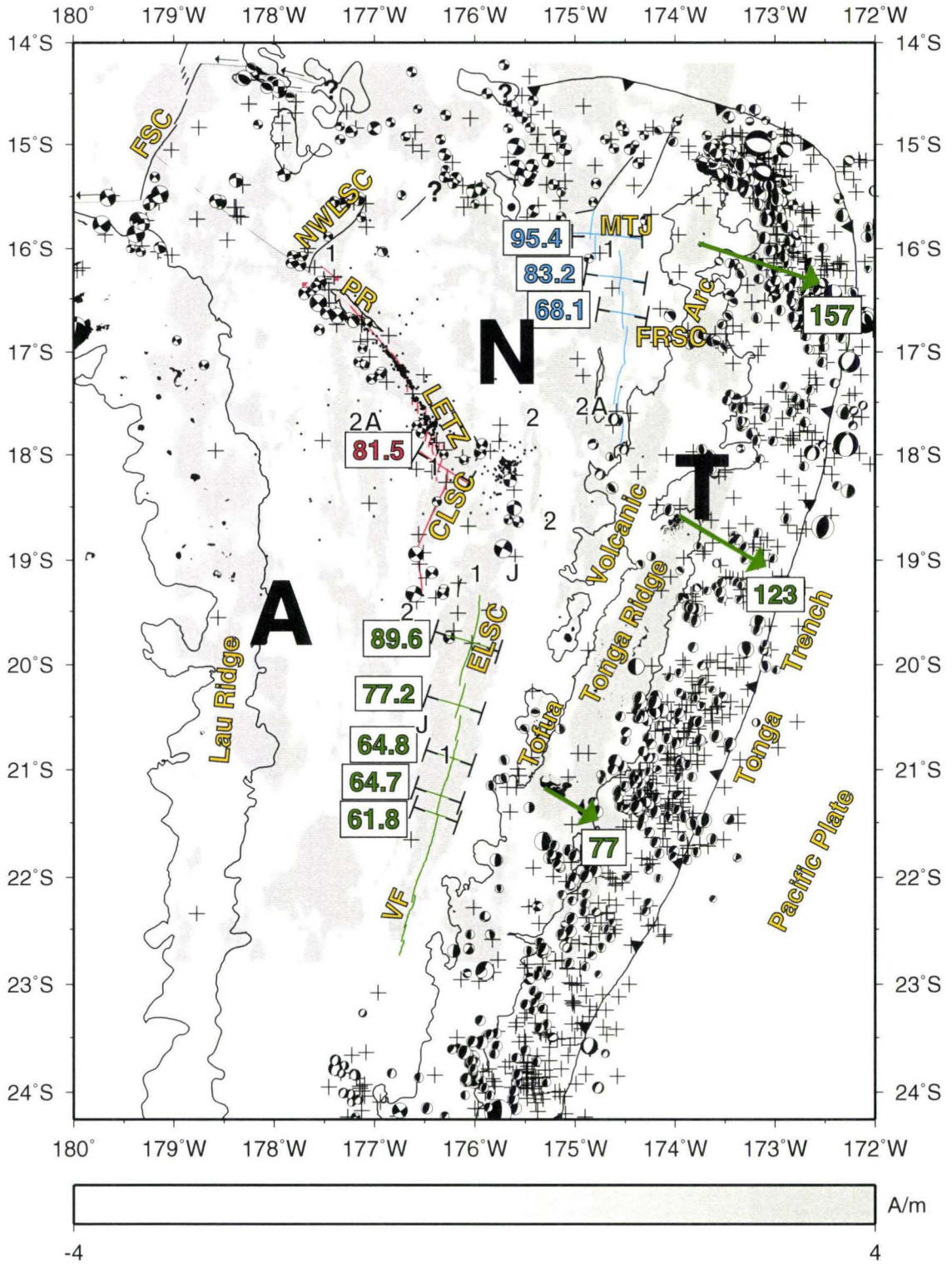
180°
179°W
178°W
177°W
176°W
175°W
174°W
173°W
172°W
14°S
15°S
16°S
17°S
18°S
19°S
20°S
21°S
22°S
23°S
24°S
FSC
NWLSC
PR
LETZ
CLSC
ELSC
VF
Lau Ridge
Volcanic
Tonga Ridge
Trench
Tofua
Tonga
Pacific Plate
MTJ
FRSC Arc
N
A
T
95.4
83.2
68.1
81.5
89.6
77.2
64.8
64.7
61.8
157
123
77
2A
1
2
J
A/m
-4
4

4.5.1 A Multiple Plate System for the Lau Basin

One of the main results of our analysis is that the kinematics of three plate-like regions in the Lau Basin can be described, even given the ambiguity of the southern boundary of the Niuafo'ou microplate. A majority of the model constraints used as inputs are well matched by the three-plate kinematic model. The initial recognition that the motions on the ELSC and the CLSC are not co-polar allowed for the motion of the intervening microplate to be accounted for within the model. The three-plate solutions allow for the additional motion at the boundaries of the microplate, and moreover, are compatible with the observed A-T geodetic velocities.

The reasonable fit of the three-plate model to the data also implies that pole positions over the past 0.78 Ma have been stable (within their respective 95% confidence ellipsoids). That the geodetic vectors are compatible with the marine-magnetic determined spreading rates implies that the plate motion vectors determined geodetically are applicable for at least 0.78 Ma.

4.5.2 Nature of Plate Boundaries

Although the three-plate model accounts for a majority of the tectonic features throughout the Lau Basin, some of the boundaries in the A-N-T system cannot be fully understood within the scope of this kinematic model.

The LETZ, for example, is a complex set of overlapping ridges that accommodate both extensional and strike-slip motion. It is difficult to locate unaltered (non-overprinted) Brunhes/Matuyama boundaries in this area, probably because of its complex history over the past ~2 Ma.

Most notably, the southern boundary of the Niuafo'ou microplate is also most certainly not a rigid plate boundary. The area is well mapped, and the only indication of a boundary is the small set of seismicity along its southern border. Therefore, although the kinematics for this aseismic region can be defined, there may be migrating and/or diffuse plate boundaries that are not accounted for in this model. Using the three-plate solution of the N-T pole, we can estimate the relative motions between the microplate and the Tongan plate. Fig. 4.15 shows predicted N-T relative plate velocities along possible locations of the indistinct southern N-T boundary. Near the southern tip of the FRSC, N-T rates of relative motion are predicted to be ~45 mm/yr (± 5 mm/yr) decreasing to ~35 mm/yr (± 5 mm/yr) near the CLSC/ELSC overlap. The boundary in this region may be rapidly migrating to accommodate these rates, in which case a narrow plate boundary would not necessarily be evident. According to the vector field predicted by the three-plate N-T pole (Fig. 4.15), a theoretical boundary (striking approximately NE between the southern tips of the CLSC and the FRSC) would be in a shear zone near the CLSC and would be under extension close to the FRSC.

4.5.3 Propagation Rates at the CLSC

The CLSC has been mapped and its morphology studied in detail (Weidicke and Habler, 1993). Weidicke and Habler note a distinct bend in the ridge axis at 18° 57' S (refer to Fig. 3.6 - 3.8 for details of the CLSC). North of 18° 57', propagation has generated seafloor fabric trending NNE. South of 18° 57', they report N-S trending fabric. The recent volcanism and very low sediment cover in this region implies that this region has undergone very rapid extension.

Fig. 4.15. Predicted N-T relative plate velocities along possible locations of the indistinct southern boundary. Predicted rates are plotted in mm/yr. Gray areas are regions of positively magnetized crust. Refer also to Fig. 1.2 for a list of plate boundary names. A theoretical boundary trending NE between the southern tips of the CLSC and the FRSC would be in a shear zone near the CLSC because predicted plate motion in this region is NE/SW. This same boundary would be under extension close to the FRSC because in this region predicted plate motion is approximately E/W.

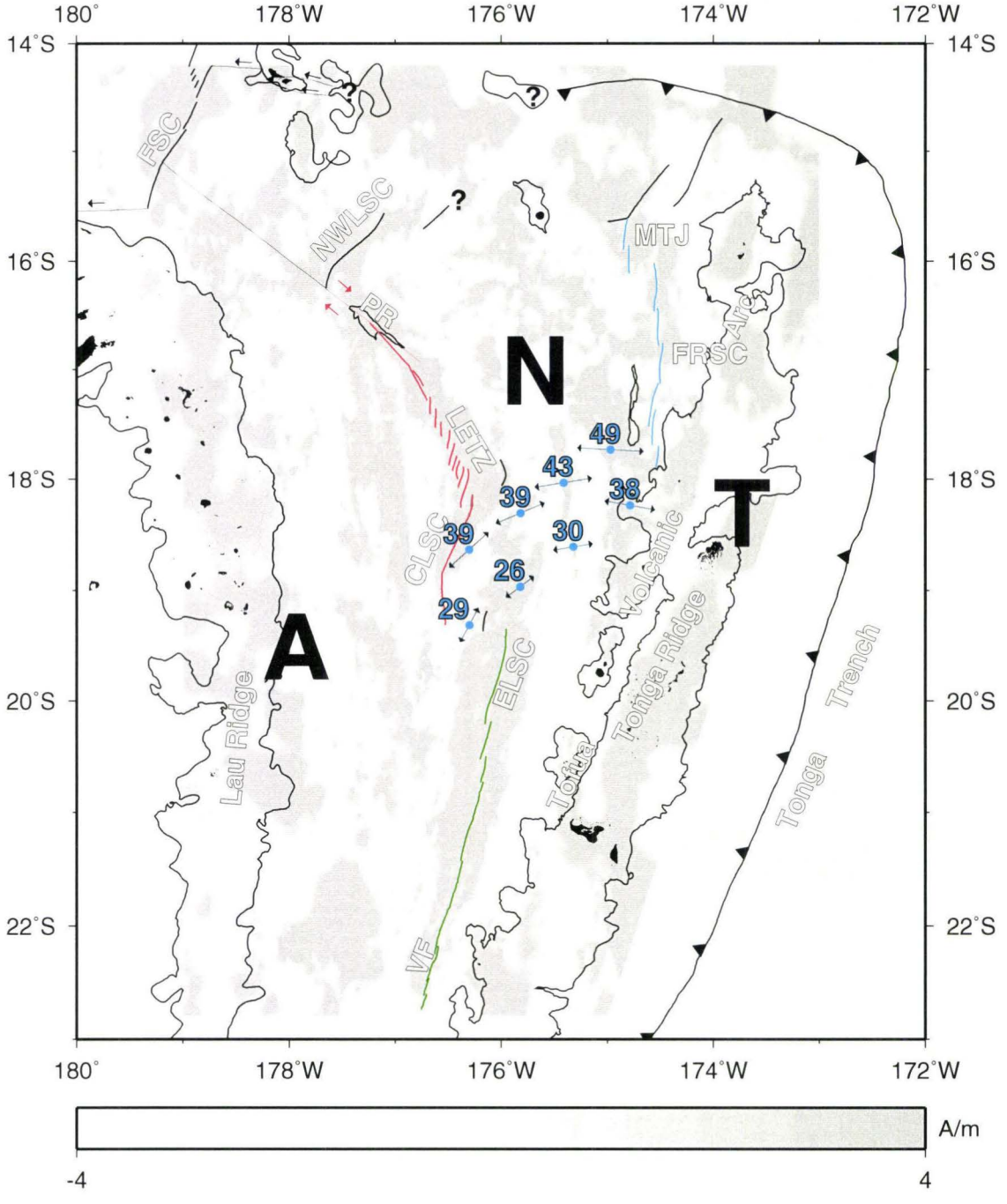
180°
178°W
176°W
174°W
172°W
14°S
16°S
18°S
20°S
22°S
FSC
NWLSC
PR
LETZ
CLSC
ELSC
VF
MTJ
FRSC
Arc
Volcanic
Tonga Ridge
Tonga Trench
Tonga
Lau Ridge
N
T
A
49
43
38
39
30
39
26
29
A/m
-4
4

Using the A-N pole calculated in our model, we can quantify the rates of both the CLSC propagation and the rates of rapid extension to the tectonic tip. We can calculate a synthetic Brunhes/Matuyama boundary using the three-plate A-N pole. Because the crust accreted within the propagation boundaries initiated at the ridge prior to 0.78 Ma, the proportion of the distance to the propagation boundaries relative to the distance across the synthetic Brunhes/Matuyama boundary directly relates to the age of the propagation boundary. Using the angular rate and position associated with the three-plate A-T pole, we estimate that the age of the propagation boundary at 18° 57' S is ~150,000 yrs, which in turn implies a propagation rate of ~111 mm/yr along the CLSC. The distance from the bend to the tectonic tip (located at the terminus of the CLSC) is ~46 km, which indeed implies a very rapid propagation rate of 313 mm/yr.

4.5.4 Implications for Regional Tectonics

South of the Lau Basin lies the Havre Trough and the Taupo Rift (Fig. 4.16). This region is known to be under active extension (Parson and Wright, 1996). Because the location of the three-plate A-T pole is north of the Havre trough and Taupo Rift, it predicts compression in this region. This observation implies that the extensional motion in the Havre Trough is not co-polar with the opening along the ELSC as described by the A-T pole. In other words, a different pole is required to describe extension in the region south of the Lau Basin.

Additionally, geodetically determined rates of Pacific-Tonga motion range from 150 mm/yr at 21°S and 240 mm/yr at 16°S (Bevis, 1995). The

Fig. 4.16. Location of the Harve Trough and Taupo Rift south of the Lau Basin. Depth scale is in km. Both the Harve Trough and Taupo Rift are known to be undergoing active extension. Geodetically determined Tonga-Pacific relative plate velocities (Bevis et al., 1995) are additionally plotted. Rates are listed in mm/yr. The three-plate kinematic model for Lau Basin opening has been shown to be compatible with geodetically determined plate velocities which implies that these high rates of subduction at the Tonga Trench have been maintained for at least 0.78 Ma.

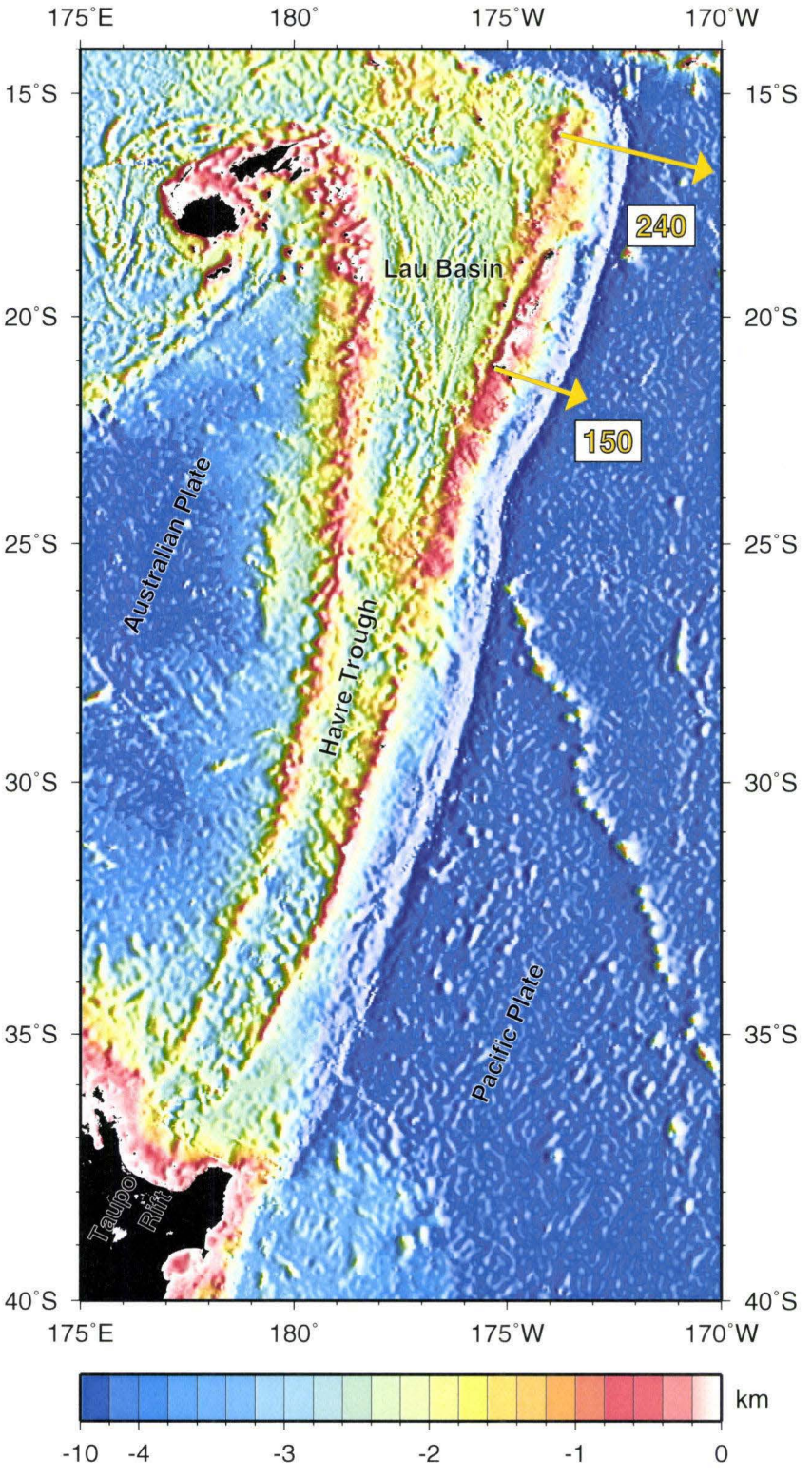
175°E
180°
175°W
170°W
15°S
20°S
25°S
30°S
35°S
40°S
240
150
Lau Basin
Australian Plate
Havre Trough
Pacific Plate
Taupo Rift
km
-10
-4
-3
-2
-1
0

three-plate kinematic model for Lau Basin opening has been shown to be compatible with geodetically determined plate velocities which suggests that subduction of the Pacific Plate at the Tonga Trench has been at these fast rates for at least 0.78 Ma.

4.6 Conclusions

The kinematic model described in this thesis results in the following main conclusions:

(1) Motions across the ELSC and the CLSC/LETZ/PR plate boundaries are not co-polar.

(2) Additional Australian-Tongan (A-T) plate motion in the northern Lau Basin is accommodated by motion at the edges of the intervening Niuafo'ou microplate. Although the southern boundary of the microplate is not well defined, the motion of the interior region microplate is compatible with a three-plate kinematic model in which N-T motion is constrained by geophysical observations near the FRSC.

(3) The kinematics of a three-plate system (A-N-T) have been derived that statistically match (a) Brunhes spreading rates, (b) spreading center and transform fault azimuths, (c) focal mechanism azimuths, and (d) geodetically determined A-T velocities.

APPENDIX

Long 1 (°W)	Lat 1 (°S)	Long 2 (°W)	Lat 2 (°S)	Weight
176.3997	19.6920	175.7630	19.8798	1.0
176.4805	20.3028	175.9311	20.4686	1.0
176.4881	20.8155	176.0271	20.9592	1.0
176.6011	21.1709	176.1398	21.3143	1.0
176.6125	21.3518	176.1739	21.4972	1.0

Table 3.1. A-T: Brunhes/Matuyama Boundary Pairs (0.78 Ma)

Long (°W)	Lat (°S)	Velocity (mm/yr)	Weight
173.7636	15.9467	157	1.0
173.9600	18.5853	123	1.0
175.3089	21.1735	77	1.0

Table 3.2. A-T: GPS Relative Velocities

Long (°W)	Lat (°S)	Azimuth	α(°)	Weight	Source
176.0329	19.8004	18.8	18.8	1.0	Ridge
176.1623	20.4005	17.6	17.6	1.0	Ridge
176.1784	20.6605	18.4	18.4	1.0	Ridge
176.2446	20.9673	18.2	18.2	1.0	Ridge
176.3385	21.2334	18.2	18.2	1.0	Ridge
176.3818	21.4823	14.7	14.7	1.0	Ridge
176.4618	21.7502	18.1	18.1	1.0	Ridge
176.5451	21.9501	24.1	24.1	1.0	Ridge
176.6948	22.4444	18.7	18.7	1.0	Ridge
177.1200	23.2700	117.5	27.5	0.1	T-axis
177.1900	23.8500	110.7	20.7	0.1	T-axis
177.3400	23.7900	101.1	11.1	0.1	T-axis
177.3000	23.7600	101.1	11.1	0.1	T-axis
177.3900	23.7900	111.2	21.2	0.1	T-axis
177.2000	23.8400	102.6	12.6	0.1	T-axis
177.3900	23.7100	111.6	21.6	0.1	T-axis
177.3300	23.8300	114.6	24.6	0.1	T-axis
177.2300	24.0900	104.2	14.2	0.1	T-axis
177.2400	24.0200	111.0	21.0	0.1	T-axis
177.1600	24.0700	117.0	27.0	0.1	T-axis
177.3100	24.0100	117.4	27.4	0.1	T-axis
173.7636	15.9467	109.0	19.0	1.0	GPS

Table 3.3. A-T: Azimuthal Data

173.9600	18.5853	120.0	30.0	1.0	GPS
175.3089	21.1735	121.0	31.0	1.0	GPS

Table 3.3 (Continued). A-T: Azimuthal Data

Long 1 (°W)	**Lat 1 (°S)**	**Long 2 (°W)**	**Lat 2 (°S)**	**Weight**
176.5731	17.9792	176.0514	18.2598	1.0

Table 3.4. A-N: Brunhes/Matuyama Boundary Pairs (0.78 Ma)

Long (°W)	Lat (°S)	Azimuth	α(°)	Weight	Source
177.6200	16.2720	128.7	38.7	1.0	Transform
177.4120	16.4348	128.7	38.7	1.0	Transform
177.1830	16.6111	128.7	38.7	1.0	Transform
176.9590	16.7846	128.7	38.7	1.0	Transform
176.7690	16.9305	128.7	38.7	1.0	Transform
176.3286	18.3759	28.1	28.1	1.0	Ridge
176.4416	18.6072	27.4	27.4	1.0	Ridge
176.5238	18.7694	25.3	25.3	1.0	Ridge
177.1600	17.1000	135.3	45.3	0.1	Slip
176.9300	17.2000	131.3	41.3	0.1	Slip
177.5600	16.5400	139.0	49.0	0.1	Slip
177.0700	16.7300	140.1	50.1	0.1	Slip
177.1200	16.9700	138.1	48.1	0.1	Slip
177.1000	17.1300	111.8	21.8	0.1	Slip
177.5400	16.3400	145.5	55.5	0.1	Slip
177.2500	16.6800	138.9	48.9	0.1	Slip
177.2100	16.7100	139.2	49.2	0.1	Slip
177.4800	16.6300	142.7	52.7	0.1	Slip
177.7000	16.4500	135.2	45.2	0.1	Slip
177.3700	16.6600	138.2	48.2	0.1	Slip
176.9500	17.2300	138.2	48.2	0.1	Slip
177.5500	16.7900	147.7	57.7	0.1	Slip

Table 3.5. A-N: Azimuthal Data

177.6200	16.4200	140.0	50.0	0.1	Slip
177.5800	16.3800	146.6	56.6	0.1	Slip
177.0300	17.2700	134.0	44.0	0.1	Slip
175.9500	17.9800	120.9	30.9	0.1	Slip
175.9300	17.9000	124.2	34.2	0.1	Slip
176.3100	18.0000	133.0	43.0	0.1	Slip
176.5800	17.7200	141.0	51.0	0.1	Slip
176.1100	18.0500	126.4	36.4	0.1	Slip
176.3800	18.4500	158.4	68.4	0.1	Slip
176.5400	17.7900	92.7	2.7	0.1	Slip
176.7600	17.9300	122.4	32.4	0.1	Slip

Table 3.5. (Continued) A-N: Azimuthal Data

Long 1 (°W)	**Lat 1 (°S)**	**Long 2 (°W)**	**Lat 2 (°S)**	**Weight**
175.0257	15.8758	174.3276	15.8758	1.0
174.8958	16.2579	174.2958	16.3496	1.0
174.7722	16.6014	174.2822	16.6869	1.0

Table 3.6. N-T: Brunhes/Matuyama Boundary Pairs (0.78 Ma)

Long (°W)	Lat (°S)	Azimuth	α(°)	Weight	Source
174.8370	15.7514	8.3	8.3	1.0	Ridge
174.8030	16.0108	-0.6	-0.6	1.0	Ridge
174.5510	16.3359	7.9	7.9	1.0	Ridge
174.5250	16.5716	2.3	2.3	1.0	Ridge
174.4900	16.8533	8.5	8.5	1.0	Ridge
174.5580	17.2125	18.8	18.8	1.0	Ridge
174.6040	17.4342	8.1	8.1	1.0	Ridge
174.6100	17.6600	96.0	6.0	0.1	T-axis
174.5100	17.9500	107.9	17.9	0.1	T-axis
174.7500	18.1900	120.0	30.0	0.1	T-axis

Table 3.7. N-T: Azimuthal Data

REFERENCES

Bevis, M., F. W. Taylor, B. E. Schutz, J. Recy, B. L. Isacks, S. Hely, R. Singh, E. Kendrick, J. Stowell, B. Taylor, and S. Calmant, Geodetic observations of very rapid convergence and back-arc extension at the Tonga arc, *Nature*, 374: 249-251, 1995.

Bevis, M., Geodetic Measurements in the Tonga-Lau Arc System (abstract),*EOS, Trans. Am. Geophys. Union*, 78: 697-698, 1997.

Caress, D. W., and D. N. Chayes, New software for processing sidescan data from sidescan-capable multibeam sonars, *Proceedings of the IEEE Oceans 95 Conference*, 997-1000, 1995.

Cox, A., and R. B. Hart, *Plate Tectonics: How it Works*, 392 pp., Blackwell Science, Cambridge, Mass., 1986.

Efron, B., and R. Tibshirani, Bootstrap Methods for Standard Errors, Confidence Intervals, and Other Measures of Statistical Accuracy, *Statistical Science*, 1: 54-77, 1986.

Eguchi, T., Microearthquakes and tectonics in an active back-arc basin: the Lau Basin, *Phys. Earth Plant. Inter.*, 56: 210-229, 1987.

Hamburger M. W., and B. L. Isacks, Diffuse back-arc deformation in the southwestern Pacific, *Nature*, 332: 599-604, 1988.

Hawkins, J. W., and S. Helu, Polymetallic sulphide deposit from "black smoker" chimney: Lau Basin, *EOS*, 67: 378, 1986.

Karig, D., Ridges and Basins of the Tonga-Keradec Island Arc System, J. *Geophys. Res.*, 75: 239-254, 1970.

Lawver, L. A., J. W. Hawkins, and J. G. Sclater, Magnetic Anomalies and Crustal Dilation in the Lau Basin, *Earth Planet Sci Lett.*, 33: 27-35, 1976.

Lawver, L. A., and J. W. Hawkins, Diffuse magnetic anomalies in the marginal basins: Their possible tectonic and petrologic significance, *Tectonophysics*, 45: 323-339, 1978.

Martinez, F., P. Fryer, N. A. Baker and T. Yamazaki, Evolution of backarc rifting: Mariana Trough, 20°-24° N, *J. Geophys. Res.*, 100: 3807-3927, 1995.

Morton, J. L., and N. H. Sleep, Seismic reflections from a Lau Basin magma chamber, in: *Geology and Offshore Resources of Pacific Island Arcs -- Tonga Region*, D. Scholl and T. Vallier, eds., pp. 441-453, Circum-Pacific Council for Energy and Mineral Resources, Houston, TX, 1985.

Parker, R. L. and Huestis, S. P., The inversion of magnetic anomalies in the presence of topography, *J. Geophys. Res.*, 79: 1587-1593, 1974.

Parson, L. M., and J. W. Hawkins, Two-stage ridge propagation and the geological history of the Lau backarc basin, in: *Proc. ODP, Sci. Results*, 135: 819-828, 1994.

Parson, L. M., J. A. Pearce, B. J. Murton, R. A. Hodkinson, and the RRS *Charles Darwin* Scientific Party, Role of ridge jumps and ridge propagation in the tectonic evolution of the Lau back-arc basin, southwest Pacific, *Geology*, 18: 470-473, 1990.

Parson, L. M., and I. C. Wright, The Lau-Havre-Taupo back-arc basin: a southward propagating, multi-stage evolution from rifting to spreading, *Tectonophysics*, 263: 1-22, 1996.

Pelletier, B., S. Calmant and R. Pillet, Current tectonics of the Tonga-New Hebrides region, *Earth Planet Sci Lett.*, 164: 263-276, 1998.

Smith, W. H. F., and D. T. Sandwell, Global sea floor topography from satellite altimetry and ship depth soundings, *Science*, 277: 1956-1962, 1997.

Smith, W.H., and P. Wessel, Gridding with continuous curvature splines in tension, *Geophysics*, 55: 293-305, 1990.

Taylor, B., and G. D. Karner, On the evolution of marginal basins, *Rev. Geophys. Space Phys.*, 21: 1727-1741, 1983.

Taylor, B., K. Crook, and J. Sinton, Extensional transform zones and oblique spreading centers, *J. Geophys. Res.*, 99: 19,707-19,718, 1994.

Taylor, B., K. Zellmer, F. Martinez, and A. Goodliffe, Sea-floor spreading in the Lau back-arc basin, *Earth Planet Sci Lett.*, 144: 35-40, 1996.

Tiffin, D. L., Tectonic and structural features of the Pacific/Indo-Australian plate boundary in the North Fiji-Lau Basin regions, southwest Pacific, *Geo-Mar. Lett.*, 13: 126-131, 1993.

Weissel, J. K., Evolution of the Lau Basin by the growth of small plates, in: *Island Arcs Deep Sea Trenches and Back Arc Basins*, M. Talwani and W. C. Pitman, eds., pp. 429-436, Maurice Ewing Ser. 1, Am. Geophys. Union, Washington, D. C., 1977.

Weissel, J. K., Magnetic lineations in marginal basins of the western Pacific, *Phil. Trans. R. Soc. Lond.*, A300: 223-247, 1981.

Wessel, P. and W. H. F. Smith. Free software helps map and display data. *Eos, Trans. Am. Geophys. Union*, 72 (41): 441-446, 1991.

Wiedicke, M., and J. Collier, Morphology of the Valu Fa Spreading Ridge in the Southern Lau Basin, *J. Geophys. Res.*, 98: 11,769-11,782, 1993.

Wiedicke, M., and W. Habler, Morphotectonic Characteristics of a Propagating Spreading System in the Northern Lau Basin, *J. Geophys. Res.*, 98: 11,783-11,797, 1993.

Wilson, D., Motion and Deformation of Juan de Fuca Plate, *J. Geophys. Res.*, 98: 16,053-16,071, 1993.